THz Sensing Group, Technische Universiteit Delft

Volumetric Method of Moments

Jinglin Geng

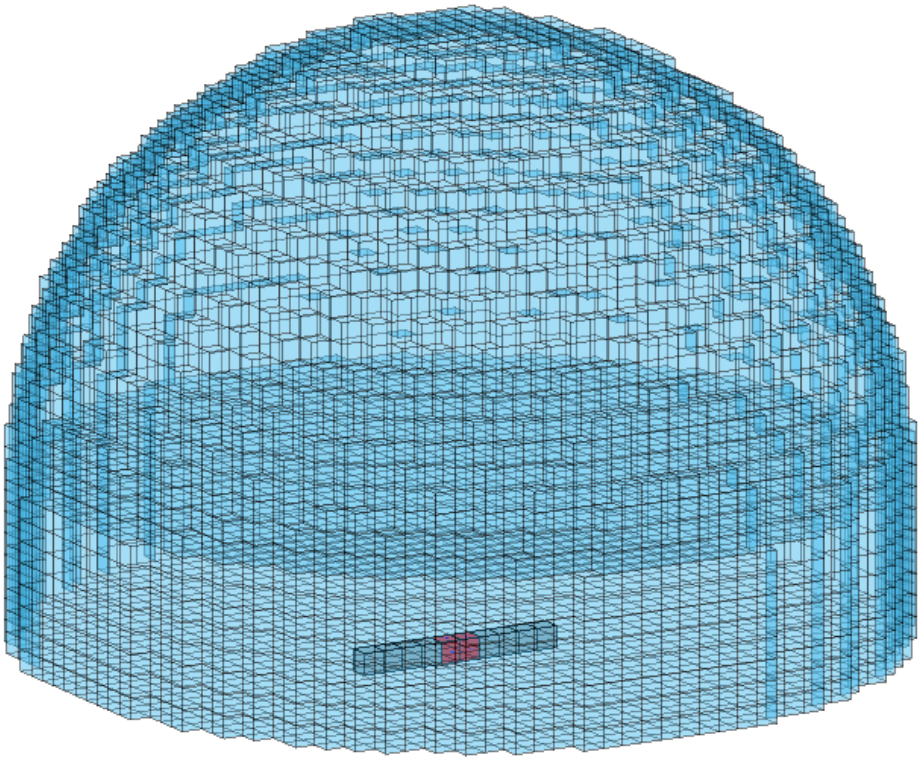

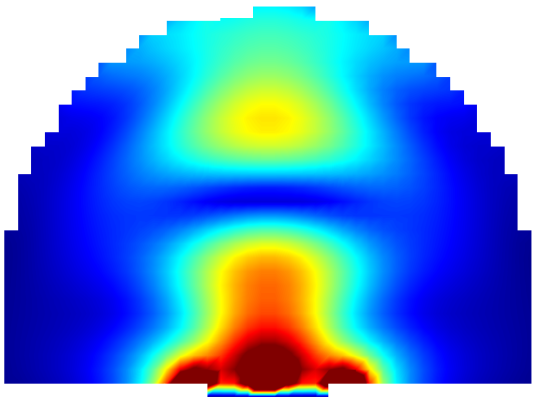

TU Delft Delft University of Technology

TS THz Sensing Group

Volumetric Method of Moments

A Numerical Tool for High Frequency Problems Analysis

by

Jinglin Geng

For the degree of Master of Science in Electrical Engineering, at Delft University of Technology.

To be defended on Friday September 16, 2022 at 1:30 PM.

Committee Member:	Prof. dr. A. Neto,	TU Delft, Supervisor
	Dr. D. Cavallo,	TU Delft
	Dr. ir. R. F. Remis,	TU Delft, External Expert

TU Delft Delft University of Technology

THz Sensing Group

Acknowledgement

I have been very lucky through this journey, as I received so much support from so many people. I would like to acknowledge you all in the thesis.

Firstly, I would like to express my deepest gratitude to my supervisor prof. Andrea Neto for leading me into such an amazing project. I have learned to a great extent from your profound knowledge both professionally and personally. "One day with a wise man benefits me more than ten years of reading", as we say in China, describes perfectly the year I have had. Working with you is an experience that I will appreciate for life.

Then my daily supervisor Riccardo Ozzola. You have been patiently guiding me through the entire year. I appreciate the time you commit to explain me the theory, structure the code, and help me to correct this thesis repeatedly. It is your delicate work and your rigorous attitude that bring this project to what it is now. I am genuinely inspired by your passion for electromagnetic and everything, and I wish you success on the next two years!

I am also grateful for the courses I had last year taught by this group that equips me so much to enter this field. Therefore, I would like to thank Nuria, Daniele, Jochem, Akira for the inspiriting courses and for sharing the knowledge.

Then to my friends in the THz Sensing group: I really enjoy the time we spent together. You are all group of both intelligent and warm-hearted people, and it is my honour to work with you this year. To Roderick Tapia Barroso, it is a pleasure to study and talk to you everyday. Thanks for dropping by constantly and I promise I will pronounce it correctly one day.

I would also like to thank my families who helped me to get through these two years of difficult time. To my parents, thank you for always being there. Even though you are not here in person, I can always rely on you whenever needed. To Renjie, Wenyu, and Yidi, thank you for sheltering me no matter at when, both physically and emotionally.

Thank you all!

耿靖林
Jinglin Geng
15 September, 2022

Abstract

In this thesis a Volumetric Method of Moments (V-MoM) is developed to analyse accurately, and ease the design of small size lens antennas, and to estimate the power emitted by warm bodies constituted by realistic materials, and having arbitrary geometries.

Thanks to the application of the volume equivalence theorem and the use of a structured mesh, this method can be used in a design loop efficiently, since different geometries can be simulated with the same evaluation of the projections, and the specific material arrangements are added at a negligible cost. Therefore, at every design iteration, differently from other integral equation methods, only the linear system has to be solved. Moreover, thanks to the use of a uniform sampling, a convolutional structure is obtained, implying that only a reduced number of projections are sufficient to characterize the entire matrix, reducing significantly the memory requirements, and allowing the solution of large scale systems. The linear system is then solved with an iterative solver, that, thanks to the convolutional properties, can be accelerated by fast matrix-vector products by using Fast Fourier Transform (FFT). The method is validated by studying the field scattered by a homogeneous and multilayer dielectric sphere, proving an accuracy within the discretization tolerance, and the capability of handling inhomogeneous structures.

A Graphical User Interface (GUI) based on the presented method has been developed, with the aim of easing and assisting the user experience on the electromagnetic analysis. The GUI allows to simulate complex geometries combining elementary shapes, characterized by arbitrary materials, and excited by either plane waves or discrete ports. The solution can be post-processed in terms near-fields, far-fields, and network quantities.

A representation in terms of *impressed* currents and *incident* voltage has been formulated to represent the incoherent radiometric sources in the V-MoM, used to analyse the power emitted by lossy semiconductors, characterized by a Drude's dispersion for the conductivity. An experimental setup to verify the numerical and analytical model is then designed.

Contents

1 Introduction

1.1. Motivation

This work deals with the development of a full wave simulation tool that solves high frequency problems regarding to dielectric structures within several wavelengths. The reason for this is that high frequency applications (especially in terahertz band) have drawn more and more attention from the antenna community over the past few years, for applications such as wireless communication systems [1] [2], astronomical instrumentation [3], and security imaging [4].Therefore, the accurate modelling of the input impedance, the patterns and the mutual coupling is crucial for these applications. However, commercial solvers such as CST usually suffer from computation overhead and slow simulation for these specific problems. As a result, there is a demand for developing efficient tools to model those structures. The Physical Optics was introduced to study lens antennas in the milestone work of Rebeiz [5]. Since then high frequency techniques have been highly employed in lens antenna analysis [6] [7]. Several methods have been adopted by the Terahertz Sensing Group [1] to model these high frequency systems fast and accurately. In the more recent work of [8], a GO/FO tool is used to analyse the pattern, efficiency and directivity of quasi-optical systems. In [9], a GO/PO tool is developed to evaluate the mutual coupling between lenses using ray-tracing. However, the GO/PO technique is inaccurate when simulating small-size lenses. For instance, in [1] where a $2\lambda_0$ lens is used as the array element, as shown in Fig. 1.1a, and in [2] a $2\lambda_0$ lens is used as the core in the core-shell lens structure, Fig. 1.1b. Due to the relevance of small-size lenses, and due to the inaccuracy of the current analysis tools, a fast full-wave solver is needed to simulate such systems.

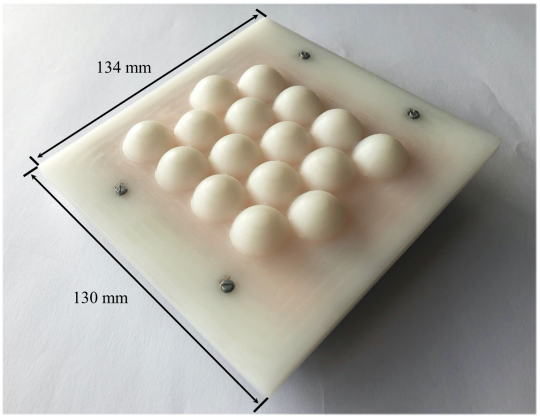

(a)

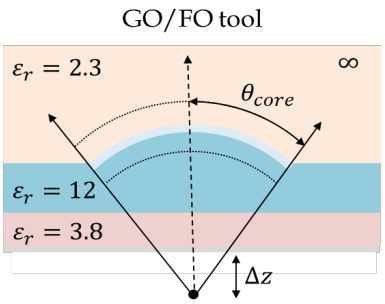

(b)

Figure 1.1: Applications using small lenses in (a) Phased array using $2\lambda_0$ lens as elements [1] and (b) Core-shell lens design for fly eyes applications [2]

[1] Terahertz Sensing Group, Department of Microelectronics, EEMCS, TUDelft. https://terahertz.tudelft.nl/

Both from a fundamental and an applicative point of view, there is the interest to characterise the emitted power generated by warm bodies. To this regard, the most relevant contribution is [10], that many authors have used to study the brightness of conductive bodies resorting to reciprocity, which allows replacing the emissivity of a body with its absorptivity under plane wave incidence. The direct emission of a thermally excited body has been only lightly discussed in the literature. For instance, [11] and [12] address the generation of electromagnetic energy from thermally excited bodies but fail to provide results from numerical simulations in the near fields. In view of this background, it is a matter of interest to characterize the radiation from conducting and semiconducting bodies, characterized by the Drude's model conductivity [13]. However, the literature lacks of full wave solvers allowing to simulate the thermal radiation from arbitrary geometries.

1.2. Proposed Method

The most popular three methods for numerical solvers are the Finite Difference Time Domain Method (FDTD), the Finite Element Method (FEM) and the Method of Moments (MoM). Although the FDTD is easy to implement, time domain solvers are not suitable to simulate problems with dimensions in the order of the wavelength (i.e., small lenses), and problems involving dispersive media (i.e., the dispersive conductivity used in radiometry). In turn FEM operates in the frequency domain [14], can handle material inhomogeneities, and operates with sparse matrices, which are fast to compute and easy to store and operate with. However the FEM requires additional boundary condition, i.e., the absorbing boundary conditions, to solve radiation problems. While the Volumetric Method of Moments (V-MoM) proposed in this thesis allows to solve problems at resonant sizes, exterior problems, to treat also inhomogeneous and dispersive media. The other advantage is that its fully occupied and large matrix is computed only once for a given problem, and can be handled in a fast solver such as the Conjugate Gradient-Fast Fourier Transform (CG-FFT) [15], that reduces the memory requirements and the computational complexity.

This thesis proposes a full-wave simulator, using the approach of equivalence theorem [16] and Volumetric Method of Moments (V-MoM) [17] to analyse high frequency structures, integrated in a GUI for user experience, where both scattering and transmission problems can be analysed. In the tool, the volume containing all the possible meshed bodies is defined, and discretized with a structured mesh. Then the reaction integrals are calculated over the mesh and used for all the bodies combined in the discretized volume. After that, the specific geometry is defined in the volume by using a combination of elementary shapes (sphere, cuboid, ellipsoid and cylinder) with an associated relative permittivity ε_r and conductivity σ. Then excitations such as plane wave sources, voltage gap generators or radiometry sources can be selected to excite the cuboids. The equivalent currents on the structure can be obtained by solving the linear system with an iterative method named CG-FFT to speed up the calculation. Then the equivalent currents are later used to derive results such as the scattered field, the directivity, the gain, the losses, the input impedances and the scattering parameters. One advantage of the approach is that due to the cuboid basis function, the calculation is high symmetrical and it is also possible to reuse the calculation of mutual impedances in homogenous space for the same discretization, thus making the tool efficient to use.

1.3. Thesis Outline

The thesis is structured as follows:

In Chapter 2 the volumetric equivalence theorem is applied to obtain the Electric Field Integral Equation (EFIE), on which the numerical method is based. The integral equation is then discretized, to allow a numerical solution with a linear system. At the end of the chapter the workflow of the tool is explained together with its advantages.

In Chapter 3, the self- and mutual-reaction integrals are derived for the chosen voxel discretization. Chapter 4 explains the parametrization of all the fundamental shapes is explained, together with the discrete port and plane wave excitation.

In Chapter 5, the solution of the linear system by means of the CG-FFT is explained.

In Chapter 6, the method is validated by comparison with the Mie series solution for the field scattered by a dielectric homogeneous and multilayer sphere. In the validation also a dipole-fed lens antenna is considered.

In Chapter 7 The thermal emission from a warm body is studied by first modelling the incoherent radiometric sources. After the validation, the tool is used to characterize the emission from lossy semiconductors.

Chapter 8 concludes the thesis and discusses the future work of this tool, including the pre-conditioner, periodic boundary conditions, the superconducting materials. Moreover, a manual of the GUI is attached in

Appendix F for users to learn about the tool efficiently.

2

Formulation

In this Chapter the Electric Field Integral Equation (EFIE) is obtained from the volumetric equivalence theorem and is later solved by the V-MoM.

In Sec. 2.1, the Electric Field Integral Equation is constructed using volume equivalence theorem. In Sec. 2.2, the MoM is applied to find the equivalent currents from the integral equation with a cuboid discretization. In Sec. 2.3, the overall structure of the tool is explained, including the advantages of the tool.

2.1. Construction of the Integral Equation

This section explains how to formulate the Electric Field Integral Equation by the application of the volume equivalence theorem [16], which sates the total electromagnetic field is unperturbed if a scatterer is substituted by equivalent electric and magnetic currents radiating in an homogenous space.

Let the electric and magnetic sources $\left(\vec{J}^i, \vec{M}^i\right)$, immersed in a homogenous medium of relative permittivity $\varepsilon_r^{\text{bg}}$, generate the fields $\left(\vec{E}^i(\vec{r}), \vec{H}^i(\vec{r})\right)$, that illuminate a body of volume $\mathcal{V}$, constituted by a material with a relative permittivity $\varepsilon_r(\vec{r})$, and a conductivity $\sigma(\vec{r})$ as shown in Fig. 2.1. The scattered field $\left(\vec{E}^s(\vec{r}), \vec{H}^s(\vec{r})\right)$ is generated by the interaction between the incident field and the scatterer. The total fields are the superposition of the incident and the scattered field as

$$\vec{E}(\vec{r}) = \vec{E}^i(\vec{r}) + \vec{E}^s(\vec{r}) \tag{2.1a}$$

$$\vec{H}(\vec{r}) = \vec{H}^i(\vec{r}) + \vec{H}^s(\vec{r}). \tag{2.1b}$$

Since the incident and the total field satisfy Maxwell's equations, one can write as follows

$$\vec{\nabla} \times \vec{H}^i(\vec{r}) = j\omega\varepsilon_0 \varepsilon_r^{\text{bg}} \vec{E}^i(\vec{r}) \tag{2.2a}$$

$$\vec{\nabla} \times \vec{E}^i(\vec{r}) = -j\omega\mu_0 \vec{H}^i(\vec{r}) \tag{2.2b}$$

$$\vec{\nabla} \times \vec{H}(\vec{r}) = \sigma(\vec{r})\vec{E}(\vec{r}) + j\omega\varepsilon_0\varepsilon_r(\vec{r})\vec{E}(\vec{r}) \tag{2.3a}$$

$$\vec{\nabla} \times \vec{E}(\vec{r}) = -j\omega\mu_0\mu_r(\vec{r})\vec{H}(\vec{r}). \tag{2.3b}$$

By defining the complex relative permittivity as

$$\varepsilon_{\text{eff}}(\vec{r}) = \varepsilon_r(\vec{r}) - \frac{j\sigma(\vec{r})}{\omega\varepsilon_0} \tag{2.4}$$

(2.3a) can be written as follows

$$\vec{\nabla} \times \vec{H}(\vec{r}) = j\omega\varepsilon_0\varepsilon_{\text{eff}}(\vec{r})\vec{E}(\vec{r}). \tag{2.5}$$

Subtracting (2.2a) from (2.5) and (2.2b) from (2.3b) respectively, combined with (2.1a) and (2.1b), one can get

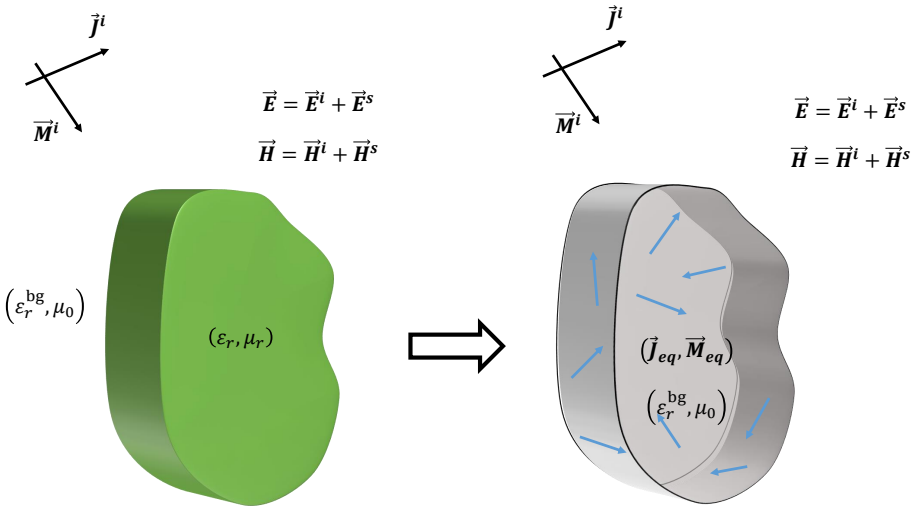

Figure 2.1: Graphical representation of the equivalence theorem

$$\begin{aligned}\vec{\nabla} \times \vec{H}^s(\vec{r}) &= j\omega\varepsilon_0(\varepsilon_{\text{eff}}(\vec{r}) - \varepsilon_{\text{eff}}^{\text{bg}})\vec{E}(\vec{r}) + j\omega\varepsilon_0\varepsilon_r\vec{E}^s(\vec{r}) \\ \vec{\nabla} \times \vec{E}^s(\vec{r}) &= -j\omega\mu_0(\mu_r(\vec{r}) - \mu_{\text{r}}^{\text{bg}})\vec{H}(\vec{r}) - j\omega\mu_0\vec{H}^s(\vec{r}).\end{aligned} \tag{2.6}$$

This implies that the scattered field $\left(\vec{E}^s(\vec{r}), \vec{H}^s(\vec{r})\right)$ can be replaced by the fields radiated by some equivalent currents $\vec{J}_{\text{eq}}(\vec{r})$ defined on the body. If $\mu_r = 1$, only the equivalent electric currents $\vec{J}_{\text{eq}}$ can be introduced and defined as follows

$$\vec{J}_{\text{eq}}(\vec{r}) = j\omega\varepsilon_0\left(\varepsilon_{\text{eff}}(\vec{r}) - \varepsilon_{\text{eff}}^{\text{bg}}\right)\vec{E}(\vec{r}) \tag{2.7}$$

Since the scattered field is the field produced by the equivalent current in the background medium, one can write as follows

$$\vec{E}^s(\vec{r}) = \iiint_{\mathcal{V}} \bar{\bar{G}}^{\text{hs}}(\vec{r}, \vec{r}') \cdot \vec{J}_{\text{eq}}(\vec{r}')\, d\vec{r}' \tag{2.8}$$

where $\bar{\bar{G}}^{\text{hs}}(\vec{r}, \vec{r}')$ is the dyadic Green's function of the homogeneous background medium defined in a coordinate free form as written in Appendix A. Substituting (2.7) and (2.8) into (2.1a), the latter can be written as follows

$$\vec{E}^i(\vec{r}) = \frac{\vec{J}_{\text{eq}}(\vec{r})}{j\omega\varepsilon_0\left(\varepsilon_{\text{eff}}(\vec{r}) - \varepsilon_{\text{eff}}^{\text{bg}}\right)} - \iiint_{\mathcal{V}} \bar{\bar{G}}^{\text{hs}}(\vec{r}, \vec{r}') \cdot \vec{J}_{\text{eq}}(\vec{r}')\, d\vec{r}'. \tag{2.9}$$

By defining a effective conductivity $\sigma_{\text{eff}}(\vec{r}) \equiv j\omega\varepsilon_0\left(\varepsilon_{\text{eff}}(\vec{r}) - \varepsilon_{\text{eff}}^{\text{bg}}\right)$, one can simplify the equation to

$$\vec{E}^i(\vec{r}) = \frac{\vec{J}_{\text{eq}}(\vec{r})}{\sigma_{\text{eff}}(\vec{r})} - \iiint_{\mathcal{V}} \bar{\bar{G}}^{\text{hs}}(\vec{r}, \vec{r}') \cdot \vec{J}_{\text{eq}}(\vec{r}')\, d\vec{r}'. \tag{2.10}$$

The analytical solution of (2.10) is not always available. Therefore, finding a numerical technique to solve the equation is essential to the problem. In the next section, a Method of Moment (MoM) is used as the numerical tool to estimate the solution of the equivalent current.

2.2. Solving the Integral Equation with MoM

As described in the MoM [17], the solution of the equivalent currents can be approximated by expanding the solution into a summation of basis functions

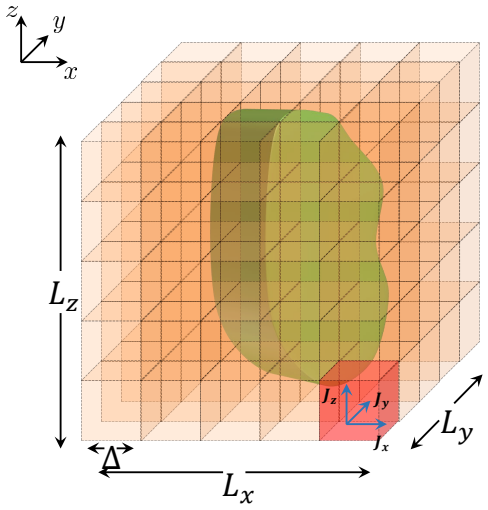

Figure 2.2: Graphical representation of the basis functions with three polarizations along x, y and z respectively

$$\vec{J}_{\text{eq}}(\vec{r}) = \sum_{n=1}^{N_t} i_n \vec{b}_n(\vec{r}). \tag{2.11}$$

Substituting (2.11) into (2.10) one can get

$$\vec{E}^i(\vec{r}) = \sum_{n=1}^{N_t} i_n \left(\frac{\vec{b}_n(\vec{r})}{\sigma_{\text{eff}}(\vec{r})} - \iiint_{\mathcal{V}_n} \bar{\bar{G}}^{\text{hs}}(\vec{r}, \vec{r}') \cdot \vec{b}_n(\vec{r}')\, d\vec{r}' \right). \tag{2.12}$$

Since the basis functions are known, the integral equations becomes a linear equation with N_t unknowns i_n. Therefore, a set of N_t linear equations are needed to find the solution of their weights. To obtain that number of linear equations, a linear operation called inner product defined as follows

$$\langle \vec{f}(\vec{r}), \vec{g}(\vec{r}) \rangle = \iiint_{\mathcal{V}} \vec{f}(\vec{r}) \cdot \vec{g}^*(\vec{r})\, d\vec{r} \tag{2.13}$$

is used to project both sides of (2.12) into the test functions $\vec{t}_m$, and obtaining as follows

$$\langle \vec{E}^i(\vec{r}), \vec{t}_m(\vec{r}) \rangle = \langle \sum_{n=1}^{N_t} i_n \left(\frac{\vec{b}_n(\vec{r})}{\sigma_{\text{eff}}(\vec{r})} - \iiint_{\mathcal{V}} \bar{\bar{G}}^{\text{hs}}(\vec{r}, \vec{r}') \cdot \vec{b}_n(\vec{r}')\, d\vec{r}' \right), \vec{t}_m(\vec{r}) \rangle \tag{2.14}$$

where $m = 1, \ldots, N_t$. Since the unknowns are the equivalent currents $\vec{J}_{\text{eq}}$, which are not subject to any continuity condition [18], for the sake of simplicity piecewise constant basis functions are being employed. Therefore, with this choice, the box of sides L_x, L_y, and L_z shown in Fig. 2.2 is discretized into N_s cuboids of edge Δ, where the current is considered to be constant. In each voxel the current is assumed to have an $x-$, a $y-$, and a $z-$component. The basis functions $\vec{b}_n$ have a unit of $[1/\text{m}^2]$ by the size of the basis functions Δ, so that combined with their weights i_n, the equivalent currents $\vec{J}_{\text{eq}}$ have a dimension of $[\text{A}/\text{m}^2]$.

With respect to this choice, the basis functions can be written as follows

$$\vec{b}_n(\vec{r}) = \frac{1}{\Delta^2} \text{rect}\left| \frac{\vec{r} - \vec{r}_n}{\Delta} \right| \hat{p}_n \tag{2.15}$$

where $\hat{p}_n \in \{\hat{x}, \hat{y}, \hat{z}\}$, with $n = 1, \ldots, N_t = 3N_s$. Since the Galerkin's method is used, the test functions are chosen as follows

$$\vec{t}_m(\vec{r}) = \vec{b}_m(\vec{r}). \tag{2.16}$$

Substituting (2.16) into the m-th equation of (2.13), one obtains as follows

$$\langle \vec{E}^i(\vec{r}), \vec{b}_m(\vec{r})\rangle = \langle \sum_{n=1}^{N_t} i_n \left(\frac{\vec{b}_n(\vec{r})}{\sigma_{\text{eff}}(\vec{r})} - \iiint_{\mathcal{V}_n} \bar{\bar{G}}^{\text{hs}}(\vec{r},\vec{r}') \cdot \vec{b}_n(\vec{r}')\, d\vec{r}' \right), \vec{b}_m(\vec{r})\rangle. \tag{2.17}$$

where $\mathcal{V}_n$ is the volume cotains the n-th basis function. Being the inner product a linear operator, (2.17) becomes as follows

$$\underbrace{\langle \vec{E}^i(\vec{r}), \vec{b}_m(\vec{r})\rangle}_{①} = \underbrace{\sum_{n=1}^{N_t} i_n \langle \frac{\vec{b}_n(\vec{r}), \vec{b}_m(\vec{r})\rangle}{\sigma_{\text{eff}}(\vec{r})}}_{②} - \underbrace{\langle \iiint_{\mathcal{V}_n} \bar{\bar{G}}^{\text{hs}}(\vec{r},\vec{r}') \cdot \vec{b}_n(\vec{r}')\, d\vec{r}', \vec{b}_m(\vec{r})\rangle}_{③}. \tag{2.18}$$

Part ① of (2.18) can be expressed as follows

$$\langle \vec{E}^i(\vec{r}), \vec{b}_m(\vec{r})\rangle = \iiint_{\mathcal{V}_m} \vec{E}^i(\vec{r}) \cdot \frac{1}{\Delta^2} \text{rect}\left| \frac{\vec{r}-\vec{r}_m}{\Delta} \right| \hat{p}_m d\vec{r} = \vec{E}^i(\vec{r}) \cdot \hat{p}_m \cdot \Delta = v_m \tag{2.19}$$

where v_m is the voltage impressed on the m-th basis function.
Part ② of (2.18) is

$$\frac{\langle \vec{b}_n(\vec{r}), \vec{b}_m(\vec{r})\rangle}{\sigma_{\text{eff}}(\vec{r})} = \iiint_{\mathcal{V}_m} \frac{1}{\Delta^2} \text{rect}\left| \frac{\vec{r}-\vec{r}_n}{\Delta} \right| \hat{p}_n d\vec{r} \cdot \frac{1}{\Delta^2} \text{rect}\left| \frac{\vec{r}-\vec{r}_m}{\Delta} \right| \hat{p}_m d\vec{r} = \frac{\delta_{nm}}{\sigma_n \Delta} \tag{2.20}$$

where δ_{nm} is the Kronecker delta, and σ_n is the effective conductivity of the n-th cell. Therefore the projection of (2.20) forms the diagonal matrix $\mathbf{Z}^{\text{mat}}$, defined as follows

$$\mathbf{Z}^{\text{mat}} = \text{diag}\left(\frac{1}{\sigma_1 \Delta}, \frac{1}{\sigma_2 \Delta}, \ldots, \frac{1}{\sigma_{N_t} \Delta} \right) \tag{2.21}$$

Part ③ of (2.18) is a double volume integration that describes the mutual coupling between the basis functions in homogenous space, which forms a radiation matrix $\mathbf{Z}^{\text{rad}}$ with entries defined as follows

$$Z_{mn} = \langle \iiint_{\mathcal{V}_n} \bar{\bar{G}}^{\text{hs}}(\vec{r},\vec{r}') \cdot \vec{b}_n(\vec{r}')\, d\vec{r}', \vec{b}_m(\vec{r})\rangle = - \iiint_{\mathcal{V}_m} \iiint_{\mathcal{V}_n} \bar{\bar{G}}^{\text{hs}}(\vec{r},\vec{r}') \cdot \vec{b}_n(\vec{r}') \cdot \vec{b}_m(\vec{r})\, d\vec{r}'\, d\vec{r} \tag{2.22}$$

Then the (2.14) can be written is matrix product form

$$\mathbf{v} = \left(\mathbf{Z}^{\text{mat}} + \mathbf{Z}^{\text{rad}} \right) \mathbf{i}. \tag{2.23}$$

2.3. Structure of the Tool

From the previous sections, it can be concluded that the V-MoM works in several steps. As illustrated in Fig. 2.3, in the first pre-computation stage, the space is divided into cubic sub-domains at the same size. Then the integrals are evaluated and used to fill in the radiation matrix. The material of the blocks and their excitation can be defined afterwards in the design stage. Then from (2.23) the weights of the basis function are obtained which are used to approximate the equivalent current. In the result stage, the scattered field is the same as the field radiated by the equivalent currents in homogenous space. The far field is calculated using homogenous space's Green's function and the near field is obtained according to the equivalence theorem (2.7).

Several advantages can be drawn from the V-MoM. First, the calculation of the radiation matrix is the most computational demanding part due to the 6-D integral. However, due to the symmetry of cuboid sampling of the grid and the fact that green's function only depends on the relative distance between the elements, one does not need to compute all the $9N_t^2$ 6-D reaction integrals but only a small part of it (about $2N_t$). Second, the symmetries also contributes to the solution of the linear system. To find the solutions, one can avoid inverting a large matrix by using an iterative method (CG-FFT) to speed up the calculation for large problems, which will be discussed in Ch. 5. Third, since the reaction integrals is calculated in homogenous space, the radiation matrix can be reused for the same grid by changing only the excitation and material matrix. This feature allows the increase of efficiency when designing different shapes within the same grid.

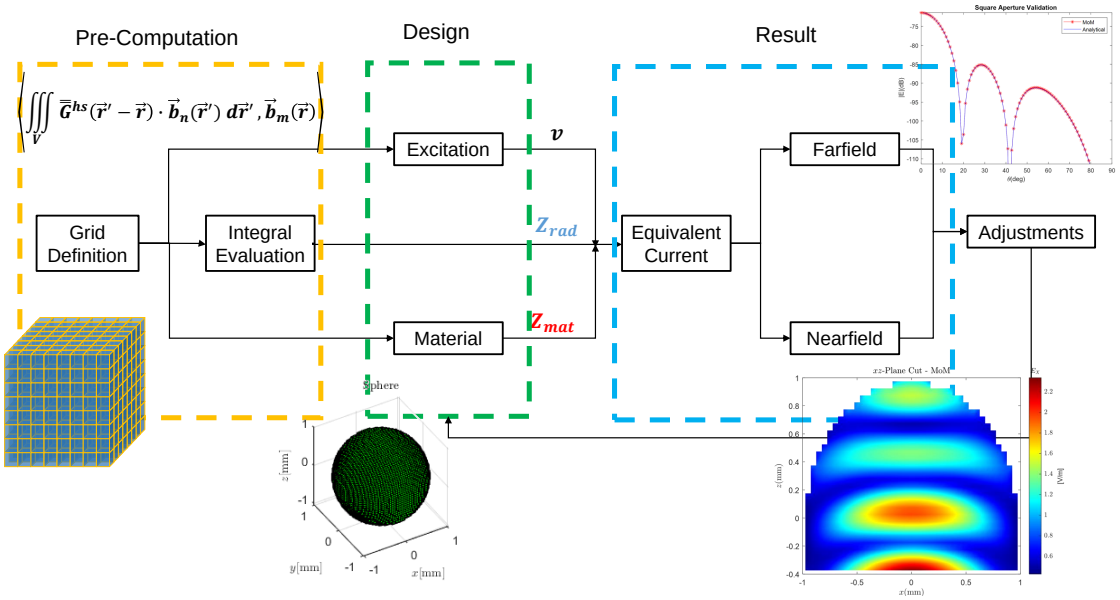

Figure 2.3: Structure of V-MoM.

3

Pre-Computation

This Chapter will describe how to generate the radiation matrix defined in (2.22). Sec. 3.1 contains the general requirements to calculate the grid such as the sampling and background material. Sec. 3.2 and 3.3 introduces how to compute the self and mutual reaction integrals respectively.

3.1. Definition of the Grid

The present V-MoM creates a structured mesh over the biggest volume of dimensions L_x, L_y, and L_z, along x, y, and z respectively, that contains all the bodies to simulate as shown in Fig. 3.1a. The volume is then discretized with cubes of edge Δ, as shown in Fig. 3.1b, in such a way that N_x, N_y, and N_z elements are present along the x, y, and z direction, with N_s elements per polarization and N_t total elements. The step size Δ is chosen according to the smallest simulated wavelength in the body, that depends both on the densest dielectric, and on the highest frequency under investigation, and it has to be suitable to reproduce the field variation inside all the possible meshed bodies. Generally it is chosen to be $\Delta < \lambda_d/10$ at least, and should be smaller for more complex problems.

The grid will be located in the origin of the reference system and be sampled along three dimensions from the minimum by x_s, y_s and z_s with

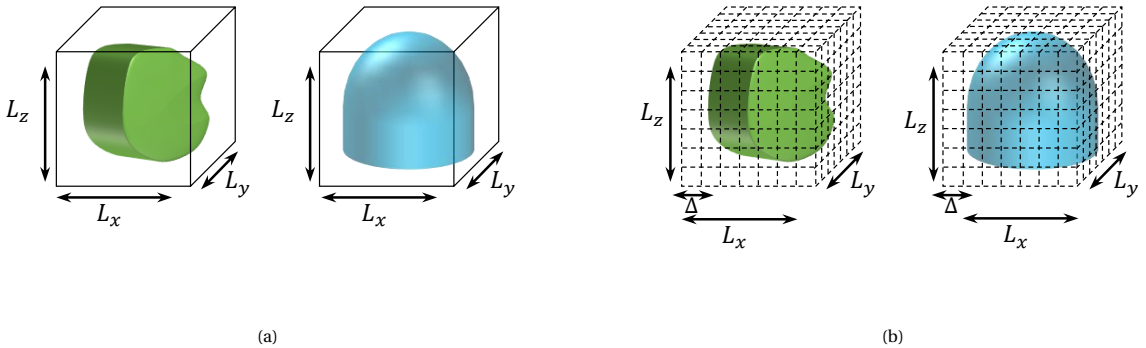

(a) (b)

Figure 3.1: (a) Cubic volume of size L_x, L_y and L_z containing the body. (b) Discretization of the volume with cubes of size Δ.

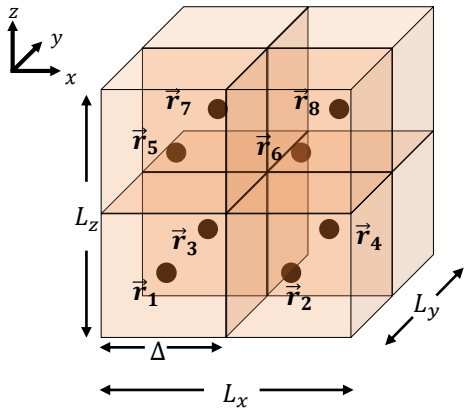

Figure 3.2: An example of a $2 \times 2 \times 2$ grid with sampling positions $\vec{r}_n$

$$
\begin{aligned}
x_s(n_x) &= -\frac{L_x}{2} - \frac{\Delta}{2} + n_x\Delta,\ n_x = 1, 2, \ldots, N_x \\
y_s(n_y) &= -\frac{L_y}{2} - \frac{\Delta}{2} + n_y\Delta,\ n_y = 1, 2, \ldots, N_y \\
z_s(n_z) &= -\frac{L_z}{2} - \frac{\Delta}{2} + n_z\Delta,\ n_z = 1, 2, \ldots, N_z.
\end{aligned} \tag{3.1}
$$

Fig. 3.2 shows an example of a $2\times2\times2$ grid with its sampling positions and ordering of $\vec{r}$ from 1-8. Once the grid is defined, the reaction integrals can be calculated for all the sampled points, regardless the material that a specific cell contains, even if a specific mesh cell does not contain any dielectric. In this case the solution for that cell is discarded by using the *masking* procedure explained in Sec. 5.1.

The structured mesh has several advantages. First, the structured grid is body independent and requires only once the calculation of the reaction integrals. Therefore, different bodies can be simulated in the same grid avoiding the re-computation of the integrals. Second, the position vectors can be represented by nodes in the fixed grid so that one does not need to store the vectors in the memory but only works with the indexes of the nodes. Third, the symmetries and uniform sampling of the grid leads to a Toeplitz property of the reaction integrals, which can be stored in a matrix-free form with low memory requirement and can be used to accelerate the calculation of the solution later discussed in Ch. 5.

However, the disadvantage of the fixed grid appears when the body does not conform to the cubic samplings. For example, Fig. 3.3 shows that for tilted bodies, curved bodies and bodies with a resolution smaller than the mesh are not well represented in the grid. This problem can be solved by tapering the ε_{eff} of the unit cell according to the ratio between the volume that the body occupies in the cell and the total volume of the cell. Another drawback of this is that the fixed grid can not model fine detailed structures and large bodies at the same time, as it requires different levels of discretization for detailed and large bodies.

3.2. Self Reaction Integrals

Once the grid properties are defined, the entries of the radiation matrix $\mathbf{Z}^{\text{rad}}$ are calculated. The reaction integrals can be divided into two categories: the self reaction integrals ($m = n$) and the mutual reaction integrals ($m \neq n$). This sub-section will discuss how to calculate the first case.

According to eq. (2.37), when $m = n$, the integral becomes as follows

$$
Z_{nn} = -\langle \iiint_{V_n} \bar{\bar{G}}^{\text{hs}}(\vec{r}, \vec{r}\,') \cdot \vec{b}_n(\vec{r}\,')\, d\vec{r}\,', \vec{b}_n(\vec{r}) \rangle \tag{3.2}
$$

which is the electric field inside the source region projected on the basis function in that region. According to Appendix B, the field inside the source region can be written in three contributions and (3.2) is expressed as

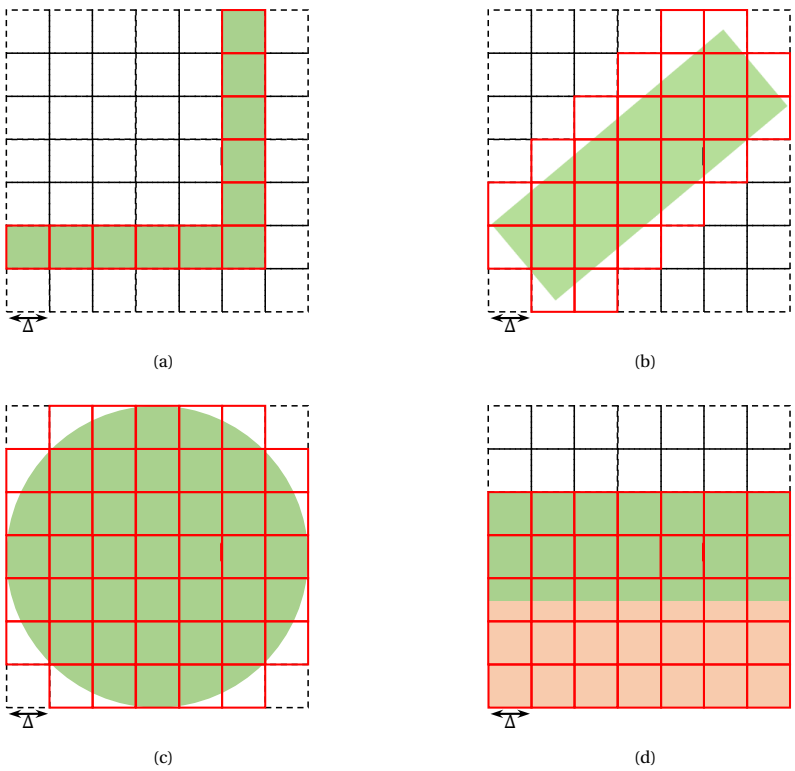

Figure 3.3: (a) A body that conforms to the sampling, and (b) a tilted cuboid, (c) a sphere and (d) two slabs a finer resolution that does not conform to the sampling

follows

$$\begin{aligned} Z_{nn} = &-\langle \iiint_{\mathcal{V}_n - \mathcal{V}_\delta} \bar{\bar{G}}^{\mathrm{hs}}\left(\vec{r},\vec{r}\,'\right)\cdot\vec{b}_n\left(\vec{r}\,'\right)d\vec{r}\,', \vec{b}_n\left(\vec{r}\right)\rangle - \frac{1}{j\omega\varepsilon_0}\left(\frac{2}{3}e^{-jka}\left(1+jka\right)-1\right)\langle \vec{b}_n\left(\vec{r}\right), \vec{b}_n\left(\vec{r}\right)\rangle \\ &-\langle \iiint_{\mathcal{V}_\delta} \bar{\bar{G}}^{\mathrm{hs}}\left(\vec{r},\vec{r}\,'\right)\cdot\left(\vec{b}_n\left(\vec{r}\,'\right)-\vec{b}_n\left(\vec{r}\right)\right)d\vec{r}\,', \vec{b}_n\left(\vec{r}\right)\rangle \end{aligned} \tag{3.3}$$

where a is radius of the sphere region enclosing the source region and $\mathcal{V}_\delta$ is the volume of the spherical region. Due to the definition of the basis functions in (2.15), the third term of (3.3) vanishes, and by calculating the second projection, it becomes as follows

$$Z_{nn} = -\langle \iiint_{\mathcal{V}_n - \mathcal{V}_\delta} \bar{\bar{G}}^{\mathrm{hs}}\left(\vec{r},\vec{r}\,'\right)\cdot\vec{b}_n\left(\vec{r}\,'\right)d\vec{r}\,', \vec{b}_n\left(\vec{r}\right)\rangle - \frac{1}{j\omega\varepsilon_0\Delta}\left(\frac{2}{3}e^{-jka}\left(1+jka\right)-1\right) \tag{3.4}$$

The projection in (3.4) can be calculated numerically, by discretizing the mesh cell into smaller cubic subdomains of edge ℓ, leading to the following expression

$$Z_{nn} = -\frac{\ell^6}{\Delta^4}\sum_{l,p,q}\sum_{\substack{l',p',q' \\ \neq \\ l,p,q}} \bar{\bar{G}}^{\mathrm{hs}}\left(\vec{r}_{l,p,q},\vec{r}_{l',p',q'}\right) - \frac{1}{j\omega\varepsilon_0\Delta}\left(\frac{2}{3}e^{-jk\left(\frac{3}{4\pi}\right)^{\frac{1}{3}}\ell}\left(1+jk\left(\frac{3}{4\pi}\right)^{\frac{1}{3}}\ell\right)-1\right) \tag{3.5}$$

where a is chosen to be $a = \ell\,(4\pi/3)^{-1/3}$ to obtain the same volume as the sub-discretized cells.

3.3. Mutual Reaction Integrals

For $m \neq n$ case, the mutual coupling between m-th basis and n-th basis function can be illustrated in Fig. 3.4, where $\mathcal{V}_n$ is considered as the source region and $\mathcal{V}_m$ represents the observation region in the figure.

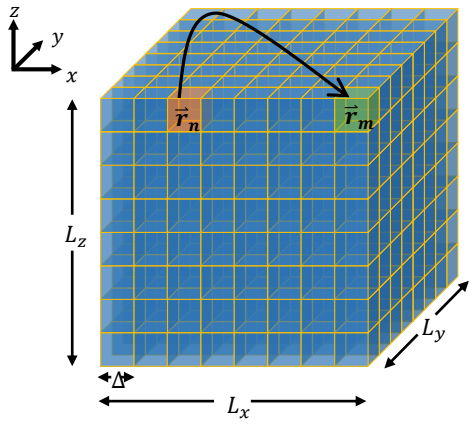

Figure 3.4: Graphical representation of mutual reaction integrals between m-th and n-th basis function

When the basis functions are close, the integrals are evaluated near the singularity. Therefore, to increase the accuracy of the computation of the mutual reaction integrals while avoiding waste of computation power, the calculations of Z_{mn} are split into two different categories as shown in Fig. 3.5. Fig. 3.5a shows the first case for basis functions are close. Here both the source and observation regions are sampled with sub-meshes since they are near the singularity. Another reason to calculate the close mutual reaction integrals accurately is that they have the largest value among the mutual integrals and thus, having a large impact on the radiation matrix. In Fig. 3.5b, where the source and observation regions are far away, the integrals are replaced by a point-to-point interactions between $\mathcal{V}_m$ and $\mathcal{V}_n$ times the volume, since the field is small and can be approximated as constant in the far regions.

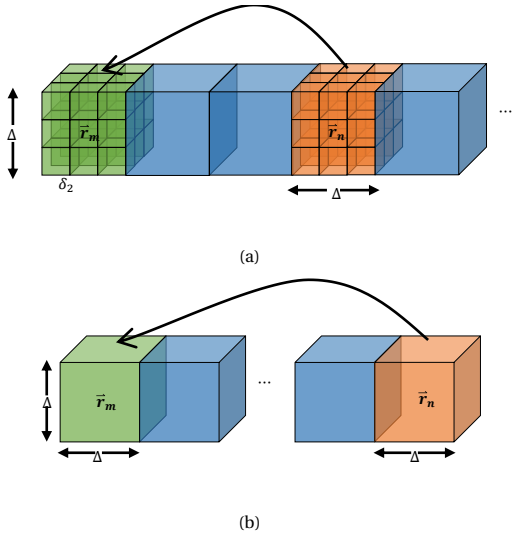

Figure 3.5: Mutual reaction integral calculations for (a) nearby elements and (b) far elements

For the nearby elements, the integrals are calculated numerically in (3.6) by discretizing the source and observation regions into $l_0 \times p_0 \times q_0$ sub-meshes with a size of ℓ.

$$Z_{mn} = -\frac{\ell^6}{\Delta^4} \sum_{l,p,q}^{l_0,p_0,q_0} \sum_{l',p',q'}^{l_0,p_0,q_0} \bar{\bar{G}}^{\mathrm{hs}}\left(\vec{r}_m\left(l,p,q\right), \vec{r}_n\left(l',p',q'\right)\right) \cdot \hat{p}_m \cdot \hat{p}_n. \tag{3.6}$$

For the far elements the mutual reaction integrals Z_{mn} can be simplified as

$$Z_{mn} = -\Delta^2 \bar{\bar{G}}^{\mathrm{hs}}\left(\vec{r}_m, \vec{r}_n\right) \cdot \hat{p}_m \cdot \hat{p}_n. \tag{3.7}$$

Note that one does not need to calculate all the mutual reactions due to the symmetries of cuboid sampling of the basis functions. The symmetries will be explored more in Ch. 5 with the CG-FFT method.

4

User's Design

After the grid is defined and the radiation matrix is computed, users will be able to design their desired structures by filling the material matrix $\mathbf{Z}^{\text{mat}}$ and excitation term $\mathbf{v}$. This chapter explains how the user can interact with the tool in terms of structure modelling and excitation. Sec 4.1 introduces the parametrization of four commonly used shapes. In Sec 4.2 and 4.3, plane wave and discrete port excitation are discussed for scattering and transmission problems. Sec. 4.4 will briefly introduce how to include radiometric sources in the tool. Sec. 4.5 discusses the possibility to customize the simulation with user defined files.

4.1. Modelling Structures

Four commonly used shapes are modelled in this tool, namely the cuboid, the ellipsoid, the sphere and the cylinder. These shapes are composed by cuboid basis function with position vector $\vec{r}$ that satisfy the parametric equations as shown in Fig. 4.1

4.1.1. Parametrization of Shapes

Sphere. As discussed in Ch. 3, the position vectors of the samples are written in Cartesian form as

$$\vec{r} = \begin{bmatrix} x_s \\ y_s \\ z_s \end{bmatrix} \tag{4.1}$$

The points located inside a sphere of radius a, and located at the origin as shown in Fig. 4.2a, are the ones which satisfy the following relation

$$\frac{x_s^2}{a^2} + \frac{y_s^2}{a^2} + \frac{z_s^2}{a^2} \leq 1. \tag{4.2}$$

Moreover, a truncation angle $\theta \in (0, \pi)$ is defined to truncate the sphere in horizontal planes. A sphere is truncated to a hemisphere, for example , when $\theta = \pi/2$. This additional bound is

$$z_s \geq a\cos\theta. \tag{4.3}$$

Cuboid. The points inside a cuboid of size L, W and H along x-, y-, and z-axis respectively, and centred at the origin, as shown in Fig. 4.2b, are given by

$$\begin{cases} |x_s| \leq \frac{L}{2} \\ |y_s| \leq \frac{W}{2} \\ |z_s| \leq \frac{H}{2} \end{cases}. \tag{4.4}$$

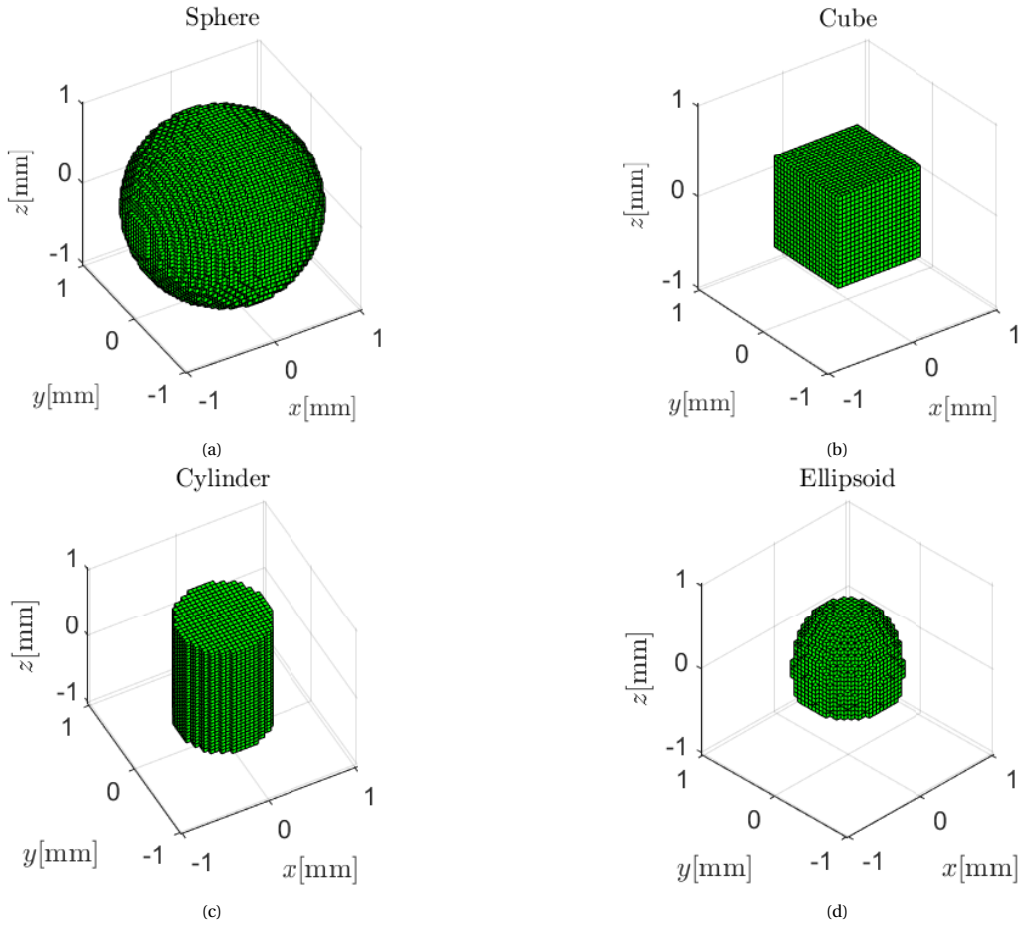

Figure 4.1: An example of the sampling of (a) a sphere with 1mm radius, (b) a 1mm × 1mm × 1mm Cuboid, (c) a cylinder with 0.5mm radius and 1.5mm height and (d) an ellipsoid with 0.7 eccentricity, 1mm diameter and 63° truncation angle

Cylinder. The points located inside a cylinder of radius a, height h with its axis parallel to the z-axis and its centre located at the origin, as shown in Fig. 4.2c, are given by

$$\begin{cases} \frac{x_s^2}{a^2} + \frac{y_s^2}{a^2} \leq 1 \\ \\ |z_s| \leq \frac{h}{2} \end{cases} . \tag{4.5}$$

Ellipsoid. In this tool, elliptical lenses are defined by their diameter D, their relative permittivity ε_r and their truncation angle $\theta \in (0, \pi)$ as shown in Fig. 4.2d. And the eccentricity is given by $e = 1/\sqrt{\varepsilon_r}$. Then the semi axes can be derived from these three parameters by

$$r_{\min} = \frac{D}{2\sin\theta_{\text{tr}}} \tag{4.6}$$

where $r_{\min}$ is the minimum distance from the lower focus to the surface of the lens.

$$r_{\min} = a\frac{1-e^2}{1-e\cos\theta_{\text{tr}}}. \tag{4.7}$$

Then the semi-major axis can be calculated by

$$a = r_{\min}\frac{1-e\cos\theta_{\text{tr}}}{1-e^2}. \tag{4.8}$$

The foci and semi-minor axis then is expressed as

$$c = a \cdot e \tag{4.9}$$

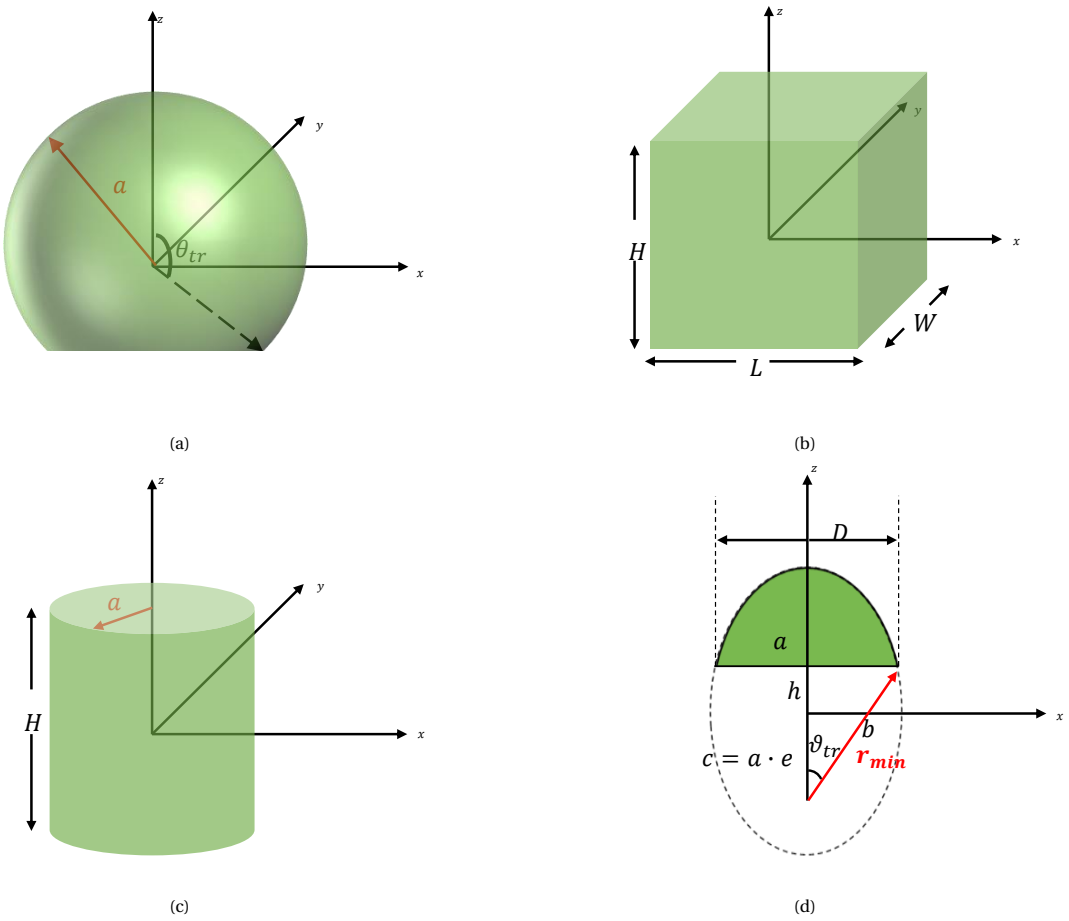

Figure 4.2: Graphical representation of the parametrization of a (a) sphere, (b) cube, (c) cylinder and (d) ellipsoid

$$b = \sqrt{a^2 - c^2}. \tag{4.10}$$

The lower limit for the lens will be h, where

$$h = \frac{D}{2\tan\theta_{\text{tr}}} - c. \tag{4.11}$$

Therefore, the points inside a truncated elliptical lens located at the origin are given by

$$\begin{cases} \frac{x_s^2}{b^2} + \frac{y_s^2}{b^2} + \frac{z_s^2}{a^2} \leq 1 \\ \\ z_s \geq h \end{cases}. \tag{4.12}$$

4.1.2. Displacement and Rotation

Normally one finds the positions of th structures from the parametric equations and then performs displacement or rotation on them. However, since the grid is fixed in he tool, mapping the positions after rotation to the samples also takes computation power. Hence this tool displaces and rotates the grid samples instead. Suppose one wants to displace the centre of a structure by a vector $\vec{r}_d$,

$$\vec{r}_d = \begin{bmatrix} x_d \\ y_d \\ z_d \end{bmatrix}. \tag{4.13}$$

Then the grid samples will first be shifted to $\vec{r}\,'$

$$\vec{r}\,' = \vec{r} - \vec{r}_d. \tag{4.14}$$

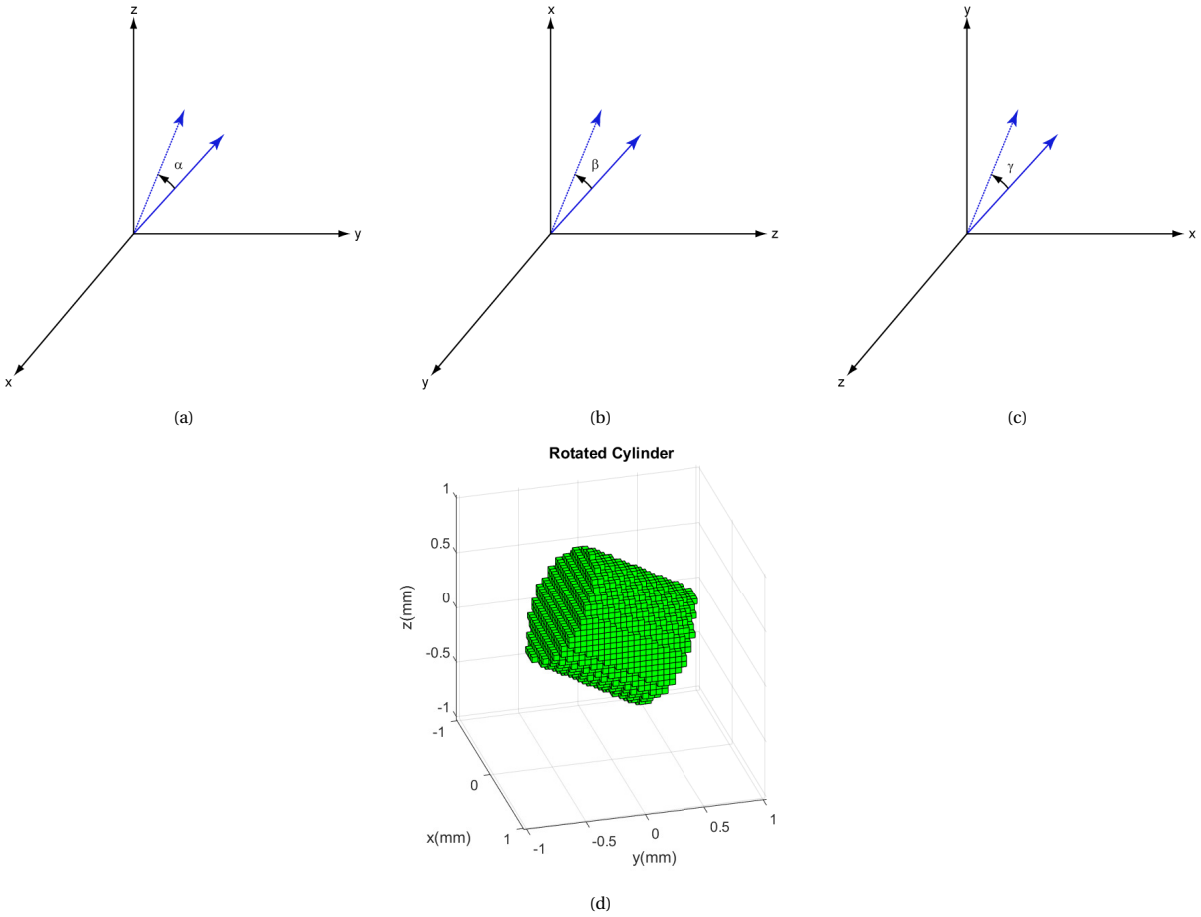

Figure 4.3: Definition of rotation angle (a) α along x-axis, (b) β along y-axis and (c) γ along z-axis and (d) an example of a cylinder is rotated along x-axis for 60 deg

To rotate the structure along x,y and z axis by α, β and γ respectively, one needs to rotate the coordinate system by $-\alpha$, $-\beta$ and $-\gamma$, where α, β and γ are defined as the counterclockwise rotation along axis according to the built-in functions in MatLab [19] in Fig. 4.3a, 4.3b and 4.3c. The rotated grid can be expressed as

$$\vec{r}\,'' = R_x\left(-\gamma\right) R_y\left(-\beta\right) R_z\left(-\alpha\right) \vec{r}\,' \tag{4.15}$$

where $R_x\left(-\alpha\right)$, $R_y\left(-\beta\right)$ and $R_z\left(-\gamma\right)$ are rotation matrices defined as

$$\begin{aligned} R_x\left(\alpha\right) &= \begin{bmatrix} 1 & 0 & 0 \\ 0 & \cos\alpha & -\sin\alpha \\ 0 & \sin\alpha & \cos\alpha \end{bmatrix} \\ R_y\left(\beta\right) &= \begin{bmatrix} \cos\beta & 0 & \sin\beta \\ 0 & 1 & 0 \\ -\sin\beta & 0 & \cos\beta \end{bmatrix} \\ R_z\left(\gamma\right) &= \begin{bmatrix} \cos\gamma & -\sin\gamma & 0 \\ \sin\gamma & \cos\gamma & 0 \\ 0 & 0 & 1 \end{bmatrix} \end{aligned} . \tag{4.16}$$

Fig. 4.3d is an example of a cylinder with 0.5mm radius and 1mm height rotated 60 deg along x-axis and shifted 0.2mm along $+\hat{z}$.

4.1.3. Material

After a structure is modelled with the indexes of the samples $\vec{r}_n$, the material of the structure (ε_r, σ) is defined on the corresponding basis functions, generating the material matrix $\mathbf{Z}^{\text{mat}}$. The undefined basis functions are filled with zeros, which will be masked at later stages.

4.2. Plane Wave Excitation

For plane wave scattering problem, the excitation $\mathbf{v}$ is provided by the incident field of the plane wave. Assuming a plane wave travelling from (θ, ϕ), as shown in Fig. 4.4, the propagation direction of the plane wave can be written as

$$\hat{k}_{\text{PW}} = -\left(\sin\theta\cos\phi\hat{x} + \sin\theta\sin\phi\hat{y} + \cos\theta\hat{z}\right). \tag{4.17}$$

By assuming the normal $\hat{n}_s = +\hat{z}$, for TE-polarized plane wave, the electric field is polarized as follows

$$\hat{E}_{\text{TE}} = \frac{\hat{k}_{\text{PW}} \times \hat{z}}{\left|\hat{k}_{\text{PW}} \times \hat{z}\right|} = \frac{-\sin\theta\sin\phi\hat{x} + \sin\theta\cos\phi\hat{y} + 0\hat{z}}{|\sin\theta|} = -\sin\phi\hat{x} + \cos\phi\hat{y} + 0\hat{z}. \tag{4.18}$$

if $\theta \neq 0$. Since $\hat{E}_{\text{TE}}$ is perpendicular to the direction of propagation, the unit vector of TM polarization is just the product between $\hat{E}_{\text{TE}}$ and $\hat{k}_{\text{PW}}$, where the TM-component can be expressed as

$$\hat{E}_{\text{TM}} = \hat{E}_{\text{TE}} \times \hat{k}_{\text{PW}} = \hat{k}_{\text{PW}} \times \hat{z} \times \hat{k}_{\text{PW}} = -\cos\theta\cos\phi\hat{x} - \cos\theta\sin\phi\hat{y} + \sin\theta\hat{z}. \tag{4.19}$$

For the broadside incidence case ($\theta = 0$), the definition for TE and TM polarization is not unique so the user can control the polarizations using ϕ and the amplitudes of each polarization. For example, if $\phi = \phi_{\text{in}}$, the tool will recognize TM polarization has a direction of $\hat{x}$ and TE as $\hat{y}$ with a rotation of ϕ_{in}. The overall expression of the electric field is written as

$$\vec{E}^{\text{in}}(\hat{r}) = \left(|E_{\text{TM}}|\,\hat{E}_{\text{TM}} + |E_{\text{TE}}|\,\hat{E}_{\text{TE}}\right) e^{-j\hat{k}_{\text{PW}}\cdot\hat{r}}. \tag{4.20}$$

Once the incident field is known, the excitation of the linear system can be derived as

$$\mathbf{v} = \begin{bmatrix} \Delta\vec{E}^{\text{in}}(\vec{r}_1)\cdot\hat{p}_1 \\ \Delta\vec{E}^{\text{in}}(\vec{r}_2)\cdot\hat{p}_2 \\ \vdots \\ \Delta\vec{E}^{\text{in}}\left(\vec{r}_{N_t}\right)\cdot\hat{p}_N \end{bmatrix} \tag{4.21}$$

where $\hat{p}_n$ is the polarization of the n-th basis functions.

4.3. Discrete Port

For active problems, the tool supports the use of discrete ports with source impedance Z_s to represent the impressed field in a certain cuboid region. Assume that one wants to excite a volume $\mathcal{V}_{\text{in}}$ with a voltage V_{in} oriented along the direction $\hat{p}_{\text{ex}}$ over a length d. The corresponding incident electric field can be written as follows

$$\vec{E}^{\text{in}}(\vec{r}) = \frac{V_{\text{in}}}{d}\hat{p}_{\text{ex}}, \text{ for } \vec{r} \in \mathcal{V}_{\text{in}}. \tag{4.22}$$

According to the definition of the incident voltage given in (2.23), and according to the choice of the used basis function, the projection of the incident field $\vec{E}^{\text{in}}$ into the n-th basis function $\vec{b}_n$ can be written as follows

$$v_n = \langle\vec{E}^{\text{in}}(\vec{r}), \vec{b}_n(\vec{r})\rangle = \iiint_{\mathcal{V}_n} \frac{V_{\text{in}}}{d}\frac{1}{\Delta^2}\text{rect}\left|\frac{\vec{r}-\vec{r}_n}{\Delta}\right|\hat{p}_{\text{ex}}\cdot\hat{p}_n d\vec{r} = \begin{cases} \frac{V_{\text{in}}\Delta}{d}\hat{p}_{\text{ex}}\cdot\hat{p}_n, & \text{if } \mathcal{V}_n \in \mathcal{V}_{\text{in}} \\ 0 \quad \text{otherwise.} \end{cases} \tag{4.23}$$

For $Z_s \neq 0$, the system is excited the same way with a correction of the results in the post processing stage. Figure shows a simple example of exciting a dipole oriented along x-axis with a voltage V_{in}. The gap is one basis function long i.e. $d = \Delta$ at $\vec{r}_8$ so only one sample is excited along $\hat{x}$ direction without $\hat{y}$ and $\hat{z}$ components. The excitation term will be $\mathbf{v}(8) = V_{\text{in}}$ with the rest elements equal to zero.

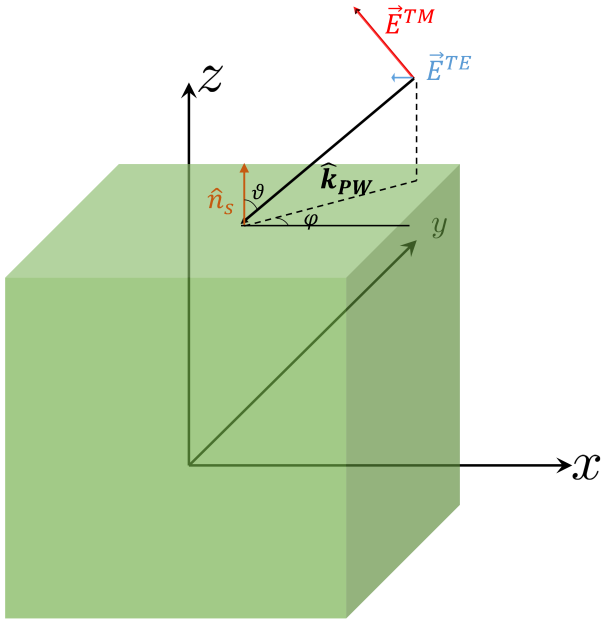

Figure 4.4: Graphical representation of a plane wave incidence from θ and ϕ

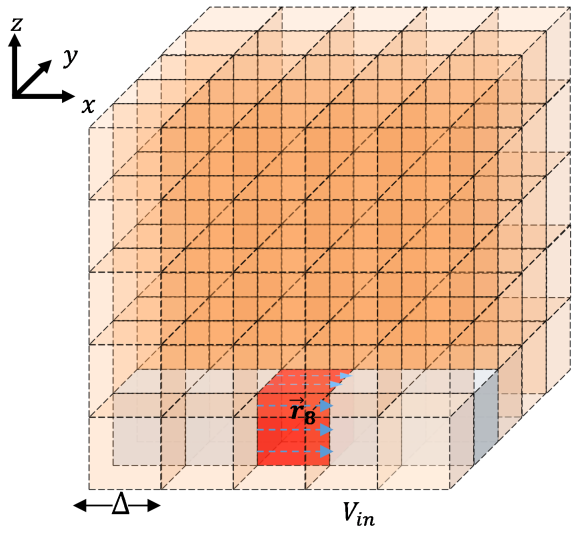

Figure 4.5: A simple example of exciting a dipole with a gap Δ

4.4. Radiometric Sources

A feature which has not been added into the GUI but already implemented in MATLAB script is radiometry properties for semi conductors. In Drude model [13], the conductivity of a material is considered as frequency dependent, which follows the relation

$$\sigma(\omega) = \frac{\sigma_{\text{qs}}}{1 + j\omega\tau} \tag{4.24}$$

where σ_{qs} is called the quasi static part of conductivity and τ is the scattering time of the material.

The structure then can be defined in the whole grid with a Drude model material $(\varepsilon_r, \sigma(\omega))$. The excitation is filled by radiometric sources for all polarizations at everywhere with an arbitrary phase:

$$v_{x,y,z}(\vec{r}_n) = \sqrt{\Re\left\{\frac{4k_B T}{\Delta\sigma_{\text{eff}}}\right\}} e^{j\phi_n} \tag{4.25}$$

where $\vec{r}_n \in \mathcal{V}$ and $\sigma_{\text{eff}} = j\omega\varepsilon_0\left(\varepsilon_r - \varepsilon_r^{bg}\right) + \sigma(\omega)$. Then the power radiated by such structure at a certain temperature T can be derived by evaluating the scattered power from the equivalent sources with the superposition of multiple simulations. More details regarding to radiometry problems are explained in Ch. 7.

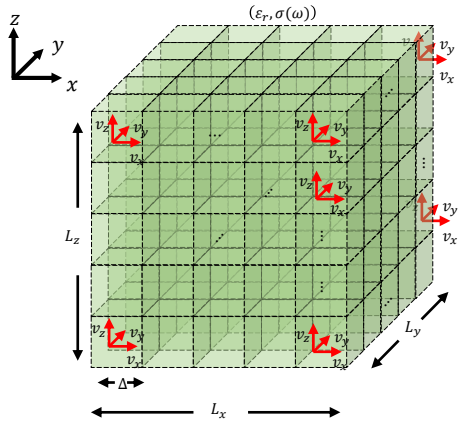

Figure 4.6: An example of simulating radiometry problems with the tool

4.5. Customization

For simplicity, the tool only parametrize four basic shapes that are commonly used in antennas. However, there are more complex structures that can be achieved. First, the tool supports overlaps between the structures, where later added shapes will overwrite the ones that are added previously with new material information if they overlap. Users may use this feature to create combination of shapes or subtraction of shapes by overwriting using a shape with background material. An example of this is the matching layer for lens antennas. Moreover, customized shapes are also possible by simply importing pre-defined indexes of the samples from files with recognizable format.

Other parts users can design, as shown in Fig. 2.3, are the excitation term and the material matrix. It is possible to introduce other material models, such as the Drude's model in the script. Field sources can be imported to fill the excitation terms also from a file with specific format. Overall, the tool is flexible and easy to implement updates.

5

Solution of Equivalent Currents

Solving a large-scale system such as $\mathbf{v} = \left(\mathbf{Z}^{\text{mat}} + \mathbf{Z}^{\text{rad}}\right)\mathbf{i}$ is not trivial. Fortunately, it is possible to exploit a fast solver, thanks to the properties introduced by the uniform sampling of the grid. Sec 5.1 introduces an iterative technique called Conjugate Gradient Fast Fourier Transform (CG-FFT) that allows to solve the linear system more efficiently in terms of computation time and memory requirements. Sec. 5.2 explains how the results (i.e., near fields, radiated and lost power, circuit parameters, and far field patterns) are derived from the equivalent currents is explained.

5.1. CG-FFT

5.1.1. Strategies to Solve Linear Systems

Several different techniques are suitable to solve (2.23).

Inversion. The most immediate one is the direct inversion which is discouraged due to the complexity of $\mathcal{O}\left(N_t^3\right)$, and to the low accuracy, therefore it is rarely used in numerical codes. It also requires the full storage of the matrix, i.e., N_t^2 entries to be saved.

LU Factorization. A more practical method is the LU factorization, where the matrix that defines the linear system is factorized into an upper-triangular (U) and a lower-triangular matrix (L). After the matrix has been factorized, the system can be solved through the solution of a triangular-like linear system. The matrix is factorized with a complexity of $\mathcal{O}\left(2N_t^3/3\right)$, and the triangular system can be solved with the complexity of $\mathcal{O}\left(N_t^2\right)$. This approach is particularly convenient if a larger number of linear systems with the same matrix but different forcing terms have to be solved. The matrix can be factorized only once, and all the different systems can be solved with N_t^2 operations. However, it requires storing N_t^2 entries of the factor matrices.

Iterative Methods. Iterative methods such as the Conjugate Gradient (CG) and its derivations such as the Conjugate Gradient Squared (CGS), the BiConjugate Gradient Squared (BiCG), and the Biconjugate Gradient Stabilized (BiCG-Stab) can be used to solve linear systems. These iterative methods converge to the solution through successive approximations. In exact arithmetic, N_t steps are required to converge to the exact solution. For the full treatise, we suggest reading the dedicated section of [15]. The principle behind the CG approach is not to solve the linear system directly but to define a functional whose minimum is the same as the solution of the system itself. The minimum is searched through an iterative approach, illustrated in Fig. 5.1, starting from the initial guess $\mathbf{i}^{(1)}$ of step 1. At the $(k+1)$-th step the solution $\mathbf{i}^{(k+1)}$ is be expressed as:

$$\mathbf{i}^{(k+1)} = \mathbf{i}^{(k)} + \alpha^{(k)}\mathbf{p}^{(k)} \tag{5.1}$$

where $\mathbf{i}_k$ is the solution of step k, $\mathbf{p}_k$ is the search direction, and α_k is a parameter that describes the movement along $\mathbf{p}_k$. The computations of $\mathbf{p}_k$ and α_k depend on the specific implemented algorithm, [15]. Moreover at each step matrix-vector multiplications are performed to compute the residual vector $\mathbf{r}_k$ defined as:

$$\mathbf{r}^{(k)} = \mathbf{v} - \underbrace{\mathbf{Z}^{\text{mat}} \cdot \mathbf{i}^{(k)}}_{①} - \underbrace{\mathbf{Z}^{\text{rad}} \cdot \mathbf{i}^{(k)}}_{②}. \tag{5.2}$$

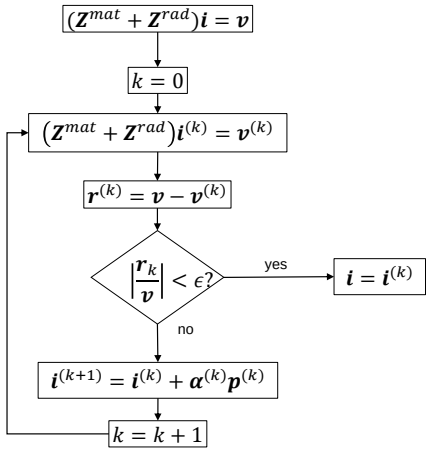

Figure 5.1: Flow chart diagram of CG algorithm for solving the linear system

The residual represents the error, component by component, for which the $\mathbf{i}^{(k)}$ solution of the linear system approximates the exact solution $\mathbf{i}$. Being the CG an iterative method, a new solution is searched until $||\mathbf{r}^{(k)}||/\|\mathbf{v}\| < \epsilon$, where $\|\cdot\|$ is the norm defined in the space vector and ϵ is the the tolerance required for the solution. In electromagnetic, the typical values for the tolerances are 10^{-3} for scattering problems and 10^{-4} for the input impedance calculation. The CG converges to the solution with n_s steps, where usually n_s is orders of magnitude smaller than the number of unknowns N_t. The CG calculates the residual (5.2) n_s times, and this aspect is the main computational effort of the method. Since the product ① of (5.2) is the product between a diagonal matrix and a vector, only N_t operations are required (i.e. element-wise multiplication). Product ② instead is the product between the full matrix $\mathbf{Z}^{\text{rad}}$ and the vector $\mathbf{i}^{(k)}$, and it requires N_t^2 operations if performed in the "traditional" manner. Therefore the complexity of each CG step is $\mathcal{O}\left(N_t^2\right)$, and since n_s are required for the convergence, the overall complexity of the method is $\mathcal{O}\left(n_s N_t^2\right)$. From this computational complexity analysis, it can be easily inferred that the computation of ② is the bottleneck for the CG. Moreover, it has to be stated that along with the complexity, the required memory is still N_t^2, which is prohibitive for any large-scale problem. The results described in this document aim first at making the memory requirements proportional to the number of unknowns N_t (instead of N_t^2) by storing only a part of $\mathbf{Z}^{\text{rad}}$ and then at reducing the complexity at which the product ② is computed.

It can be demonstrated that in the case of a uniform sampling, the matrix $\mathbf{Z}^{\text{rad}}$ is a Toeplitz matrix, which benefits from properties that allow us to reduce the memory requirements and the computational complexity significantly.

5.1.2. Toeplitz Matrix - Vector Product with Fast Fourier Transform

In this sub-section, the general properties of Toeplitz matrices are explained from a mathematical point of view and the aspects concerning the electromagnetic modelling are emphasized.

In the first place, these aspects are analysed for linear geometries and then extended to planar and volumetric structures

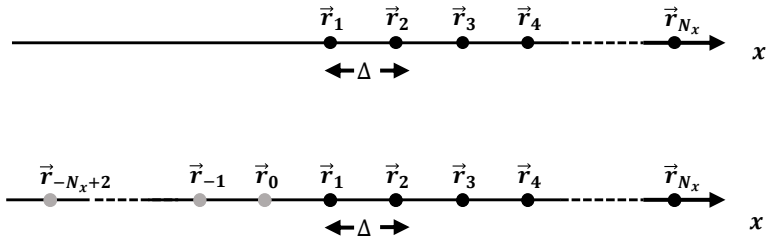

Figure 5.2: Geometry of N_x equispaced sources distributed along x-axis, and geometry of N_t equispaced sources distributed along x-axis and their cyclical extension (in grey).

One Dimensional Case

Let us assume a linear geometry of N_x equispaced basis functions as shown in Fig. 5.2. The associated impedance matrix $\mathbf{Z}^{\text{rad}}$ can be written as:

$$\mathbf{Z}^{\text{rad}} = \begin{bmatrix} z_{11} & z_{12} & z_{13} & \cdots & z_{1N_x} \\ z_{21} & z_{22} & z_{23} & \cdots & z_{2N_x} \\ z_{31} & z_{32} & z_{33} & \cdots & z_{3N_x} \\ \vdots & \vdots & \vdots & \ddots & \vdots \\ z_{N_x1} & z_{N_x2} & z_{N_x3} & \cdots & z_{N_xN_x} \end{bmatrix}, \tag{5.3}$$

where the generic z_{ij} entry represents the reaction of the field generated with the j-th basis function (i.e., the source) into the i-th test function (i.e., the observation). However, since a space uniform sampling has been used, the space invariance of the Green's function yields to:

$$z_{ij} = z_{j-i} \quad \forall i, j \tag{5.4}$$

meaning that every reaction depends only on the mutual distance between the source and the observation point, but not on their exact positions. Therefore, the impedance matrix $\mathbf{Z}^{\text{rad}}$ can be written as:

$$\mathbf{Z}^{\text{rad}} = \begin{bmatrix} z_0 & z_{-1} & z_{-2} & \cdots & z_{2-N_x} & z_{1-N_x} \\ z_1 & z_0 & z_{-1} & \cdots & z_{3-N_x} & z_{2-N_x} \\ z_2 & z_1 & z_0 & \cdots & z_{4-N_x} & z_{3-N_x} \\ \vdots & \vdots & \vdots & \ddots & \vdots & \vdots \\ z_{N_x-2} & z_{N_x-3} & z_{N_x-4} & \cdots & z_0 & z_{-1} \\ z_{N_x-1} & z_{N_x-2} & z_{N_x-3} & \cdots & z_1 & z_0 \end{bmatrix}. \tag{5.5}$$

In the form expressed by (5.5), $\mathbf{Z}^{\text{rad}}$ is a Toeplitz matrix, i.e., a matrix where each descending diagonal from left to right is constant. Due to its symmetries, it can be sufficiently characterized by using only its first row and its first column. Therefore, instead of N_x^2, only $2N_x - 1$ elements have to be stored. The vector $\dot{\mathbf{z}}^{\text{rad}}$ sufficient to characterize the matrix can be written as:

$$\dot{\mathbf{z}}^{\text{rad}} = \begin{bmatrix} z_{N_x-1} & z_{N_x-2} & \cdots & z_1 & z_0 & z_{-1} & \cdots & z_{1-N_x} \end{bmatrix}^T \tag{5.6}$$

The impedance matrix associated with a linear and equispaced geometry can be completely characterized by the $2N_x - 1$ interactions stored in the vector $\dot{\mathbf{z}}^{\text{rad}}$. Let us now analyse the meaning of the of the entries of $\dot{\mathbf{z}}^{\text{rad}}$, and how these can be calculated. The entries $z_{-\ell}$, with $\ell > 0$ represent the interactions between an element with a source located ℓ bins on its right. Therefore these can be calculated by fixing the observation point on the first element and by changing the source point from 2 to N_x.

On the contrary, the entries z_ℓ, with $\ell > 0$ represent the interactions between an element with a source located ℓ bins on its left. To this purpose, it is convenient to cyclically extend the geometry, as shown in Fig. 5.3b, by adding N_x "virtual" elements mirrored with respect to the original ones. So, the observation point can still be considered fixed on the first element, while the source point changes from $-N_x + 2$ to 0.

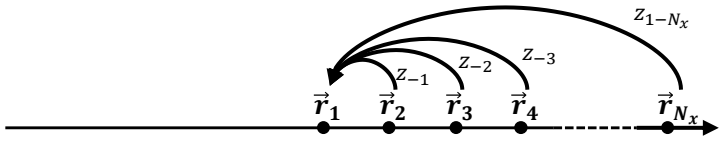

(a)

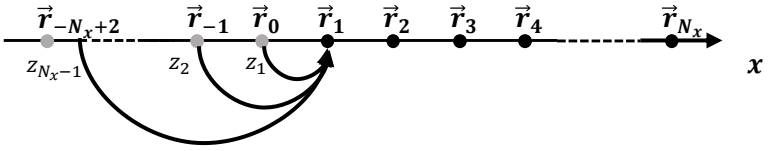

(b)

Figure 5.3: The mutual reaction between element 1 and element ℓ for (a) $\ell > 0$ and (b) $\ell < 0$

The entire $\dot{\mathbf{z}}^{\text{rad}}$ vector can then be calculated in the cyclically extended geometry by fixing the observation point on the element 1 and by changing the source point from $-N_x+2$ to N_x.

Assume now we want to calculate the matrix-vector product between $\mathbf{Z}^{\text{rad}}$ and the vector $\mathbf{p}$. The traditional matrix-vector product is expressed as:

$$\mathbf{b} = \mathbf{Z}^{\text{rad}} \cdot \mathbf{p} = \begin{bmatrix} z_0 & z_{-1} & \cdots & z_{1-N_x} \\ z_1 & z_0 & \cdots & z_{2-N_x} \\ \vdots & \vdots & \ddots & \vdots \\ z_{N_x-1} & z_{N_x-1} & \cdots & z_0 \end{bmatrix} \cdot \begin{bmatrix} p_1 \\ p_2 \\ \vdots \\ p_{N_x} \end{bmatrix} = \begin{bmatrix} z_0 \cdot p_1 + z_{-1} \cdot p_2 + \cdots + z_{1-N_x} \cdot p_{N_x} \\ z_1 \cdot p_1 + z_0 \cdot p_2 + \cdots + z_{2-N_x} \cdot p_{N_x} \\ \vdots \\ z_{N_x-1} \cdot p_1 + z_{N_x-2} \cdot p_2 + \cdots + z_0 \cdot p_{N_x} \end{bmatrix}. \tag{5.7}$$

However, the evaluation of (5.7) requires the storage of N_x^2 coefficients. By resorting to the properties of Toeplitz matrices, it is possible to calculate $\mathbf{Z}^{\text{rad}} \cdot \mathbf{p}$ by encompassing the storage of the entire matrix.

The first row of $\mathbf{b}$ in (5.7), is the sum of the element-by-element products between all the elements of $\mathbf{p}$ and the N_x-th to last elements of $\dot{\mathbf{z}}^{\text{rad}}$. The calculation of this row can be represented as follows:

$$\begin{array}{cccccccc} z_{N_x-1} & z_{N_x-2} & \cdots & z_1 & z_0 & z_{-1} & \cdots & z_{1-N_x} \\ & & & & p_1 & p_2 & \cdots & p_{N_x} \end{array}$$

Analogously, the second row can be calculated as follows:

$$\begin{array}{cccccccc} z_{N_x-1} & z_{N_x-2} & \cdots & z_1 & z_0 & z_{-1} & \cdots & z_{2-N_x} \quad z_{1-N_x} \\ & & & p_1 & p_2 & p_3 & \cdots & p_{N_x} \end{array}$$

Therefore, as it can be seen from the previous steps, the product can be implemented by using a backward-sliding window that selects the desired N_x elements of $\dot{\mathbf{z}}^{\text{rad}}$, multiplies them element-by-element by the elements of $\mathbf{p}$, and then sums the products. The complexity is N_x^2 (i.e., the same as the traditional approach), but the memory requirement is $2N_x - 1$, instead of N_x^2. This procedure is equivalent to computing the circular convolution[1], indicated as '$*$', between $\dot{\mathbf{z}}^{\text{rad}}$and the vector flip$(\mathbf{p})$, i.e., the vector taken in the reversed order.

[1]The circular convolution between two sequences is the convolution between two sequences periodically extended with period T. As one of the two sequences shifts on the other, the samples exceeding the fundamental period T re-enter in the convolution from the side opposite to the exit.

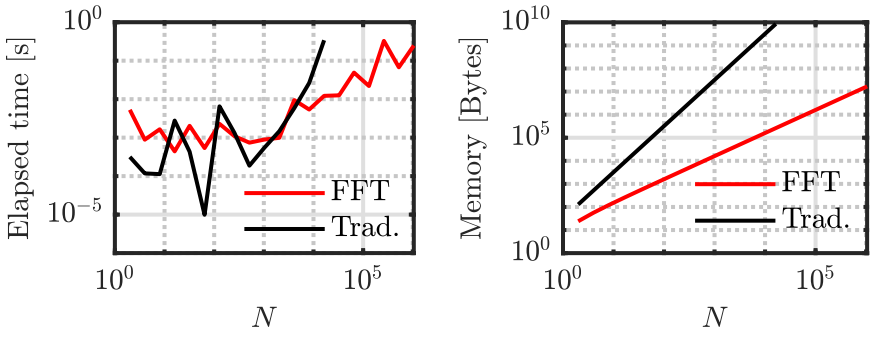

(a) (b)

Figure 5.4: (a) Toeplitz matrix-vector product elapsed time of the “traditionally" calculated product and the FFT calculated one, and (b) Memory requirements for the two approaches.

Therefore, $\mathbf{b}$ can be expressed as follows:

$$\mathbf{b} = \left[\dot{\mathbf{z}}^{\text{rad}} * \text{flip}\left(\mathbf{p}\right)\right]_{1:N_x}, \tag{5.8}$$

where the subscript $1:N_x$ indicates the first N_x components extracted from the convolution. The circular convolution used to calculate the Toeplitz matrix-vector product can be equivalently calculated with the aim of the Discrete Fourier Transform (DFT), which can be written as

$$\mathbf{b} = \text{DFT}^{-1}\left\{\text{DFT}\left\{\dot{\mathbf{z}}^{\text{rad}}\right\} \circ \text{DFT}\left\{\mathbf{p}\right\}\right\} \tag{5.9}$$

where $\circ$ denotes the Hadamard product. If the DFT and the IDFT are calculated with the FFT (Fast Fourier Transform) and the IFFT (Inverse Fast Fourier Transform)[2], (5.9) becomes:

$$\mathbf{b} = \text{FFT}^{-1}\left\{\text{FFT}\left\{\dot{\mathbf{z}}^{\text{rad}}\right\} \circ \text{FFT}\left\{\mathbf{p}\right\}\right\}. \tag{5.10}$$

In (5.10) two FFTs and an IFFT all are with complexity $\mathcal{O}\left(N_x \log_2 N_x\right)$ and the Hadamard product is with complexity $\mathcal{O}\left(N_x\right)$, therefore the overall complexity of the product computed with the FFT is $\mathcal{O}\left(N_x \log_2 N_x\right)$ versus the $\mathcal{O}\left(N_x^2\right)$ complexity of the traditionally calculated product. Moreover, only $2N_x - 1$ coefficients need to be stored.

Fig. 5.4a shows the elapsed time necessary to calculate a Toeplitz matrix-vector product versus the number of elements N. The fluctuations present in the plot are due to the other processes running in the background during the computation, and to the specific memory management of the system. As it can be seen for small values of N, the “traditional" product is more efficient due to the overhead operations necessary to calculate the FFT. However, the elapsed times of the two approaches grow in significantly different manners, the product calculated with the FFT . While curve associated with the “traditional" product grows fast before stopping for $N = 2^{13}$ due to the limited memory resources. Fig. 5.4b shows the memory requirements necessary to calculate the Toeplitz matrix-vector product calculated with the two algorithms. The data is stored in double-precision.

Two Dimensional Case

Let us now consider the planar geometry shown in Fig. 5.5, where N_x and N_y elements are uniformly arranged along x-axis and y-axis respectively. The element numbering is carried out along x before shifting to the following y-coordinate row in the chosen geometry. The impedance matrix $\mathbf{Z}$ can be expressed as:

$$\mathbf{Z}^{\text{rad}} = \begin{bmatrix} \mathbf{Z}_0 & \mathbf{Z}_{-1} & \mathbf{Z}_{-2} & \dots & \mathbf{Z}_{1-N_y} \\ \mathbf{Z}_1 & \mathbf{Z}_0 & \mathbf{Z}_{-1} & \dots & \mathbf{Z}_{2-N_y} \\ \mathbf{Z}_2 & \mathbf{Z}_1 & \mathbf{Z}_0 & \dots & \mathbf{Z}_{3-N_y} \\ \vdots & \vdots & \vdots & \ddots & \vdots \\ \mathbf{Z}_{N_y-1} & \mathbf{Z}_{N_y-2} & \mathbf{Z}_{N_y-3} & \dots & \mathbf{Z}_0 \end{bmatrix}. \tag{5.11}$$

[2]The DFT is the mathematical transform, while the FFT and the IFFT are the specific algorithms use for the computation.

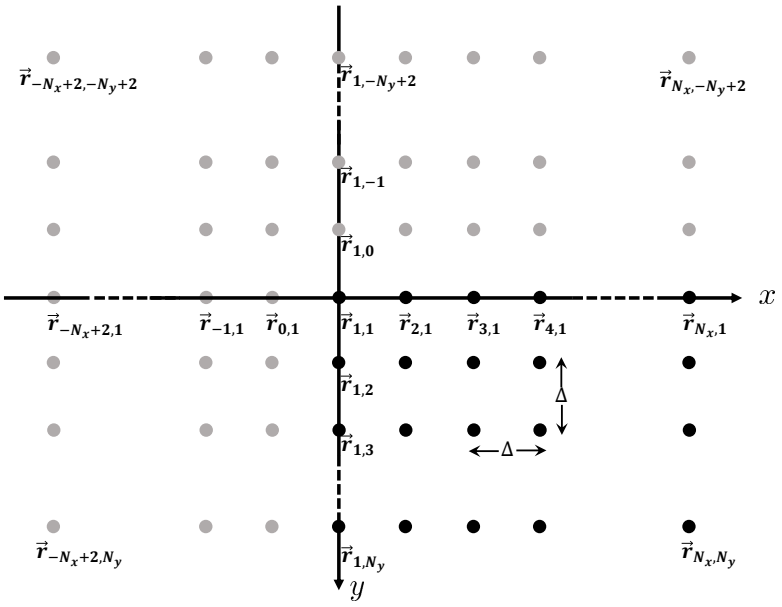

Figure 5.5: Planar geometry of N_x equispaced elements along x-axis and N_y equispaced elements along y-axis (black). The number ordering is along x. The cyclically extended geometry is also shown (grey).

The matrix $\mathbf{Z}^{\text{rad}}$ is a block Toeplitz matrix, i.e., a matrix that can be subdivided into blocks arranged in a Toeplitz fashion, where each of the blocks is a Toeplitz matrix itself. Each block represents the interactions within the same y coordinate. Therefore the subscript of each block indicates the difference in y between the source and the observation point. Any block $\mathbf{Z}_k$ of (5.11) is expressed as follows:

$$\mathbf{Z}_k = \begin{bmatrix} z_{0,k} & z_{-1,k} & z_{-2,k} & \cdots & z_{2-N_x,k} & z_{1-N_x,k} \\ z_{1,k} & z_{0,k} & z_{-1,k} & \cdots & z_{3-N_x,k} & z_{2-N_x,k} \\ z_{1,k} & z_{1,k} & z_{0,k} & \cdots & z_{4-N_x,k} & z_{3-N_x,k} \\ \vdots & \vdots & \vdots & \ddots & \vdots & \vdots \\ z_{N_x-1,k} & z_{N_x-2,k} & z_{N_x-3,k} & \cdots & z_{1,k} & z_{0,k} \end{bmatrix} \tag{5.12}$$

where the entry $z_{i,j}$ of $\mathbf{Z}^{\text{rad}}$ is the interaction between the source located in $\left(i_{\text{obs}}+i,\, j_{\text{obs}}+j\right)$ an the observation point located in $\left(i_{\text{obs}},\, j_{\text{obs}}\right)$. The impedance matrix is fully characterized if the first column and the first row of blocks (i.e., $2N_y-1$ blocks) are characterized, and each block is in turn characterized if its first column and its first row are known, i.e., $2N_x-1$ elements per block to determine. As it has been done in the previous one dimensional case, to ease the computation, it is convenient to extend the geometry cyclically (gray dots) to form a $(2N_x-1)\times\left(2N_y-1\right)$ uniform grid, as shown in Fig. 5.5.

Analogously to what has been previously done in the one dimensional case, it is also possible to define the matrix $\mathbf{z}$ containing all the interactions, and defined as follows:

$$\ddot{\mathbf{z}}^{\text{rad}} = \begin{bmatrix} z_{N_x-1,N_y-1} & \cdots & z_{0,N_y-1} & \cdots & z_{1-N_x,N_y-1} \\ z_{N_x-1,N_y-1} & \cdots & z_{0,N_y-1} & \cdots & z_{1-N_x,N_y-1} \\ \vdots & \ddots & \vdots & \ddots & \vdots \\ z_{N_x-1,1} & \cdots & z_{0,1} & \cdots & z_{1-N_x,1} \\ z_{N_x-1,0} & \cdots & z_{0,0} & \cdots & z_{1-N_x,0} \\ z_{N_x-1,-1} & \cdots & z_{0,-1} & \cdots & z_{1-N_x,-1} \\ \vdots & \ddots & \vdots & \ddots & \vdots \\ z_{N_x-1,1-N_y1} & \cdots & z_{0,1-N_y} & \cdots & z_{1-N_x,1-N_y} \end{bmatrix}. \tag{5.13}$$

The matrix is filled in by fixing the observation point on $(0,0)$ and by scanning over the positions $\left(i,j\right)$ with $i=-N_x+1,\ldots,N_x-1$, and $j=-N_y+1,\ldots,N_y-1$.

Now one can write the matrix-vector product for the two dimensional case as follows

$$\mathbf{b} = \mathbf{Z}^{\text{rad}} \cdot \mathbf{p} = \mathbf{Z}^{\text{rad}} \cdot \begin{bmatrix} p_1 \\ p_2 \\ \vdots \\ p_{N_x \cdot N_y} \end{bmatrix}. \tag{5.14}$$

Similarly to the previous case, the product is equivalent to calculate the first $N_x \times N_y$ elements of the circular 2D convolution between $\ddot{\mathbf{z}}^{\text{rad}}$ and $\tilde{\mathbf{P}}$ flipped, which is written as follows

$$\mathbf{b} = \text{reshape}\left\{\ddot{\mathbf{z}}^{\text{rad}} * \text{flip}\left(\tilde{\mathbf{P}}\right)\right\}_{1:N_x \cdot N_y} \tag{5.15}$$

where $\tilde{\mathbf{P}}$ is $\mathbf{p}$ reshaped into rows and defined as

$$\tilde{\mathbf{P}} = \begin{bmatrix} p_{1,1} & p_{2,1} & \cdots & p_{N_x,1} \\ p_{1,2} & p_{2,2} & \cdots & p_{N_x,2} \\ \vdots & \vdots & \ddots & \vdots \\ p_{1,N_y} & p_{2,N_y} & \cdots & p_{N_x,N_y} \end{bmatrix}. \tag{5.16}$$

with

$$p_{i,j} = p_{(j-1)\cdot N_x + i} \tag{5.17}$$

And the flipping operator reverses both the rows and the columns by rotating the matrix by 180°, which is defined as

$$\text{flip}\left(\tilde{\mathbf{P}}\right) = \text{flip}\left(\begin{bmatrix} p_{1,1} & p_{2,1} & \cdots & p_{N_x,1} \\ p_{1,2} & p_{2,2} & \cdots & p_{N_x,2} \\ \vdots & \vdots & \ddots & \vdots \\ p_{1,N_y} & p_{2,N_y} & \cdots & p_{N_x,N_y} \end{bmatrix}\right) = \begin{bmatrix} p_{N_x,N_y} & p_{N_x-1,N_y} & \cdots & p_{1,N_y} \\ p_{N_x,N_y-1} & p_{N_x-1,N_y-1} & \cdots & p_{1,N_y-1} \\ \vdots & \vdots & \ddots & \vdots \\ p_{N_x,1} & p_{N_x-1,1} & \cdots & p_{1,1} \end{bmatrix} \tag{5.18}$$

Three Dimensional Case

Extending to the three dimensional case, a 3D tensor $\dddot{\mathbf{z}}^{\text{rad}}$ is sufficient to characterize the interactions in the $\mathbf{Z}^{\text{rad}}$, where the entries of the tensor $\dddot{\mathbf{z}}^{\text{rad}}(i,j,k)$ stands for the interaction between the source point at $(N_x - i, N_y - j, N_z - k)$ and the observation point at $(0,0,0)$ with $i = 1,\ldots,2N_x - 1,\ j = 1,\ldots,2N_y - 1$ and $k = 1,\ldots,2N_z - 1$.

Then the product is calculated by using a circular 3D convolution as

$$\mathbf{b} = \mathbf{Z}^{\text{rad}} \cdot \mathbf{p} = \text{reshape}\left\{\dddot{\mathbf{z}}^{\text{rad}} * \text{flip}\left(\tilde{\mathbf{P}}\right)\right\}_{1:N_x \cdot N_y \cdot N_z} \tag{5.19}$$

where

$$\tilde{\mathbf{P}}(i,j,k) = p_{(k-1)\cdot N_x \cdot N_y + (j-1)\cdot N_x + i} \tag{5.20}$$

and

$$\text{flip}\left(\tilde{\mathbf{P}}\right)(i,j,k) = \tilde{\mathbf{P}}\left(N_x - i, N_y - j, N_z - k\right) \tag{5.21}$$

CGFFT Formulation

After having illustrated the properties of the Toeplitz matrices, it is possible to apply these properties to reduce the CG method's memory requirements and computation time.

The residual vector (5.2) can be expressed as follows:

$$\mathbf{r}^{(k)} = \mathbf{v} - \underbrace{\mathbf{z}^{\text{mat}} \circ \mathbf{i}^{(k)}}_{①} - \underbrace{\mathbf{Z}^{\text{rad}} \cdot \mathbf{i}^{(k)}}_{②}, \tag{5.22}$$

where the product ① is calculated as the element-wise product between the currents $\mathbf{i}^{(k)}$ and $\mathbf{z}^{\text{mat}}$, the diagonal entries of $\mathbf{Z}^{\text{mat}}$, and the product ② can be calculated by using the FFT. The structure of the entire impedance matrix $\mathbf{Z}^{\text{rad}}$ in a configuration including three polarizations can be explicated as follows:

$$\mathbf{Z}^{\text{rad}} = \begin{bmatrix} \mathbf{Z}_{xx} & \mathbf{Z}_{xy} & \mathbf{Z}_{xz} \\ \mathbf{Z}_{yx} & \mathbf{Z}_{yy} & \mathbf{Z}_{yz} \\ \mathbf{Z}_{zx} & \mathbf{Z}_{zy} & \mathbf{Z}_{zz} \end{bmatrix} \tag{5.23}$$

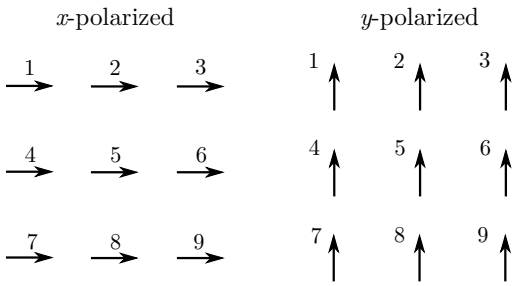

Figure 5.6: Diagram of x-polarized sources and y-polarized sources

where each sub-matrix $\mathbf{Z}_{\ell m}$ is the impedance matrix calculated as in (2.22) between ℓ-polarized and m-polarized currents, it results in a Toeplitz-like form, and is characterized by the interactions stored in $\mathbf{z}_{\ell m}$. However, if the same number of points are taken in the x, y, and z, due to reciprocity and to the symmetries of the structure, the sub-matrices circled in red are sufficient for its characterization. Therefore it is simply sufficient to calculate the interactions $\mathbf{z}_{xx}$, and $\mathbf{z}_{xy}$. However, the sub-matrices are not identical, in the elements ordering, to the calculated ones, and an extra operation is necessary to build the entire matrix correctly. Let us consider, for instance, the geometry sketched below, where the x- and y-polarized currents are present.

The interactions between the x-polarized currents are numerically equal to the ones between the y-polarized ones. However, a different element ordering has to be considered. For instance, as shown in Fig. 5.6, the interaction between the x-polarized currents 1 and 2 is different from the interaction between the y-polarized currents 1 and 2. Instead, the former is equal to the interaction between the y-polarized currents 1 and 4. Therefore, it is possible to calculate $\mathbf{z}_{xx}$ only, but an element rotation is needed to derive $\mathbf{z}_{yy}$ or $\mathbf{z}_{zz}$ out of it. Moreover, if the basis functions are cubic, as used in this tool, the magnitudse of the mutual reactions for the same absolute distance are the same, yielding $\|z_i\| = |z_{-i}\|$, with only a sign different depending on the relative directions along the three axes. This feature simplifies the calculation and storage of the interactions by a factor 8 from $(2N_x-1)\cdot\left(2N_y-1\right)\cdot(2N_z-1)$ to $N_x\cdot N_y\cdot N_z$. Then the matrix-vector product can be calculated as follows:

$$\begin{aligned}
\mathbf{Z}^{\text{rad}}\cdot\mathbf{i}^{(k)} &= \begin{bmatrix}\mathbf{Z}_{xx} & \mathbf{Z}_{xy} & \mathbf{Z}_{xz}\\ \mathbf{Z}_{yx} & \mathbf{Z}_{yy} & \mathbf{Z}_{yz}\\ \mathbf{Z}_{zx} & \mathbf{Z}_{zy} & \mathbf{Z}_{zz}\end{bmatrix}\cdot\begin{bmatrix}\mathbf{i}_x^{(k)}\\ \mathbf{i}_y^{(k)}\\ \mathbf{i}_z^{(k)}\end{bmatrix} = \\
&= \begin{bmatrix}\mathbf{Z}_{xx}\cdot\mathbf{i}_x^{(k)}+\mathbf{Z}_{xy}\cdot\mathbf{i}_y^{(k)}+\mathbf{Z}_{xz}\cdot\mathbf{i}_z^{(k)}\\ \mathbf{Z}_{yx}\cdot\mathbf{i}_x^{(k)}+\mathbf{Z}_{yy}\cdot\mathbf{i}_y^{(k)}+\mathbf{Z}_{yz}\cdot\mathbf{i}_z^{(k)}\\ \mathbf{Z}_{zx}\cdot\mathbf{i}_x^{(k)}+\mathbf{Z}_{zy}\cdot\mathbf{i}_y^{(k)}+\mathbf{Z}_{zz}\cdot\mathbf{i}_z^{(k)}\end{bmatrix} = \\
&= \begin{bmatrix}\mathbf{Z}_{xx}\\ \mathbf{Z}_{yx}\\ \mathbf{Z}_{zx}\end{bmatrix}\cdot\mathbf{i}_x^{(k)}+\begin{bmatrix}\mathbf{Z}_{xy}\\ \mathbf{Z}_{yy}\\ \mathbf{Z}_{zy}\end{bmatrix}\cdot\mathbf{i}_y^{(k)}+\begin{bmatrix}\mathbf{Z}_{xz}\\ \mathbf{Z}_{yz}\\ \mathbf{Z}_{zz}\end{bmatrix}\cdot\mathbf{i}_z^{(k)},
\end{aligned} \tag{5.24}$$

where products $\mathbf{Z}_{\ell m}\cdot\mathbf{i}_m^{(k)}$ can be efficiently calculated by using the FFT, as shown in previously. The number of operations can be reduced by pre-computing the FFT of the blocks $\mathbf{z}_{\ell m}$ before entering the CG algorithm. Moreover, inside the residual evaluation, for every CG step, the FFT calculation of each $\mathbf{i}_{x,y,z}^{(k)}$ can be calculated only once and used for the all the three necessary products, as highlighted in (5.24).

Table 5.1: Linear system solution comparison between CG-FFT, Inversion and LU-factorization

	Complexity	Memory
Inversion	$\mathcal{O}\left(N^3\right)$	N_t^2
LU Factorization	$\mathcal{O}\left(\frac{2}{3}N_t^3\right)+\mathcal{O}\left(N_t^2\right)$	N_t^2
CG	$n_s\mathcal{O}\left(N_t^2\right)+ns_{\mathcal{O}}\left(N_t\right)$	N_t^2
CG-FFT	$n_s\mathcal{O}\left(N_t\log_2 N\right)+n_s\mathcal{O}\left(N_t\right)$	N_t

In summary, due to the Toeplitz properties and the choice of cubic basis functions, the number of integrals to be evaluated can be reduced from $\left(3N_xN_yN_z\right)^2$ to $\left(2N_xN_yN_z\right)$. The memory storage is drops from N_t^2

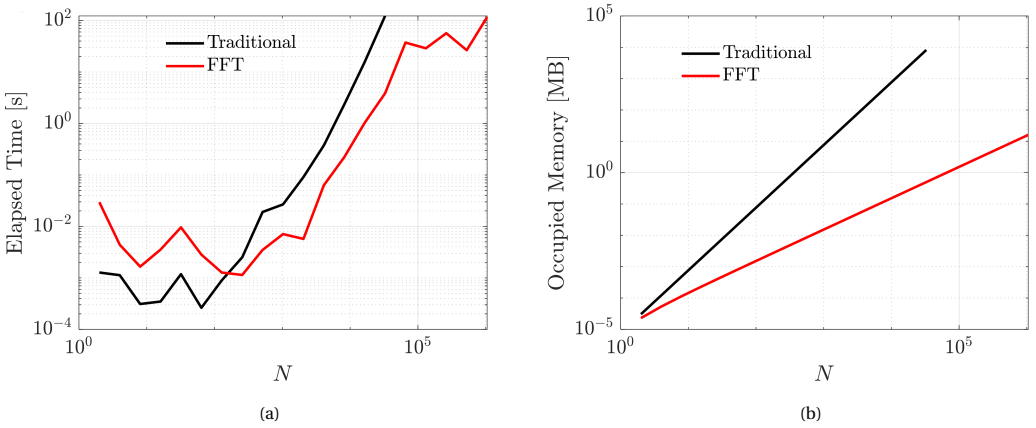

Figure 5.7: The comparison of performance between the traditional LU factorization method and CG-FFT in terms of (a) elapsed time and (b) memory storage

to N_t and the calculation of the matrix-vector product has a complexity of $\mathcal{O}\left(N_t \log_2 N_t\right)$ instead of $\mathcal{O}\left(N_t^2\right)$. The comparison between different method is shown in Table. 5.1.2 and Fig. 5.7. It is seen that the CG-FFT approach has advantage over the other methods in terms of computation complexity or memory requirement, where the traditional method fails when the number of basis function exceeds 40×10^3 due to memory limits while the CG-FFT method can handle several millions of unknowns with faster solutions.

5.1.3. Masking

Since the grid is chosen to contain all the bodies to simulate, and to represent the field accurately, it is likely that some mesh cells do not contain any material piece, and are not active during the calculation. Ideally one only needs to solve a reduced linear system

$$\hat{\mathbf{v}} = \left(\hat{\mathbf{Z}}^{\text{mat}} + \hat{\mathbf{Z}}^{\text{rad}}\right)\hat{\mathbf{i}} \tag{5.25}$$

where $\hat{\mathbf{v}}$, $\hat{\mathbf{Z}}^{\text{mat}}$, $\hat{\mathbf{Z}}^{\text{rad}}$ and $\hat{\mathbf{i}}$ are the correspondent of $\mathbf{v}$, $\mathbf{Z}^{\text{mat}}$, $\mathbf{Z}^{\text{rad}}$, and $\mathbf{i}$, but defined only on the scatterer. However, after the introduction of FFT, the cubic geometry has to be maintained to preserve the Toeplitz structure and the convolutional property of $\hat{\mathbf{Z}}^{\text{rad}}$. A masking procedure is used to discard in the CG-FFT the contributions from the mesh cells not containing any material piece. Suppose K out of N_t basis functions are used in one simulation. Let the total grid $\mathscr{D}$ containing N_t points be numbered as

$$\mathscr{D} = \{1, 2, 3, \ldots, N_t\} \tag{5.26}$$

and the actual grid $\mathscr{D}_s$ containing K points be numbered as

$$\mathscr{D} = \{k_1, k_2, \ldots, k_K\} \tag{5.27}$$

where k_i is the index of the i_{th} basis function in the whole grid. For example, k_1 means the index of the first basis function that contains a material piece. The mask matrix $\mathbf{M}$ of size $N_t \times K$ maps $\mathscr{D}$ into $\mathscr{D}_s$ and vice versa, by creating a correspondence between the two different numbering sets, the element of which is defined as

$$m_{ij} = \begin{cases} 1, & \text{if } i = k_j \\ 0 & \text{otherwise.} \end{cases} \tag{5.28}$$

In such a way, the mapping between the entire basis function set and relevant basis function set can easily performed by

$$\hat{\mathbf{i}} = \mathbf{M} \cdot \mathbf{i} \tag{5.29}$$

$$\mathbf{i} = \mathbf{M}^{\mathbf{T}} \cdot \hat{\mathbf{i}}. \tag{5.30}$$

Fig. 5.8 shows the updated algorithm for the CGFFT approach, the irrelevant basis functions are taken out at the end of each step and refilled with zeros before the next iteration. In such a way one is still able to compute the matrix-vector product disregarding the contributions from irrelevant basis functions.

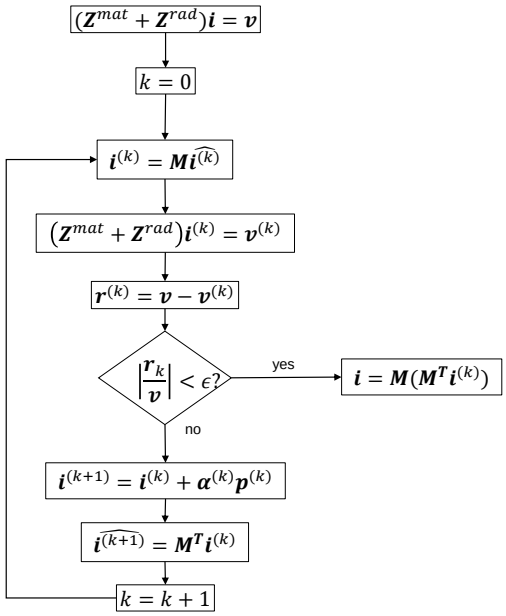

Figure 5.8: Flow chart diagram of CG algorithm for solving the linear system

5.2. Post-Processing

Once the linear system has been solved, scattering and discrete port problems are considered for post-processing.

5.2.1. Scattering Problems

For scattering problems, by using (2.23), the equivalent current are obtained for desired results.The most direct result is the radiation in far fields using homogenous space Green's function

$$\vec{E}^s(\vec{r}) = \iiint_{\mathcal{V}} \bar{\bar{G}}^{\text{hs}}(\vec{r},\vec{r}\,') \cdot \vec{J}_{\text{eq}}(\vec{r}\,')d\vec{r}\,'. \tag{5.31}$$

Let us now assume that the observation point $\vec{r}$ is located in the far field. Therefore, the dimension of each cuboid constituting the source can be considered small with respect to the distance from the observation point. The electric field radiated by the n-th current can written as

$$\vec{E}(\vec{r}) = \iiint_{\mathcal{V}_n} \bar{\bar{G}}^{\text{hs}}(\vec{r},\vec{r}\,') \cdot \vec{J}_{\text{eq}}(\vec{r}\,')\, d\vec{r}\,' = \bar{\bar{G}}^{\text{hs}}(\vec{r},\vec{r}_n) \cdot \vec{J}_{\text{eq}}(\vec{r}_n)\,\Delta^3. \tag{5.32}$$

By applying the superposition principle, the total field can be written as

$$\vec{E}^{\text{far}}(\vec{r}) = \Delta^3 \sum_{n=0}^{N_t} \bar{\bar{G}}^{\text{hs}}(\vec{r},\vec{r}\,')\, i_n \vec{b}_n \tag{5.33}$$

where i_n is the n-th element of the solution $\mathbf{i}$ and $\vec{b}_n$ is the n-th basis function. By using the cubic pulse basis functions, (5.2.1) becomes as follows

$$\vec{E}^{\text{far}}(\vec{r}) = \Delta \sum_{n=0}^{N_t} \bar{\bar{G}}^{\text{hs}}(\vec{r},\vec{r}\,') \cdot \hat{p}_n i_n \tag{5.34}$$

where $\hat{p}_n$ is the orientation of the n-th basis function.

The total electric field $\vec{E}$ inside the structure, according to (2.7), can be written as

$$\vec{E}(\vec{r}_n) = \frac{1}{\Delta^2 j\omega\epsilon_0 \left(\varepsilon_{\text{eff}}(\vec{r}_n) - \varepsilon_{\text{eff}}^{bg}(\vec{r}_n)\right)} \left(i_n\hat{x} + i_{n+N_x}\hat{y} + i_{n+2N_x}\hat{z}\right), \text{ with } n = 1,2,\ldots,N_s. \tag{5.35}$$

The power lost in the dielectric can be calculated in matrix form as

$$P_{\text{Loss}} = \frac{1}{2}\mathbf{i}^H \Re\left\{\mathbf{Z}^{\text{mat}}\right\}\mathbf{i} \tag{5.36}$$

which simply is equivalent to

$$P_{\text{Loss}} = \frac{1}{2}\sum_{n=0}^{N_t} \left|i_n^2\right| \Re\left\{\sigma_{\text{eff}}(\vec{r}_n)\right\} \tag{5.37}$$

The radiated power can be calculated from

$$P_{\text{Rad}} = \frac{1}{2}\Re\left\{\mathbf{i}^H \mathbf{Z}^{\text{rad}}\mathbf{i}\right\} \tag{5.38}$$

which follows the conservation of energy as

$$P_{\text{Rad}} = \Re\left\{\frac{1}{2}\mathbf{i}^H \cdot \mathbf{v}_{\text{in}} - P_{\text{Loss}}\right\} = \frac{1}{2}\sum_{n=0}^{N_t} \Re\left\{i_n v_n\right\} - P_{\text{Loss}}. \tag{5.39}$$

5.2.2. Discrete Port Problems

Finding the exact excitation of (2.23) is not straightforward for discrete port problems when there are source impedance Z_s connected to the ports. The excitation could be found by solving a equivalent circuit as shown in Figure, but the S parameters of the structure is required. Since the circuit parameters do not depend on the excitation but only the structure itself, one may use a testing case to solve the circuit parameters beforehand. Here the testing case is chosen to be all source impedances are zeros $Z_{sn} = 0$. Assume there are K ports oriented along $\hat{p}_1^{\text{ex}}, \hat{p}_2^{\text{ex}}, \ldots, \hat{p}_K^{\text{ex}}$ excited individually with a voltage $\mathbf{V} = [V_1, V_2, \ldots, V_K]^T$, now we can solve the equivalent currents $\tilde{\mathbf{i}}$. The average current flowing across the k-th port can be expressed

$$I_{\text{port,k}} = \frac{1}{d_k}\iiint_{\mathcal{V}_k} \vec{J}(\vec{r}_k)\cdot \hat{p}_k^{\text{ex}} d\vec{r}_k \tag{5.40}$$

where $\mathcal{V}_k$ is the volume enclosing the port k, d_k is the length of port k along the orientation $\hat{p}_k^{\text{ex}}$ and $\vec{J}(\vec{r})$ is the current on the basis function, which can be obtained through:

$$\vec{J}(\vec{r}) = \sigma(\vec{r})\,\vec{E}(\vec{r}) = \frac{\sigma(\vec{r})\,\vec{J}_{\text{eq}}(\vec{r})}{\sigma_{\text{eff}}(\vec{r})}. \tag{5.41}$$

One obtains the $I_{\text{port,k}}$ by

$$I_{\text{port,k}} = \sum_{m=1}^{N_k} \frac{\sigma\left(\vec{r}_{k(m)}\right)}{\sigma_{\text{eff}}\left(\vec{r}_{k(m)}\right)} \frac{\left(i_{k(m)}\hat{x} + i_{N+k(m)}\hat{y} + i_{2N+k(m)}\hat{z}\right)\cdot \hat{p}_k^{\text{ex}}}{d_k/\Delta} \tag{5.42}$$

where N_k is the number of basis functions used to describe port k, Δ is the size of the basis function, i_n is the n-th element of the solution $\tilde{\mathbf{i}}$ and $\vec{r}_{k(m)}$ is the position vectors that belong to the set R^k describing the volume $\mathcal{V}_k$.

$$\vec{r}_{k(m)} \in R^k = \left\{\vec{r} | \vec{r} \in \mathcal{V}_k\right\}. \tag{5.43}$$

The input admittance matrix $\mathbf{Y}^{\text{a}}$ for the antenna can be characterized by

$$\mathbf{Y}^{\text{a}}_{i,j} = \frac{I_{\text{port,i}}}{V_j} \tag{5.44}$$

where $I_{port,i}$ is the current flowing across port i when port j is excited by a voltage V_j. The input impedance matrix of the antenna is simply an inversion of $\mathbf{Y}^{\text{a}}$.

$$\mathbf{Z}^{\text{a}} = \left[\mathbf{Y}^{\text{a}}\right]^{-1}. \tag{5.45}$$

Therefore, the overall impedance matrix $\mathbf{Z}$ is obtained by

$$\mathbf{Z} = \mathbf{Z}^{\text{a}} + \mathbf{Z}^{s} \tag{5.46}$$

where $\mathbf{Z}^s$ is a diagonal matrix with source impedances as its elements

$$\mathbf{Z}^s = \begin{bmatrix} Z_{s1} & 0 & \cdots & 0 \\ 0 & Z_{s2} & \cdots & 0 \\ \vdots & 0 & \ddots & \vdots \\ 0 & \cdots & 0 & Z_{sK} \end{bmatrix}. \tag{5.47}$$

The current flowing across the ports can be derived as

$$\mathbf{I} = [\mathbf{Z}]^{-1}\mathbf{V}. \tag{5.48}$$

The true excitation falls on the ports is solved using

$$\mathbf{V}^{\text{ex}} = \mathbf{Z}^{\text{a}}\mathbf{I}. \tag{5.49}$$

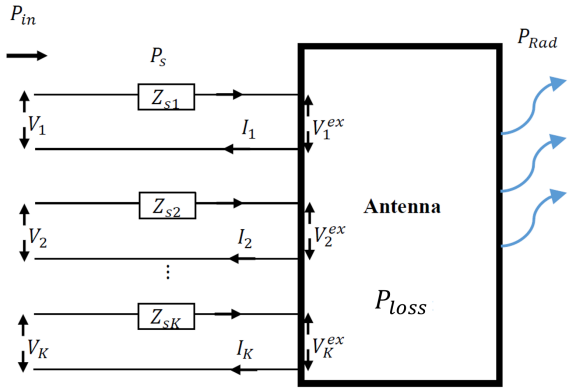

Figure 5.9: Equivalent circuit diagram of a discrete port problem

Then the true solution of the equivalent currents **i** are obtained by defining the excitation terms as Eq and solving the linear system. From Figure one finds the input power P_{in} as in

$$P_{\text{in}} = \frac{1}{2}\mathbf{I}^H\mathbf{V}. \tag{5.50}$$

The power distributed on the source impedances P_s is

$$P_s = \frac{1}{2}\mathbf{I}^H\mathbf{Z}^s\mathbf{I} = \frac{1}{2}\sum_{k=1}^{K}\left|I_k^2\right|Z_{sk} \tag{5.51}$$

where I_k is the k-th element in **I**. The power lost in the dielectric P_{Loss} and the radiated power is expressed the same as (5.2.1) and (5.38). Similarly, due the conservation of energy, the radiated power is

$$P_{\text{Rad}} = P_{\text{in}} - P_{\text{Loss}} - P_{\text{s}}. \tag{5.52}$$

The S-parameters can also be calculated accordingly with a default reference impedance of 50Ω.

6

Validation

In this chapter, results from the V-MoM are compared and validated using both analytical tools and commercial software. Sec. 6.1 validates the simulation results of a dielectric sphere from the tool with Mie series [20]. In Sec. 6.2, a small lens with a dipole feed is simulated and the result is compared with CST.

6.1. Validation with the Mie Series - Dielectric Sphere

The Mie series gives an analytical solution for the fields scattered by a sphere by expanding the fields into spherical waves, and enforcing the boundary conditions on the surfaces. Let us assume a sphere of radius $\lambda_0/2$ with an effective permittivity of ε_r is illuminated by a plane wave impinging from the negative z-direction, with electric field along $\hat{x}$. The scattered field along the z-axis of the sphere is obtained from the V-MoM, the Mie series [21] and CST [22], as shown in Fig. 6.1.

The magnitude of the total field along the z-axis shown in Fig. 6.3 for $\varepsilon_r = 4$ and $\varepsilon_r = 8$, where different solutions are compared. The V-MoM meshes the volume into $81 \times 81 \times 81$ samples with $\Delta = \lambda_0/81$. The frequency domain solver is used in CST due to he resonant nature of the problem.

The voxel discretization of the V-MoM cannot represent perfectly the curvature of the sphere and its correct volume. As shown in Fig. 6.2a, the field in the structure is represented until $r - \Delta/2$, and this leaves an uncertainty for the outer $\Delta/2$ area, which usually can be ignored if the field is constant at the edges. For this reason, the V-MoM is compared with a dielectric sphere of the correct radius $r = \lambda_0/2$, and of $r - \Delta/2$ to model uncertainty due to the discretization, as depicted in Fig. 6.2b. As shown in Fig. 6.3, the V-MoM represents the field with an error comparable with the tolerance given by the discretization, making thus the code validated.

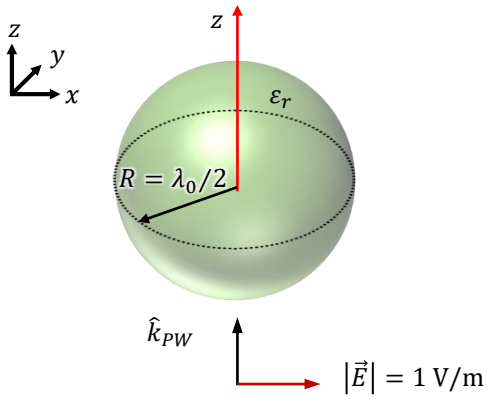

Figure 6.1: Graphical representation of a λ_0 sphere illuminated by a plane wave with field oriented along $\hat{x}$.

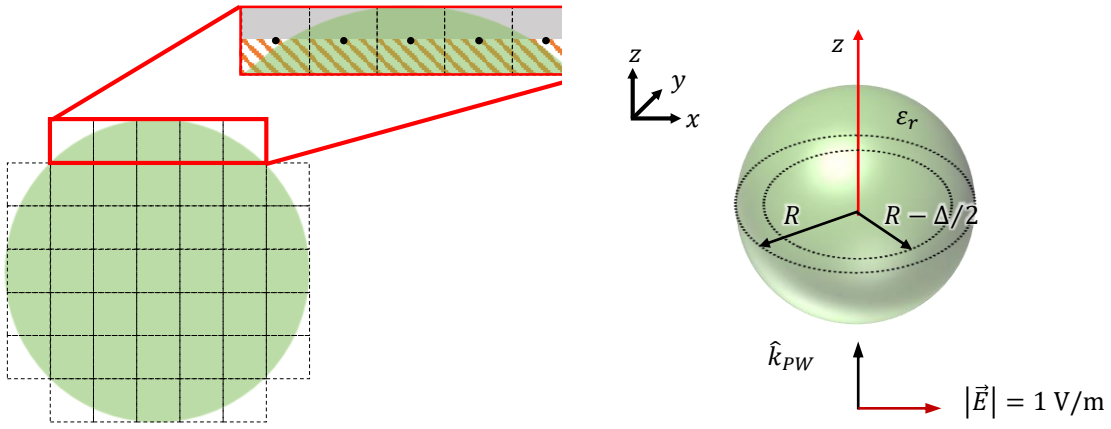

(a) (b)

Figure 6.2: (a) Representation of the fields by the basis functions on the edge. (b) Graphical representation of simulation on a smaller sphere of radius $\lambda_0/2 - \Delta/2$

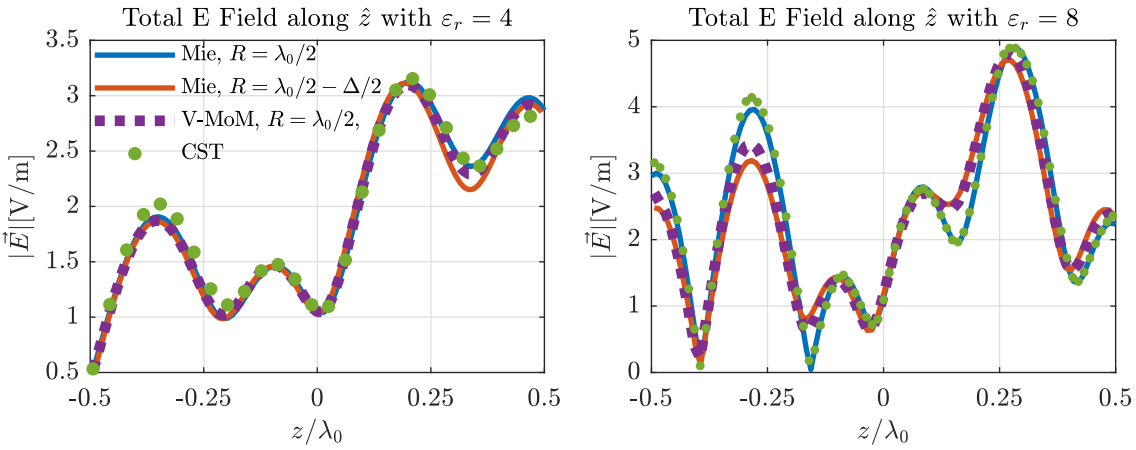

(a) (b)

Figure 6.3: The total electric field along $\hat{z}$ given by the V-MoM, CST and Mie series at the centre of the (a) $\varepsilon_r = 4$ sphere and (b) $\varepsilon_r = 8$ sphere

To compare the performances between the two numerical solvers, one defines the relative error as

$$\epsilon_{\text{solver}} = \left|\left| \frac{|\vec{E}^t_{\text{solver}}| - |\vec{E}^t_{\text{Mie}}|}{|\vec{E}^t_{\text{Mie}}|} \right|\right| \tag{6.1}$$

Table 6.1: Performance comparison between CST and the V-MoM for a $\varepsilon_r = 4$ sphere

	ϵ_{solver}	Computation Time
V-MoM	1.8%	109 s[1]
CST	4.1%	241 s

Table. 6.1 shows the comparison in terms of accuracy and computation time between the V-MoM and CST . It is seen that for the sphere with $\varepsilon_r = 4$, the V-MoM is more accurate than the CST by 2%. Meanwhile it is also faster than CST as it takes only 109 seconds to solve the linear system plus 53 seconds to compute the recyclable reaction integrals while CST takes 241 seconds to get a slightly less accurate results.

[1] t_{solver} = 109 s and the time to fill the reaction integrals is 53 s, which can be reused.

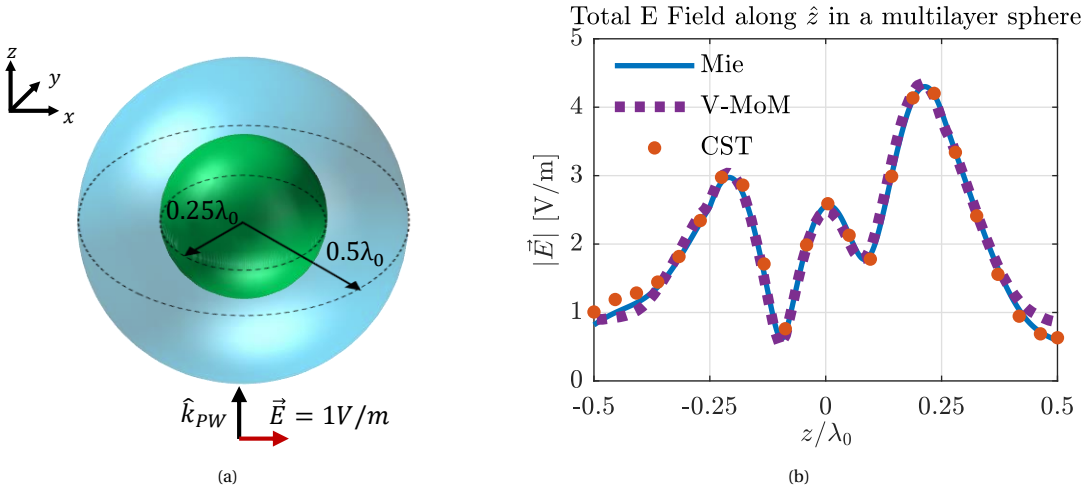

Figure 6.4: (a) Graphical representation of a multi-layer sphere with an inner $\varepsilon_r = 4$ sphere and an outer $\varepsilon_r = 8$ sphere. (b) Total field along $\hat{z}$ inside the multi-layer sphere obtained from the Mie series, V-MoM and CST

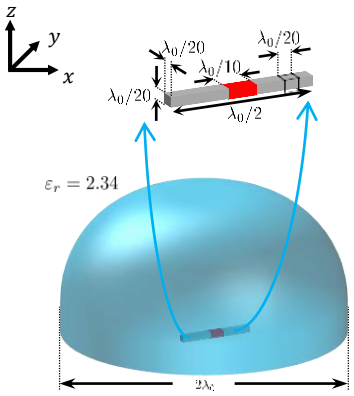

Figure 6.5: Graphical representation of a semi-hemispherical lens fed by a dipole antenna

The tool is also validated in the case of multilayered sphere under a plane wave incidence, as shown in Fig. 6.4a. The agreement Fig. 6.4b between different results demonstrates that the tool's capability of modelling inhomogeneous structures accurately, which is promising for realistic applications such as lens antennas with matching layers.

6.2. Validation with CST - Lens Antenna

The tool is validated for a practical case scenario consisting of the dipole fed lens antenna shown in Fig. 6.5. The lens has a dimension of $D = 2\lambda_0 = 2$mm and it is constituted of a dielectric material having a relative permittivity $\varepsilon_r = 2.34$. The fed is a half-wavelength dipole with a square section of $\lambda_0/20$ and a feeding gap of $\lambda_0/10$ long. This structure is discretized with basis functions having edge $\Delta = \lambda_0/20$, for a total of $1.92 \cdot 10^5$ unknowns.

First, the $2\lambda_0$ semi-hemispherical lens is constructed by a hemisphere with a diameter of $D = 2$mm and a cylinder of height $H = 0.195D$ located below, illuminated by a plane wave from broadside with electric field oriented along $\hat{x}$, as shown in Fig. 6.6a. Fig. 6.6b shows the magnitude of the total field inside the Lens along $\hat{z}$ direction at 294GHz, which is in good comparison between CST and the V-MoM. In Fig. 6.6c and Fig. 6.6d, the magnitude of the total electric field distribution are shown on the X-Z plane. It is seen that the V-MoM models the lens accurately in the near field with respect to CST.

Then the half-wavelength feeding dipole is simulated in free space with a volumetric excitation. Since this excitation can not be applied in CST, nine discrete ports are placed in parallel over the gap to represent the uniform excitation over the volumetric δ-gap space. Fig. 6.7a shows the comparison in terms of input

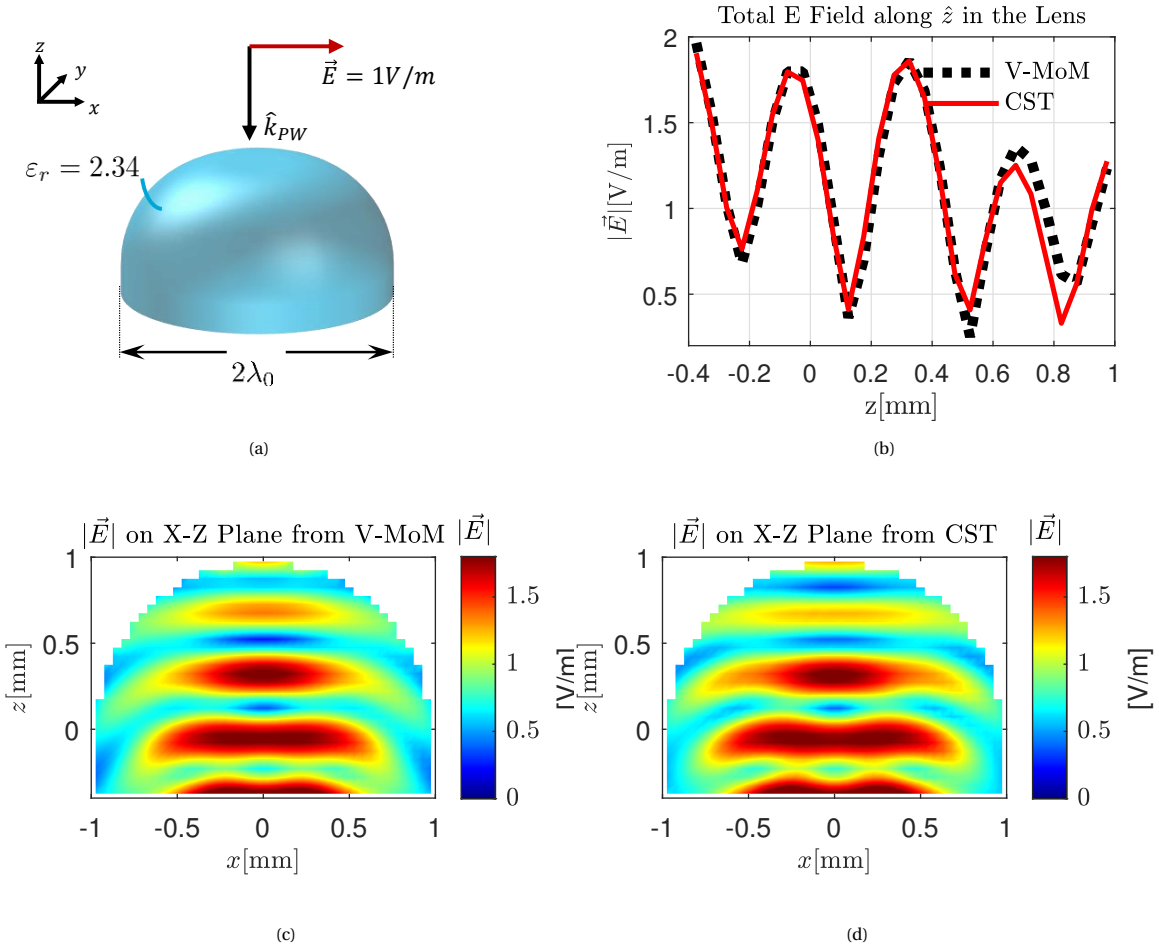

Figure 6.6: (a) A 2mm semi-hemispherical Lens with $\varepsilon_r = 2.34$ incident by a plane wave from $\hat{z}$. (b) The magnitude of the total electric field on the Lens along $\hat{z}$ given by CST and V-MoM at 294GHz. And the magnitude of the total field on the X-Z plane inside the lens given by (c) the V-MoM and (d) CST

impedance of the dipole between the V-MoM and CST. The disagreements are due to the different source representations between the V-MoM and CST, and are also due to the use of a single basis function on the dipole's cross section, which can not represent the current accurately. The sampling of $\lambda_0/20$ is sufficient for the dielectric while the metallization of the dipole requires much finer discretization. Nevertheless, the overall comparison acceptable over the entire frequency band and in the future we aim to decouple the simulation of the metallization and the dielectric by considering adding analytical corrections in the post-processing stage.

Finally, the dipole-lens antenna is simulated. In CST, the dipole is placed under the lens with its centre located at $(0,0,-h-\Delta/2)$. However, in the V-MoM, due to the even sampling of the grid and its resolution of $\Delta = \lambda_0/20$, the cylinder is constructed of height $\tilde{h} = 0.2D$ and the dipole is located at $\left(0,\Delta/2,-\tilde{h}-\Delta/2\right)$. The input impedance of the dipole-lens antenna is shown in Fig. 6.7b, proving the tool's capability to reproduce the field oscillations inside the lens, and showing a good agreement compared with CST. The radiated fields are shown in Fig. 6.8, when exciting the lens with a 4.5W power. The field evaluated on the X-Z cut inside the lens is shown in Fig. 6.8a, which results into a good agreement compared with CST in Fig. 6.8b. The far-fields are shown in Fig. 6.8c, evaluated at distance $r = 1$mm over $\varphi = 0$deg and $\varphi = 90$deg. From these simulations it is proved that the tool is able to simulate complex problems in transmission with a good accuracy.

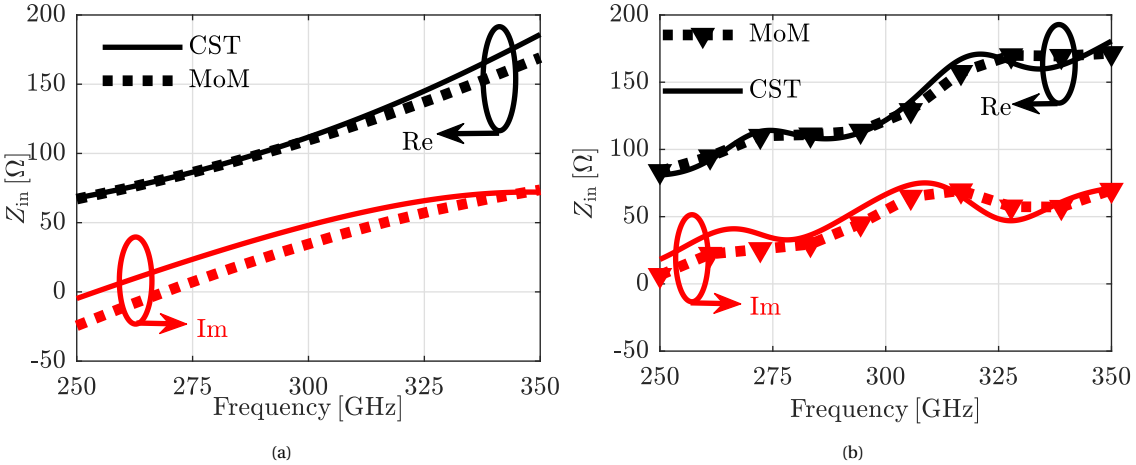

Figure 6.7: Input impedance for (a) the half-wavelength dipole and (b) the $2\lambda_0$ Lens antenna

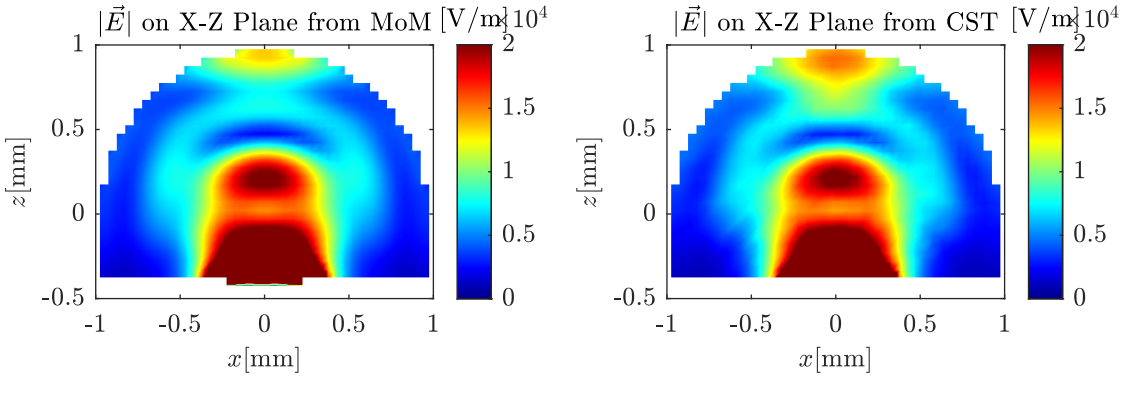

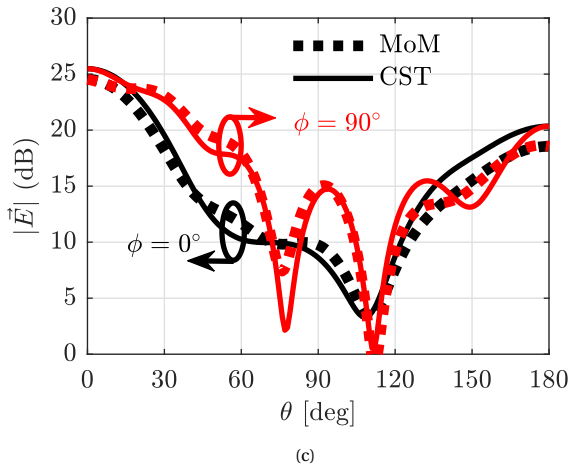

Figure 6.8: The total field inside the Lens antenna on the X-Z plane obtained at 294GHz from (a) V-MoM and (b) CST, and (c) the far field of the simulated antenna obtained from the V-MoM and CST

7

Radiometry

7.1. Motivation

Thermal noise contribution plays an important role in signal-to-noise estimation in communication systems, imaging systems, and earth observation tasks. With more and more devices in sub-terahertz being designed and used in such systems, the estimation of thermal noise becomes crucial, as it scales with the square of the frequency. If one integrates the noise spectrum from zero to the highest frequency, the total noise grows as f^3. For example, the thermal noise power at 1 THz is a billion times higher than the noise power at 1 GHz integrating the spectrum. However, there is a lack of analysis, both theoretical and experimental, on the thermal radiation from a realistic body, in the sub-THz band. Therefore, in this thesis, the V-MoM is used to estimate the noise power spectrum of an arbitrary shaped body with a certain conductivity and permittivity.

The thermal radiation from a body is typically characterized experimentally by comparing it with the one from black body radiation, with an additional correction parameter named emissivity $\mathscr{E}$. In 1860, Kirchhoff [23] first stated that if the body is in thermodynamic equilibrium, the emissivity of a body is equal to its absorptivity. Then the radiated power from a black body was estimated by Rayleigh–Jeans with classical physics, which then was validated incoherent with the experimental results at high frequencies, and thus bringing the ultraviolet catastrophe. Then in 1906, Planck [24] explained the experiment results well with the famous Planck's law, by introducing the quantum theory. However, an ideal black body does not exist, and to approximate the radiation from an actual body, emissivity as a correction parameter was created to calibrate the experimental results. The emissivity could be a wild function depending on the frequency, the shape and the material of the body.

In 1928, Johnson [25] analysed the noise caused by the thermal fluctuations of the electrons, after which his colleague Nyquist [26] presented a more rigorous formula, but also adding a quantum correction based on Planck's law without any experimental backing. This law is wildly used in microwave engineering known as the Johnson-Nyquist noise. The first semi-rigorous treatment of the power emitted by a material body kept at a certain temperature was proposed by Rytov [10] in 1955. At that time, the means to analyse complex electromagnetic problems was limited and thus Rytov suggested a simplified technique based on reciprocity and reflection and transmission from infinite slabs to approximate the absorptivity of the slabs. Since then heat transfer was studied in many work, [11], [27], and [12], using classical electromagnetic but most of them were done with ideal materials without experimental validation.

In this work the V-MoM is used to characterize the thermal emission from bodies having an arbitrary shape, and constituted by homogeneous materials, in the frequency range in which it is legitimate to define a conductivity. In fact, when the frequency is so high that in a box of tenth of a wavelength and there is only one electron, it is apparent that the concept of conductivity fails to represent homogenized properties of a body. Moreover, a waveguide problem is formulated and solved numerically to prepare for a validation with the experimental results of the radiation from a semiconductor.

7.2. Formulation using the V-MoM

To study the thermal radiation from a arbitrary body with relative permittivity ε_r and conductivity σ, kept at a certain temperature T, one discretizes it using N_t voxels of size Δ and sum the contribution in terms of

radiated power spectrum from each voxels respectively, which can be written as follows

$$P(f) = \sum_{n=1}^{N_t} \left| i_{\mathrm{n}}^{\mathrm{impr}} \right|^2 R_n^{\mathrm{rad}} \tag{7.1}$$

where R_n^{rad} is the radiation impedance of the n-th voxel in the body, and $i_{\mathrm{n}}^{\mathrm{impr}}$ is the impressed currents from Rytov [10] and is defined as

$$i_{\mathrm{n}}^{\mathrm{impr}} \equiv \sqrt{\frac{4hf}{e^{\frac{hf}{k_B T}} - 1} \Re\{\sigma_n\} \Delta}. \tag{7.2}$$

Since the Green's function in the presence of which the impressed currents are radiating is not known, the V-MoM procedure can be used to evaluated R^{rad}. The impressed currents are transferred into voltage sources, based on [25] and [26], and then the the radiated power spectrum of the body can be simulated numerically.

As shown in Fig. 4.6, the structure is discretized into N_s samples and $N_t = 3N_s$ basis function are used to represent the orthogonal three degrees of freedoms of the field. Then the linear system is obtained as (2.23), where

$$v_n = \sqrt{\frac{4hf}{e^{\frac{hf}{k_B T}} - 1} \Re\left\{\mathbf{z}_{\mathrm{n}}^{\mathrm{mat}}\right\}} e^{j\phi_n} \tag{7.3}$$

where $\Re\left\{\mathbf{z}_{\mathrm{n}}^{\mathrm{mat}}\right\}$ is the real part of diagonal elements in the material matrix $\mathbf{Z}^{\mathrm{mat}}$ and $\phi_n \in (0, 2\pi)$is the phase term, which is an random variable uniformly distributed in $[0, 2\pi]$, and an incoherent field excitation is obtained thanks to the statistical independence between all the different forcing terms.Each different set of phases represents a single realization in a Monte Carlo like simulation. Eventually, the average field and corresponding power is associated to an incoherent field excitation. At low frequencies, the denominator of (7.3) can be linearized, yielding

$$v_n = \sqrt{4k_B T \Re\left\{\mathbf{z}_{\mathrm{n}}^{\mathrm{mat}}\right\}} e^{j\phi_n}. \tag{7.4}$$

For all the small problems, where it is possible to store the matrix, and to calculate its inverse, (2.23) is directly solved by defining a MoM matrix $\mathbf{Y}^{\mathrm{MoM}}$ as the inverse of the sum of two matrices as

$$\mathbf{Y}^{\mathrm{MoM}} = \left(\mathbf{Z}^{\mathrm{mat}} + \mathbf{Z}^{\mathrm{rad}}\right)^{-1}. \tag{7.5}$$

Then (2.23) becomes as

$$\mathbf{i} = \mathbf{Y}^{\mathrm{MoM}} \mathbf{v}. \tag{7.6}$$

Combined with (5.38), the radiated power can be written as

$$P_{\mathrm{rad}} = \Re\left\{\mathbf{v}^{\mathrm{H}} \left(\mathbf{Y}^{\mathrm{MoM}}\right)^{\mathrm{H}} \mathbf{Z}^{\mathrm{rad}} \mathbf{Y}^{\mathrm{MoM}} \mathbf{v}\right\}. \tag{7.7}$$

7.2.1. Trace Computation

For incoherent excitations, the basis functions are excited one by one, and the results are then summed up to obtain the radiated power, meaning,

$$P_{\mathrm{rad}} = \Re\left\{\sum_{n=1}^{N_t} \mathbf{v}_{\mathrm{n}}^{\mathrm{H}} \left(\mathbf{Y}^{\mathrm{MoM}}\right)^{\mathrm{H}} \mathbf{Z}^{\mathrm{rad}} \mathbf{Y}^{\mathrm{MoM}} \mathbf{v}_{\mathrm{n}}\right\} \tag{7.8}$$

where $\mathbf{v}_{\mathrm{n}}$ is the excitation vector for the n-th simulation and is defined as

$$\mathbf{v}_{\mathrm{n}}(m) = \begin{cases} \sqrt{4k_B T \Re\left\{\mathbf{z}_{\mathrm{n}}^{\mathrm{mat}}\right\}}, & \text{for } m = n \\ 0, & \text{for } m \neq n \end{cases} \tag{7.9}$$

Then (7.8) can be simply written as a summation of the traces of the matrix as

$$P_{\mathrm{rad}} = \sum_{n=1}^{N_t} |v_n|^2 \Re\left\{\mathrm{diag}\left(\left(\mathbf{Y}^{\mathrm{MoM}}\right)^{\mathrm{H}} \mathbf{Z}^{\mathrm{rad}} \mathbf{Y}^{\mathrm{MoM}}\right)_{\mathrm{nn}}\right\} \tag{7.10}$$

Similar to LU factorization method, the trace method is suitable solve problems with the same body excited differently. For example, a parameter sweep on the temperature can be easily performed by inverse the

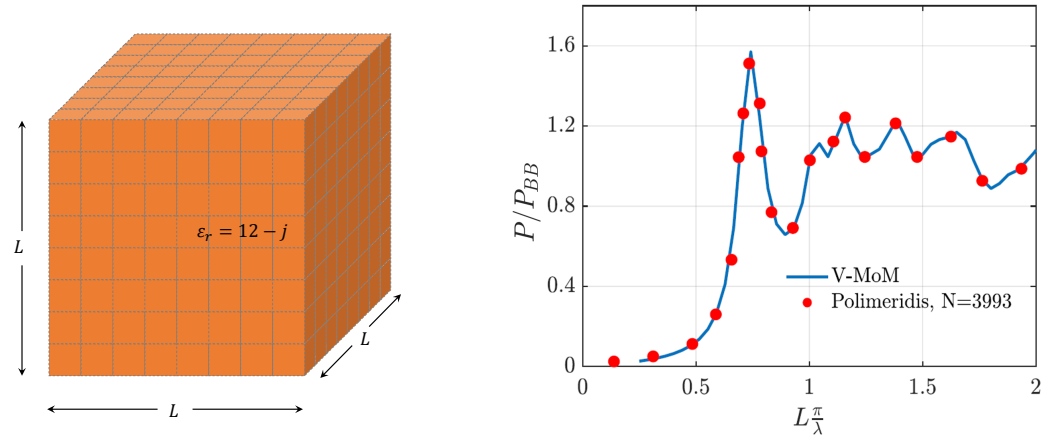

(a) (b)

Figure 7.1: (a) A cube of edge L with an effective permittivity of $\varepsilon_r = 12 - j$ kept at a certain temperature T emitting power in free space. (b) Thermal emission of the cube as a function of the size of the cube in terms of wavelength, normalized to black body

matrix only once and solve the radiated power with a complexity of $\mathcal{O}(N_t)$ by changing the excitation term for each temperature. One downside of this method is that due to the memory and the computation limitations, the trace method can only perform the inversion up to 24 thousands of unknowns and fails when when dealing with larger problems. Another shortage of the trace method is that it only gives the radiated power but can not reconstruct the field inside the body.

7.2.2. Monte Carlo Simulation

To simulate larger structures one needs to use the CG-FFT to solve the linear system. Sufficient number of simulations are needed and the results are averaged to model the incoherent excitation. Suppose M simulations are done with the arbitrary phase excitation $\mathbf{v}_m$ as described in (7.4), the equivalent currents of the m-th linear system is solved by

$$\mathbf{v}_m = \left(\mathbf{Z}^{\text{mat}} + \mathbf{Z}^{\text{rad}}\right)\mathbf{i}_m \tag{7.11}$$

where $\mathbf{i}_m$ is the solutions of equivalent currents for the m-th similation. The power radiated by the body is the average of those in each simulation, which is written as follows

$$P_{\text{rad}} = \frac{1}{M}\sum_{m=1}^{M} \mathbf{i}_m^H \mathbf{Z}^{\text{rad}} \mathbf{i}_m. \tag{7.12}$$

The field intensity inside the body is derived as

$$\left|\vec{E}(\vec{r}_n)\right| = \left|\frac{1}{M}\cdot\frac{\sum_{m=1}^{M}\mathbf{i}_m(n)}{\sigma_{\text{eff}}(\vec{r}_n)\,\Delta^2}\right|. \tag{7.13}$$

7.3. Results and Validation

The tool is validated by comparing the results with those of [27]. As shown in Fig. 7.1a, a cube of edge L constituted by an ideal material with an effective permittivity of $\varepsilon_r = 12 - j$ and kept at a temperature T is simulated in free space. The power P_{rad} emitted by the cube is calculated versus the frequency with the V-MoM, and normalized to the power P_{BB} that a black body would emit if it had the same geometry of the cube, and if it was kept at the same temperature T. The emitted power from a black body can be written as

$$P_{BB} = 4\pi\frac{6L^2}{\lambda_0^2}\frac{2hf}{e^{\frac{hf}{k_B T}} - 1} \tag{7.14}$$

Fig. 7.1b shows the comparison between the V-MoM and the result of [27] using $N = 3993$ unknowns. It is seen that the results from V-MoM and [27] are in perfect agreement.

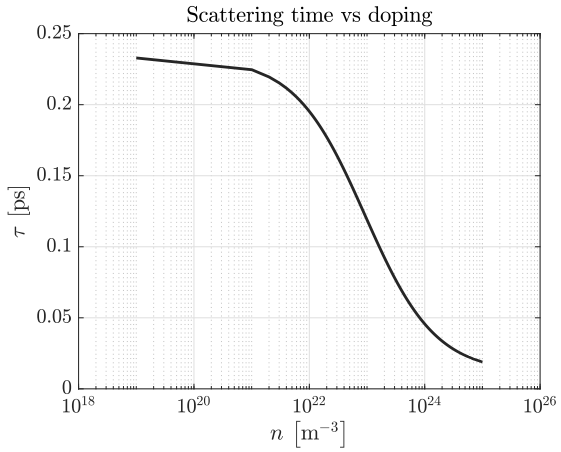

Figure 7.2: The scattering time τ inside the crystalline silicon as a function of the doping level n

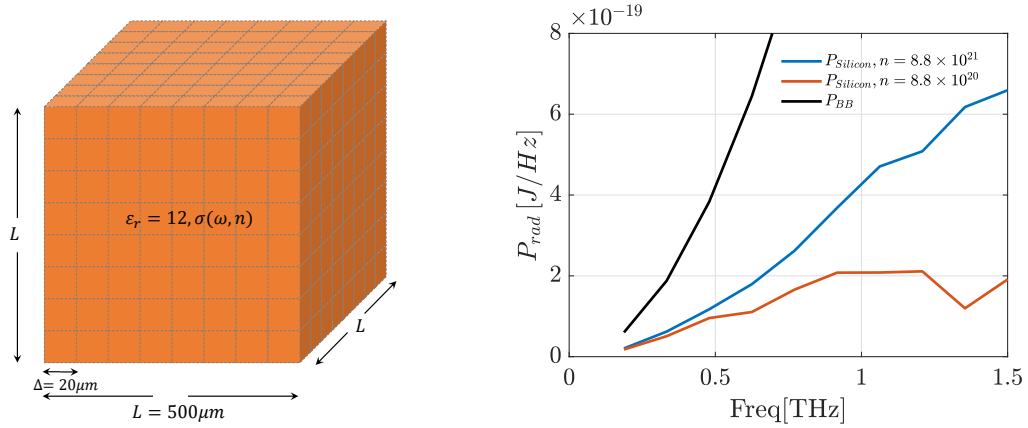

Figure 7.3: (a) A n doped crystalline silicon cube of edge $L = 500\,\mu$m sample into $25 \times 25 \times 25$ voxels of edge $\Delta = 20\,\mu$m. (b) Thermal emission from the cube as a function of frequency for $n = 8.8 \times 10^{21}$ m^{-3}, $n = 8.8 \times 10^{20}$ m^{-3} and black body respectively.

Then a realistic doped crystalline silicon cube is studied using the V-MoM as shown in Fig. 7.3a A doped silicon cube of edge $L = 500\,\mu$m with a relative permittivity of $\varepsilon_r = 12$ and a conductivity $\sigma(\omega, n)$ is discretized into $25 \times 25 \times 25$ voxels of edge $\Delta = 20\,\mu$m. The conductivity of the silicon, according to Drude's Model [13], depends both on frequency and the doping of the material and can be written as

$$\sigma(\omega, n) = \frac{\sigma_{\text{qs}}}{1 + j\omega\tau} \tag{7.15}$$

where τ, the scattering time in the material, depends on the electron density in the silicon [28] as shown in Fig. 7.2and σ_{qs} is the quasi-static limit of the conductivity and can be written as

$$\sigma_{\text{qs}} = \frac{ne^2\tau}{m_{\text{eff}}} \tag{7.16}$$

where n is the electron density in the silicon, $e = 1.6 \times 10^{-19}$C is the charge of an electron and $m_{\text{eff}} = 0.29m_e$ is the effective mass of an electron is silicon, with $m_e = 9.1 \times 10^{-31}$kg. Fig. 7.3b shows the results of the thermal radiation from the silicon cube doped by $n = 8.8 \times 10^{21}$ m^{-3} and $n = 8.8 \times 10^{20}$ m^{-3}, and then compared with the one from a black body.

7.4. Discussion

The results from the V-MoM have the same order of magnitude as the predictions from the black body. It is seen that the radiated power from the silicon grows less as function of frequency compared with the one from

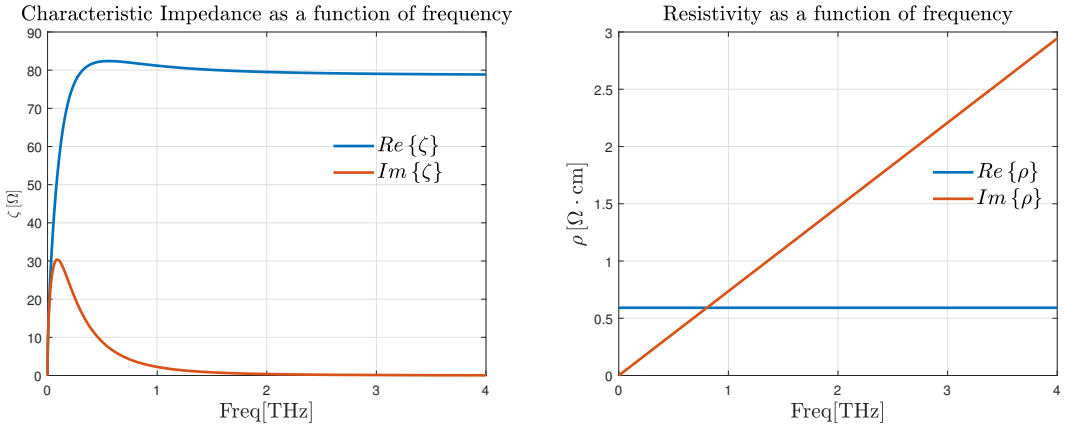

(a) (b)

Figure 7.4: (a) Characteristic impedance of crystalline silicon with $n = 8.8 \times 10^{21}$ m^{-3} doping. (b) Resistivity of the n doped silicon

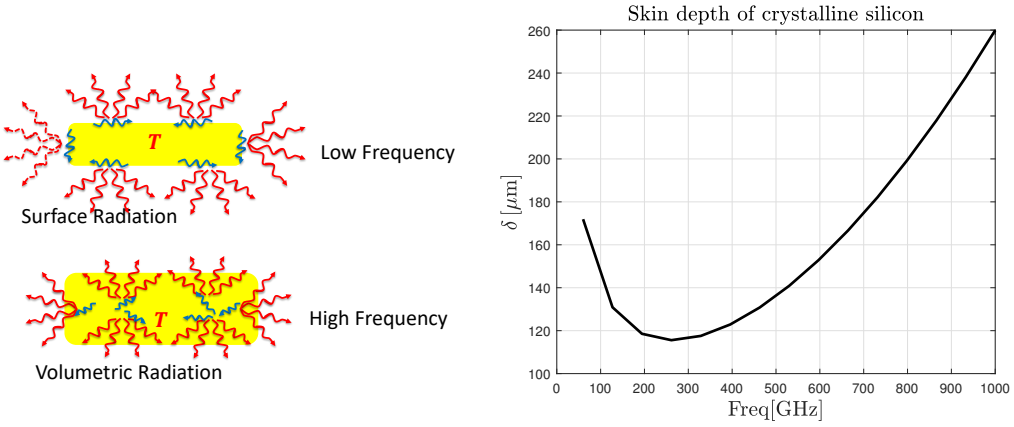

(a) (b)

Figure 7.5: Depiction of the surface and volumetric radiation in the low frequency, and high frequency regime, and (b) skin depth of cristalline silicon with $n = 8.8 \times 10^{21}$ m^{-3}

the black body. This is because the Drude's model suggests the sources are weaker at higher frequencies, due to the decrease of the conductivity. Fig. 7.4 shows the characteristic impedance and the resistivity of crystalline silicon with $n = 8.8 \times 10^{21}$ m^{-3} doping. As shown in Fig. 1.3b, the imaginary part of the resistivity grows linearly with the frequency, resulting into a decreasing conductivity at high frequency. At high frequency, due to the faster varying fields, the electrons are less prone to move, since the fast inversion of the field direction does not allow them to accelerate sufficiently. This implies that, according to the definition of the sources in (7.4), the body radiates less power..

The reduction of the losses at high frequencies, also implies a reduction of the attenuation constant within the material, therefore also the inner parts of the body contribute to the emission, not only the ones on the surface,as depicted in Fig. 7.5a. Fig. 7.5b shows the skin depth of the silicon doped with $n = 8.8 \times 10^{21}$ m^{-3}. Despite the strong source intensity at low frequency, the large attenuation allows only the outer part of the body to radiate, while the contribution originated from the inner parts are strongly attenuated before reaching the surface. Therefore, it is seen in Fig. 7.3b that at low frequency regime the radiation from the doped silicon behaves similarly to the one from black body. While at high frequencies,the attenuation is less, due to the decrease of the conductivity. While at high frequency, due to the reduced attenuation, caused by the decreased conductivity, the inner part of the body also contributes to the radiation, compensating for the decrease of the sources' intensity. As a result, the behaviour of the power radiated by the material deviates from the one radiated by an ideal black body.

Fig. 7.6 shows the results from a simulation of the same cube using incoherent excitations. The voxels are excited one by one, according to (7.9), and the radiated power contribution from the voxels on the X-Y plane

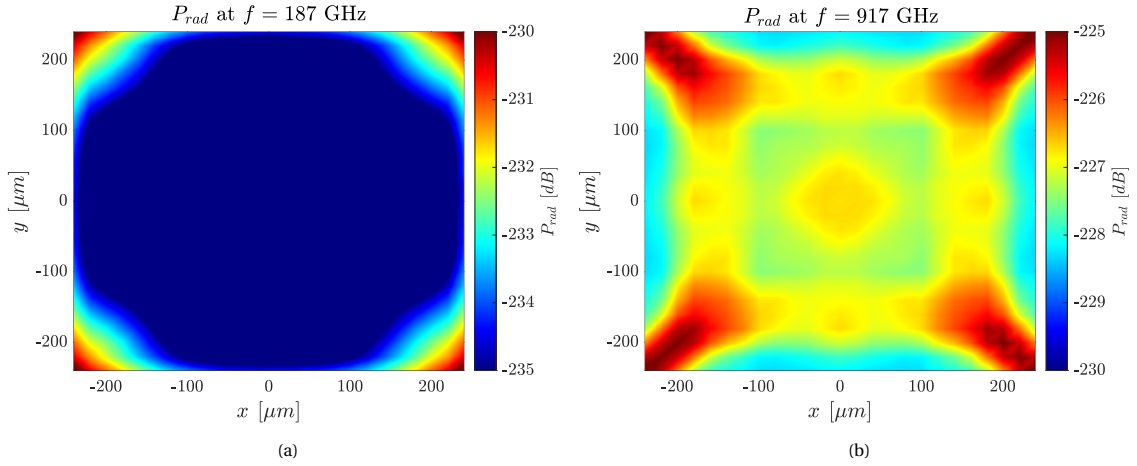

Figure 7.6: The contribution of the elements on the X-Y plane of the lossy silicon cube to the total radiated power at (a) $f = 187$ GHz and (b) $f = 917$ GHz

of the cube are recorded and compared with a same dynamic range of 5dB. It is seen that at low frequency, as shown in Fig. 7.6a, the radiation only comes from the surface area. At high frequency, the contributions are more uniform and volumetric.

7.5. Waveguide Model for Measurement

The predictions of the power radiated by a lossy semiconductor are going to be experimentally verified, by measuring the power radiated by a silicon slab placed inside a waveguide, to avoid power leakage outside of the measurements setup. However, the V-MoM is highly ill conditioned for such setup, therefore a plane wave expansion of the field inside a waveguide is used to calculate the radiated power.

As shown in Fig. 7.7a, the power radiated by an elementary source located at (x', y', z') inside a waveguide is with cross section $a \times b$ is given is given by

$$\begin{aligned} P^{\mathrm{wg}} &= P_{\mathrm{x}}^{\mathrm{wg}} + P_{\mathrm{y}}^{\mathrm{wg}} + P_{\mathrm{z}}^{\mathrm{wg}} \\ &= \frac{1}{ab}\frac{1}{\zeta_0}\sum_{m_x}\sum_{m_y}\left\|\bar{\bar{G}}^{\mathrm{ej}}(k_{xm}, k_{ym})\cdot\hat{x}\right\|^2 \cos^2(k_{xm}x')\sin^2(k_{ym}y') \\ &+ \left\|\bar{\bar{G}}^{\mathrm{ej}}(k_{xm}, k_{ym})\cdot\hat{y}\right\|^2 \sin^2(k_{xm}x')\cos^2(k_{ym}y') \\ &+ \left\|\bar{\bar{G}}^{\mathrm{ej}}(k_{xm}, k)_{ym})\cdot\hat{z}\right\|^2 \sin^2(k_{xm}x')\sin^2(k_{ym}y') \end{aligned} \tag{7.17}$$

where $\bar{\bar{G}}^{\mathrm{ej}}$ is the spectral Green's function of the material filling the waveguide, e.g., free space Green's function if the waveguide does not contain any material, or the Green's function of a slab of height h. The origin of the reference system is located at the centre of the left surface of the slab for convenience. As it can be noticed, the power results into an expansion of Floquet modes, arising from the application of the image theorem, that expands the structure periodically. The powers $P_{\mathrm{x}}^{\mathrm{wg}}$, $P_{\mathrm{y}}^{\mathrm{wg}}$, and $P_{\mathrm{z}}^{\mathrm{wg}}$ are th powers radiated by currents oriented along x, y, and z, respectively.The full derivation of the power flowing in a waveguide expressed in a plane wave expansion is reported in Appendix D and the Green's function is derived in Appendix E.

The formula (7.17) is validated with CST by simulating a waveguide having cross section $a \times b = 250\,\mu\mathrm{m} \times 250\,\mu\mathrm{m}$, filled with a lossless silicon slab of size $a \times b \times h = 250\,\mu\mathrm{m} \times 250\,\mu\mathrm{m} \times 250\,\mu\mathrm{m}$, where the currents $\vec{J} = J_x\hat{x} = 6\hat{x}\,\mathrm{A/m^2}$ are located in a cube of edge $\Delta = 5\,\mu\mathrm{m}$, as shown in Fig. 7.7a. To validate the accuracy of the model, different displacements of the source are considered. As shown in Fig. 7.7b, c and d, the source is displaced along x-, y- and z-axis respectively and the power calculated by the analytical model is in good agreement with the CST simulation.

To calculate the total power radiated by the entire lossy silicon slab, (7.17) has to be integrated over the entire considered volume. Suppose the slab has a volume $\mathcal{V}$ and is discretized by voxels of edge Δ, the total

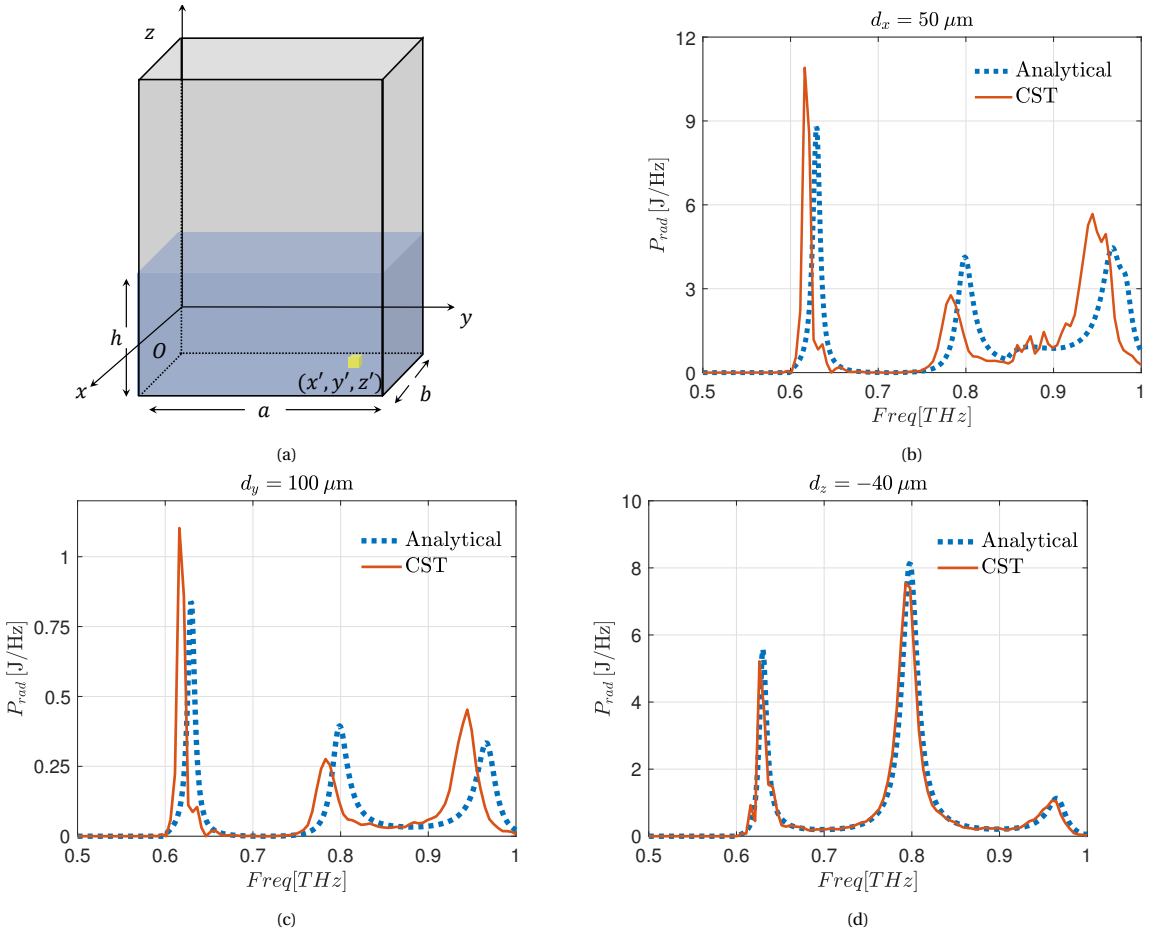

Figure 7.7: (a) Depiction of a slab of size $a \times b \times h$ placed inside a waveguide with an electric source located at (x', y', z'), and the power radiated by the source displaced at (b) $50\,\mu$m (c) $100\,\mu$m, and (d) $-40\,\mu$m along x, y, and z respectively.

power radiated by the slab is summed incoherently, which can be expressed as follows

$$P_{\text{rad}} = |i|^2 \iiint_V P^{\text{wg}}(x', y', z')\, dx'\, dy'\, dz' = |i|^2 \Delta^3 \sum_{n_x=1}^{Nx} \sum_{n_y=1}^{Ny} \sum_{n_z=1}^{Nz} P^{\text{wg}}\left(x_{n_x,n_y,n_z}, y_{n_x,n_y,n_z}, z_{n_x,n_y,n_z}\right). \tag{7.18}$$

where for radiometry problems regarding semiconductors, the impressed current is defined as

$$|i| = \sqrt{4 k_B T \Re\{\sigma(\omega, n)\}}. \tag{7.19}$$

8

Conclusion

8.1. Summary

In this thesis, a fast and efficient full wave simulation tool for high frequency problems is developed using the volume equivalence theorem, the Method of Moments (MoM) and the Conjugate-Gradient Fast Fourier Transform (CG-FFT). The tool is validated with various sources and can handle scattering problems, antennas in transmission and radiometric problems in the terahertz domain.

First the Electric Field Integral Equation (EFIE) is formulated using the volumetric equivalence theorem and by the use of the MoM and discretization of the grid, the problem is resorted to a linear system, which is later solved by the iterative method CG-FFT. The mutual and self reaction integrals are evaluated. The body is designed by a combination of four elementary shapes, namely cuboid, sphere, cylinder, and ellipsoid constituted by materials defined by their relative permittivity and their conductivity, Different excitation terms can be impressed such as plane wave, discrete port and radiometric sources. Results such as field inside the body, far field pattern, power lost in the dielectric and scattering parameters are obtained by post processing the solution of the equivalent currents. Then the tool is validated for multi-layer sphere scattering problems, lens antennas fed by dipoles, and thermal emission from lossy silicon slabs with Mie series, CST, and open literatures respectively. Finally a Graphical User Interface (GUI) is developed using MatLab to enhance the user experience.

This work utilizes the Toeplitz properties of the strcucture grid, combined with the matrix free form CG-FFT algorithm, reduces the calculation time of the radiation matrix, the time to solve the large linear system and the memory requirement dramatically. Moreover, the structured grid also allows users to reuse the pre-computed reaction integrals for problems with same background material but different bodies and excitation terms that can be defined in the same discretization. The tool is validated to be accurate for all three types of problems with a computation speed comparable with commercial software. The results from this tool provide a deeper insight on radiometric problems in the terahertz band using the Drude's model. However, the tool has difficulty simulating high dielectric density structures and metal bodies due to the ill conditioning of such problems. The tool also has an uncertainty when the structure to simulate does not conform with the fixed cuboid grid.

To summarize, the V-MoM was designed as an efficient and accurate tool to simulate high frequency structures of size within several wavelengths for multiple purposes. Several millions of unknown can be handled by the tool with fast convergence and low memory requirements.

8.2. Outlook

The V-MoM's performance reduces when dealing with ill-conditioned probelms introduced by high contrast on the boundaries and matal materials. One possible solution is to implement a pre-conditioner to accelerate the convergence of the tool. Another extension of the tool could be implementing the periodic boundary conditions in the V-MoM to model antenna arrays. Finally, the tool also has potential in modelling superconducting devices such as the MKID for astronomical instrumentation design.

A

Coordinate Free Green's Function

The spatial Green's function used in this thesis is written in the coordinate free form based on [29], resulting into a more efficient implementation when calculating the reaction integrals and the radiated fields. Given an homogeneous material, having relative permittivity ε_r, the Green's function evaluated at $\vec{r}$ due to sources located ar $\vec{r}\,'$, can be expressed as follows

$$\bar{\bar{G}}\left(\vec{r},\vec{r}\,'\right) = -jk\zeta\left[\left(\bar{\bar{I}}-\hat{R}\hat{R}\right)g\left(\vec{R}\right)+\frac{1}{jk_0\sqrt{\varepsilon_r}\,|\vec{r}|}\left(\bar{\bar{I}}-3\hat{R}\hat{R}\right)g\left(\vec{r}\right)-\frac{1}{k_0^2\varepsilon_r\,|\vec{r}|^2}\left(\bar{\bar{I}}-3\hat{R}\hat{R}\right)g\left(\vec{r}\right)\right] \tag{A.1}$$

$\bar{\bar{I}}$ is the identity dyad, $\vec{R}$ is the relative distance between the source and the observation point defined as (A.2), $\hat{R}$ is the unit vector associated with $\vec{R}$, and defined as (A.3), and $g\left(\vec{R}\right)$ is the scalar Green's function expressed as

$$\vec{R} = \vec{r} - \vec{r}\,' \tag{A.2}$$

$$\hat{R} = \frac{\vec{R}}{\left|\vec{R}\right|} \tag{A.3}$$

$$g\left(\vec{R}\right) = \frac{e^{-jk_0\sqrt{\varepsilon_r}|\vec{R}|}}{4\pi\left|\vec{R}\right|}. \tag{A.4}$$

B

Electric Field Evaluated at the Source Domain

The electric field $\vec{E}^s(\vec{r})$ generated by electric sources located within the volume $\mathcal{V}$ can be calculated with the following expression,

$$\vec{E}^s(\vec{r}) = \iiint_{\mathcal{V}-\mathcal{V}_\delta} \bar{\bar{G}}^{\text{hs}}(\vec{r},\vec{r}\,') \cdot \vec{J}(\vec{r}\,')\, d\vec{r}\,' + j\frac{\mathbf{L}_{\mathbf{V}_\delta} \cdot \vec{J}(\vec{r})}{\omega\varepsilon_0} + \iiint_{\mathcal{V}_\delta} \bar{\bar{G}}^{\text{hs}}(\vec{r},\vec{r}\,') \cdot \vec{J}(\vec{r}\,')\, d\vec{r}\,'. \tag{B.1}$$

where $\mathcal{V}_\delta$ is a small volume around the observation point and $\mathbf{L}_{\mathbf{V}_\delta}$ is an operator depends on the shape of the volume $\mathcal{V}_\delta$. By using the dyadic operator given by [30] and [31], and assuming the volume is spherical [32], one can write $\vec{E}^s(\vec{r})$ as

$$\vec{E}^s(\vec{r}) = \iiint_{\mathcal{V}-\mathcal{V}_\delta} \bar{\bar{G}}^{\text{hs}}(\vec{r},\vec{r}\,') \cdot \vec{J}(\vec{r}\,')\, d\vec{r}\,' + j\frac{\vec{J}(\vec{r})}{3\omega\varepsilon_0} + \iiint_{\mathcal{V}_\delta} \bar{\bar{G}}^{\text{hs}}(\vec{r},\vec{r}\,') \cdot \vec{J}(\vec{r}\,')\, d\vec{r}\,'. \tag{B.2}$$

As shown in Fig. B.1, the first term is the contribution of the currents located in the volume outside $\mathcal{V}_\delta$, the second term is the contribution of the currents located at $\vec{r}\,'$, and the third term is the field generated by the currents located within $\mathcal{V}_\delta$. By summing and subtracting $\bar{\bar{G}}^{\text{hs}}(\vec{r},\vec{r}\,') \cdot \vec{J}(\vec{r})$ in the latter one can write as follows

$$\vec{E}^s(\vec{r}) = \iiint_{\mathcal{V}-\mathcal{V}_\delta} \bar{\bar{G}}^{\text{hs}}(\vec{r},\vec{r}\,') \cdot \vec{J}(\vec{r}\,')\, d\vec{r}\,' + j\frac{\vec{J}(\vec{r})}{3\omega\varepsilon_0} + \iiint_{\mathcal{V}_\delta} \bar{\bar{G}}^{\text{hs}}(\vec{r},\vec{r}\,') \cdot \vec{J}(\vec{r})\, d\vec{r}\,' + \iiint_{\mathcal{V}_\delta} \bar{\bar{G}}^{\text{hs}}(\vec{r},\vec{r}\,') \cdot \left(\vec{J}(\vec{r}\,') - \vec{J}(\vec{r})\right) d\vec{r}\,'. \tag{B.3}$$

To solve the contribution of the third contribution as described in Fig. B.1c, by choosing $\mathcal{V}_\delta$ as a spherical volume centred at $\vec{r}$, and having a as radius, by resorting to the integration in spherical coordinates one can write

$$\int_0^a \int_0^{2\pi} \int_0^{\pi} \bar{\bar{G}}^{\text{hs}}(\rho,\theta,\phi)\, \rho^2 \sin\theta\, d\rho\, d\theta\, d\phi \tag{B.4}$$

expressing the Green's function in spherical coordinates as follows

$$\bar{\bar{G}}^{\text{hs}}(\rho,\theta,\phi) = -\frac{jk\zeta}{4\pi}\frac{e^{-jk\rho}}{\rho}\left\{\left[\bar{\bar{I}} - \hat{R}\hat{R}\right] - \frac{j}{k\rho}\left[\bar{\bar{I}} - 3\hat{R}\hat{R}\right] - \frac{1}{k^2\rho^2}\left[\bar{\bar{I}} - 3\hat{R}\hat{R}\right]\right\} \tag{B.5}$$

and by substituting it in (B.4), one obtains as follows

$$\begin{aligned} -\frac{jk\zeta}{4\pi}\int_0^a e^{-jk\rho}\rho \int_0^{2\pi}\int_0^{\pi}\left[\bar{\bar{I}} - \hat{R}\hat{R}\right]\sin\theta\, d\rho\, d\theta\, d\phi - \frac{\zeta}{4\pi}\int_0^a e^{-jk\rho}\int_0^{2\pi}\int_0^{\pi}\left[\bar{\bar{I}} - 3\hat{R}\hat{R}\right]\sin\theta\, d\rho\, d\theta\, d\phi \\ + \frac{j\zeta}{4\pi k}\int_0^a \frac{e^{-jk\rho}}{\rho}\int_0^{2\pi}\int_0^{\pi}\left[\bar{\bar{I}} - 3\hat{R}\hat{R}\right]\sin\theta\, d\rho\, d\theta\, d\phi. \end{aligned} \tag{B.6}$$

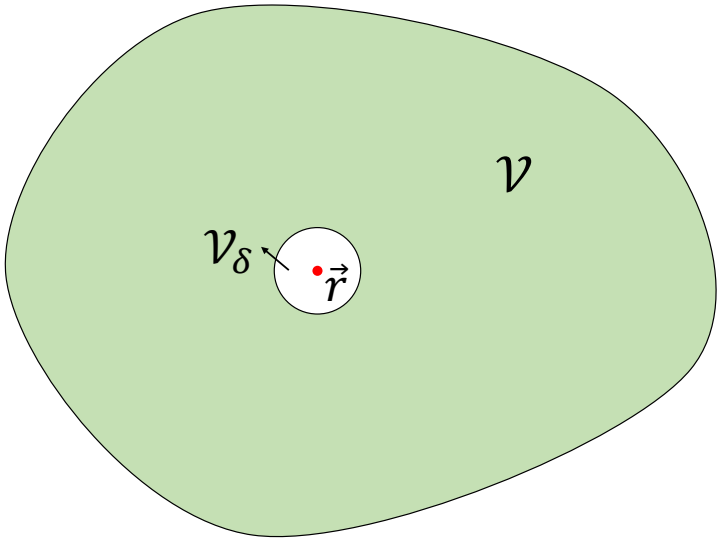

Figure B.1: Depiction of the three contributions to the electric field

The formula above (B.6) has a combination of integrals of dyads calculated over the entire solid angle, and radial integrals. Let as now consider the angular integrals first. By expressing the cartesian components of the unit vector $\hat{R}$ in terms of (θ,ϕ) as follows

$$\hat{R} = \sin\theta\cos\phi\hat{x} + \sin\theta\sin\phi\hat{y} + \cos\theta\hat{z} \tag{B.7}$$

the dyad $\hat{R}\hat{R}$ can be expressed as

$$\hat{R}\hat{R} = \begin{bmatrix} \sin^2\theta\cos^2\phi & \sin^2\theta\cos\phi\sin\phi & \sin\theta\cos\theta\cos\phi \\ \sin^2\theta\cos\phi\sin\phi & \sin^2\theta\sin^2\phi & \sin\theta\cos\theta\sin\phi \\ \sin\theta\cos\theta\cos\phi & \sin\theta\cos\theta\sin\phi & \cos^2\theta \end{bmatrix}. \tag{B.8}$$

Therefore, the angular integrals of (B.6) can be closed as follows

$$\int_0^{2\pi}\int_0^{\pi} \hat{R}\hat{R}\sin\theta d\theta d\phi = \begin{bmatrix} \frac{4\pi}{3} & 0 & 0 \\ 0 & \frac{4\pi}{3} & 0 \\ 0 & 0 & \frac{4\pi}{3} \end{bmatrix} \tag{B.9}$$

Therefore the integrals that include the unitary dyad can be written as

$$\int_0^{2\pi}\int_0^{\pi} \left[\bar{\bar{I}} - \hat{R}\hat{R}\right]\sin\theta d\theta d\phi = \frac{8\pi}{3}\bar{\bar{I}} \tag{B.10}$$

and

$$\int_0^{2\pi}\int_0^{\pi} \left[\bar{\bar{I}} - 3\hat{R}\hat{R}\right]\sin\theta d\theta d\phi = \bar{\bar{0}} \tag{B.11}$$

where $\bar{\bar{0}}$ is the null dyad. By substituting (B.10) and (B.11) into (B.6), one obtains as follows

$$-jk\zeta\frac{2}{3}\int_0^a e^{-jk\rho}\rho d\rho = -jk\zeta\frac{2}{3}\left[\frac{e^{-jk\rho}\left(1+jk\rho\right)}{k^2}\right]_0^a = -j\frac{2}{3}\frac{1}{\omega\varepsilon_0}\left[e^{-jka}\left(1+jka\right)-1\right] \tag{B.12}$$

By combining all the results, the field $\vec{E}^s(\vec{r})$ becomes as follows

$$\begin{aligned}\vec{E}^s(\vec{r}) &= \iiint_{V-V_\delta} \bar{\bar{G}}^{\mathrm{hs}}(\vec{r},\vec{r}\,')\cdot\vec{J}(\vec{r}\,')\,d\vec{r}\,' + j\frac{1}{3\omega\varepsilon_0}\vec{J}(\vec{r}) - j\frac{2}{3}\frac{1}{\omega\varepsilon_0}\left[e^{-jka}(1+jka)-1\right]\vec{J}(\vec{r}) \\ &+ \iiint_{V_\delta} \bar{\bar{G}}^{\mathrm{hs}}(\vec{r},\vec{r}\,')\cdot\left(\vec{J}(\vec{r}\,')-\vec{J}(\vec{r})\right)d\vec{r}\,' \\ &= \iiint_{V-V_\delta} \bar{\bar{G}}^{\mathrm{hs}}(\vec{r},\vec{r}\,')\cdot\vec{J}(\vec{r}\,')\,d\vec{r}\,' + \frac{1}{j\omega\varepsilon_0}\left(\frac{2}{3}e^{-jka}(1+jka)-1\right)\vec{J}(\vec{r}) \\ &+ \iiint_{V_\delta} \bar{\bar{G}}^{\mathrm{hs}}(\vec{r},\vec{r}\,')\cdot\left(\vec{J}(\vec{r}\,')-\vec{J}(\vec{r})\right)d\vec{r}\,'\end{aligned} \quad . \tag{B.13}$$

C

Error Analysis

To use the V-MoM in a valid regime, it is important to investigate the causes of the error and how much error those causes will contribute. Besides representing shapes properly, the key to achieve accurate simulation of the numerical tool is to have enough basis function to describe the field distribution. In the previous chapter a rough estimation of $\Delta < \lambda_d/30$ is given as the constraint for the tool. However, the size of the basis function Δ depends not only on the wavelength in the dielectric λ_d, but also on how propagation of the field in the structure. Consider the same sphere with a relative permittivity of ε_r impinged by plane waves from 100GHz to 1THz from broadside as shown in Fig. C.2. The field on the entire sphere from the V-MoM is compared with CST.

Fig. C.2 shows the relative error the V-MoM makes with respect to CST. The size of basis function is chosen to be $\Delta = 16.7\mu m$ here in this case. It is shown that the results of a $\varepsilon_r = 2$ sphere at 1THz are more accurate than a $\varepsilon_r = 4$ sphere at 500GHz, although the former case has a worse sampling ($\lambda_d/13$) than the latter one ($\lambda_d/18$) in terms of wavelength in the dielectric. The high permittivity not only has an impact on the size of the basis function, but also introduces fast varying fields. Two main factors considered in this thesis: dielectric size of the resonator and the flections in it.

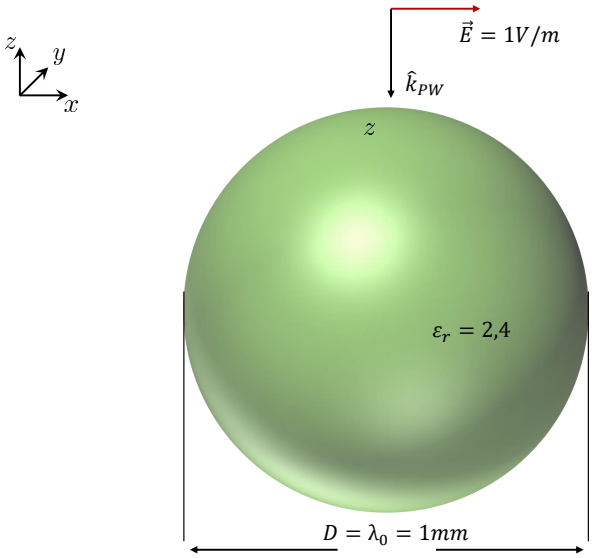

Figure C.1: Sphere with $\varepsilon_r = 2,4$ impinged by a plane wave from broad side

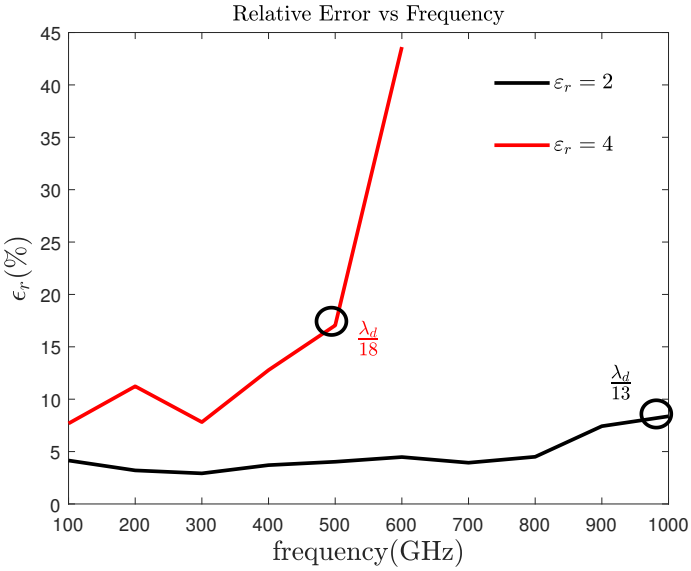

Figure C.2: Error of the field from the V-MoM with respect to CST

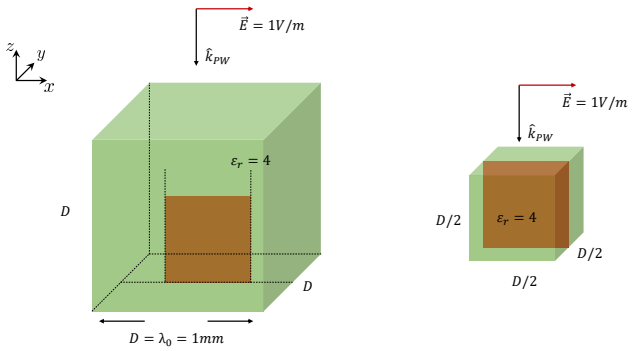

Figure C.3: A $0.5\lambda_0$ cube and $1\lambda_0$ cube incident by a plane wave from broadside

C.1. Dielectric Size

The number of propagation modes increases as the dielectric size of the resonator grows. To study this effect and separate the effect of curvature of the resonator, a $1\lambda_0 \times 1\lambda_0 \times 1\lambda_0$ cube and a $0.5\lambda_0 \times 0.5\lambda_0 \times 0.5\lambda_0$is simulated with a plane wave incident from broadside at 300GHz as shown in Fig. C.3. The results are plotted in a frame of size $0.5\lambda_0 \times 0.5\lambda_0 \times 0.5\lambda_0$ at the most intense region in the cubes on the X-Z plane.

It is shown in Fig C.4 that the field inside the larger cube (Fig. C.4b) varies much faster than the field in the smaller cube (Fig. C.4a) due to the difference between the excited propagation modes. This means the larger the structure is, the more resonate ii will be and thus requires finer basis function to model the field distribution.

A parametric analysis is done to show the error that the V-MoM commits for different size of resonators ($1\lambda_0$, $0.5\lambda_0$ and $0.25\lambda_0$). Different samplings are applied to the structures from poorly sampled ($\Delta < \lambda_d/10$) to well sampled ($\Delta > \lambda_d/30$). The relative error the tool commits with respect to CST in Fig. C.5 shows that the tool ,with the same sampling rate, has different accuracies for different sizes of resonators. For a quarter-wavelength cube, the tool gives a relative error less than 10% with $\Delta = \lambda_d/7$ while for a one-wavelength cube, the sampling needs t be $\Delta < \lambda_d/25$ to achieve the same accuracy. This implies that the number of basis functions needed does not simply scale with the dielectric size of the resonators as $N_t \propto \mathcal{V}(\lambda_0)$, but with a higher order dependence that the user needs to be careful of for highly resonant structures.

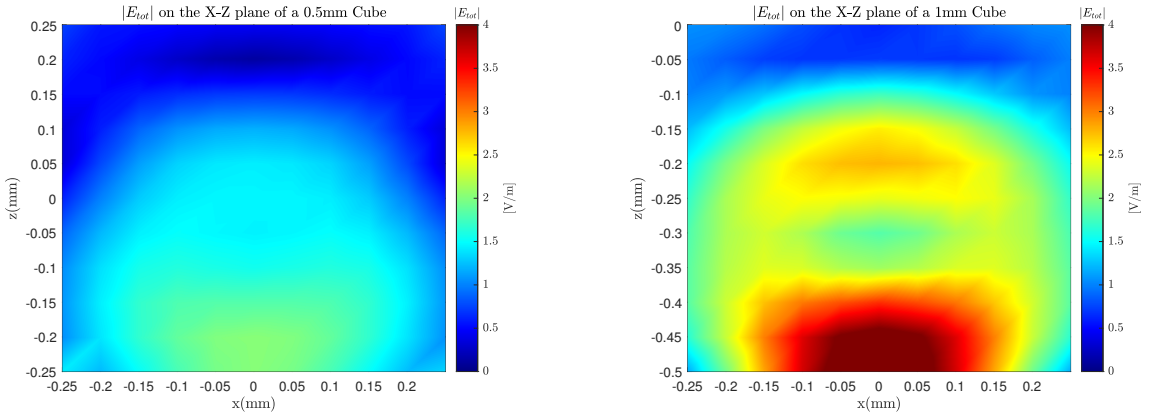

(a) (b)

Figure C.4: The field inside the (a)$1\lambda_0$ cube and (b) $0.5\lambda_0$ cube

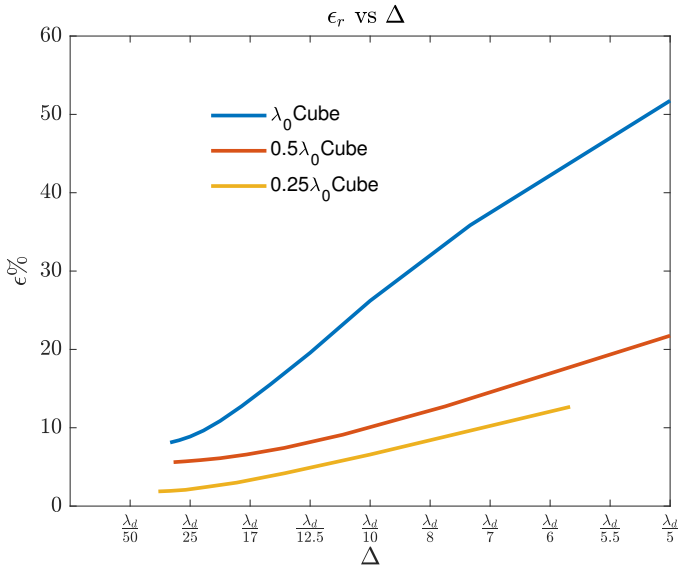

Figure C.5: Relative error the tool commits with respect to CST for $1\lambda_0$, $0.5\lambda_0$ and $0.25\lambda_0$ cubes

C.2. Reflection

Besides the dielectric size of the resonator, the contrast on the boundaries between the structure and the background also contributes to the fast varying field, by resulting strong reflected fields in the body. In Fig. C.6 two cubes with the same dielectric size ($\mathcal{V} = \sqrt{2}\lambda_0$) but different relative permittivity ($\varepsilon_r = 2, 8$) are simulated using the tool and compared with CST for relative error. The total field on the X-Z plane in the cube is plotted in Fig. C.7. Fig. C.7b shows that there is high reflected field in the top region of the denser cube, compared with less reflections in the lighter cube in Fig. C.7a. In Fig.C.8 the relative error committed by the tool of the two simulations are plotted with respect to CST, as a function of the size of the basis function. This result implies that for this dielectric size, a sampling of $\Delta = \lambda_d/10$ is sufficient to describe the propagation modes in the resonator. However, to describe the reflections, one needs to sample the denser resonator at $\Delta < \lambda_d/20$.

To further illustrate the impact of reflections on the accuracy of the simulation, in Fig. C.9, cubes share the same dielectric size ($\mathcal{V} = \lambda_0$) with different relative permittivity ($\varepsilon_r = 2, 4, 6, 9, 12$) are simulated using the tool. Then those structures are also simulated in a so called "normalized background" with $\varepsilon_r^{\mathrm{BG}} = \varepsilon_r/2$ to get the same reflections on the boundaries. The structure are sampled with $\Delta = \lambda_d/30$. Fig. shows the relative error of the fields compared with CST, with an addition set of simulation using larger structures of $\mathcal{V} = 2\lambda_0$. It is seen that if the background is free space, the error increases as the contrast on the boundaries rises. However, if the material of the background is normalized, the error tends to be stable for high dielectric density resonators, as

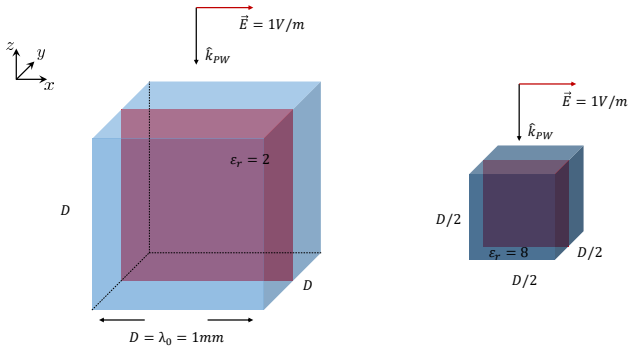

Figure C.6: Two resonators with the same dielectric size: $1\lambda_0$ cube with $\varepsilon_r = 2$ and $0.5\lambda_0$ cube with $\varepsilon_r = 8$

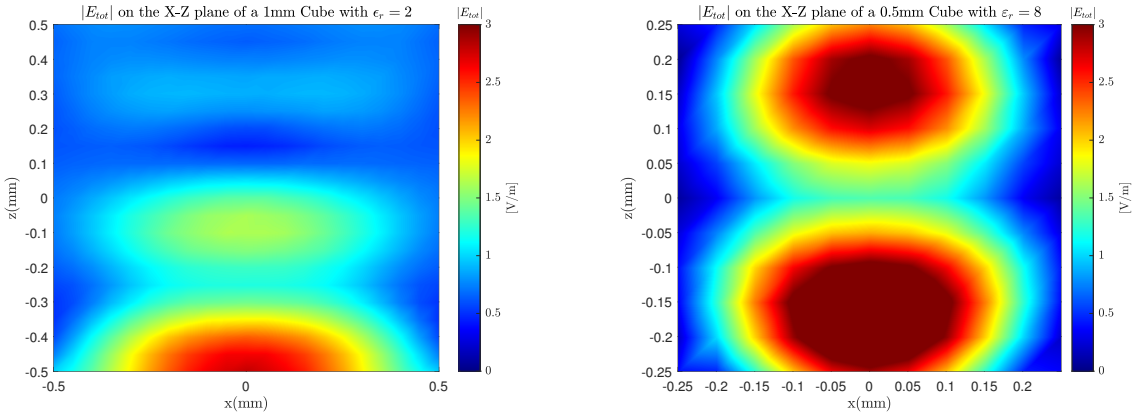

(a) (b)

Figure C.7: The field inside the (a)$1\lambda_0$ cube with $\varepsilon_r = 2$ and (b) $0.5\lambda_0$ cube with $\varepsilon_r = 8$

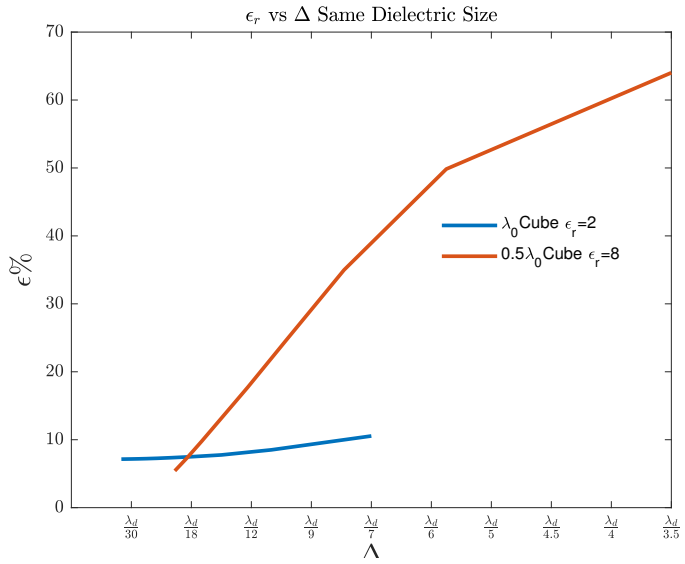

Figure C.8: Relative error of field in the two resonators with the same dielectric size with respect to CST

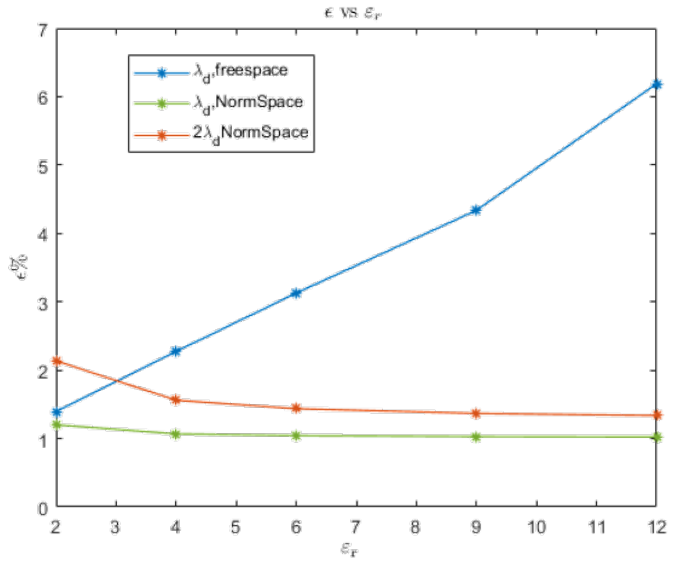

Figure C.9: Relative error of field in different dielectric constant cubes of the same size in normalized background material

the reflections are the same in all cases. With these experiments, the two main factors that affect the accuracy of this tool are itentified as the contrast on the boundary and the size of the structure in terms of wavelength.

D

Power Radiated in Waveguide by Arbitrary Oriented Sources

Let us consider a waveguide with x and y being its transverse dimensions and z being the longitudinal one as shown in Fig. 7.7a. The waveguide is filled with a dielectric slab of thickness h backed by a ground plane. The chosen reference system has its origin at the centre of left surface of the slab, and the waveguide cross section has dimensions a and b along x and y, respectively. Let $\vec{e}\left(\vec{r},\vec{r}'\right)$ be the electric field produced at the position $\vec{r}$ by electric sources located at $\vec{r}'$, and oriented along $\hat{p}_i$. By resorting to the spectral Green's function $\bar{\bar{G}}\left((k_x,k_y)\right)$, the field can be written as

$$\vec{E}\left(\vec{r},\vec{r}',h\right)=\frac{1}{4\pi^2}\int_{-\infty}^{+\infty}\int_{-\infty}^{+\infty}\bar{\bar{G}}^{ej}\left(k_x,k_y\right)\cdot\hat{p}_i e^{-jk_x(x-x')}e^{-jk_y(y-y')}e^{-jk_z\left(z-\frac{h}{2}\right)}dk_x dk_y \tag{D.1}$$

Due to the presence of perfect electric conductor walls, the image theorem can be applied as shown in Fig. D.1, allowing to replicate the sources located at $\left(x',y'\right)$ as shown below

$$\vec{E}\left(\vec{r},\vec{r}',h\right)=\frac{1}{4\pi^2}\int_{-\infty}^{\infty}\int_{-\infty}^{\infty}\sum_{n_x}\sum_{n_y}\bar{\bar{G}}^{ej}\left(k_x,k_y\right)\cdot\hat{p}_i F_{\text{im}}^{\text{i}}\left(x',y'\right)e^{-jk_x(x-2n_x a)}e^{-jk_y(y-2n_y b)}e^{-jk_z\left(z-\frac{h}{2}\right)}dk_x dk_y, \tag{D.2}$$

With $F_{\text{im}}^{\text{i}}\left(x',y'\right)$ describing the position and the orientation sources oriented along $\hat{p}_i$. By using the relations

$$\sum_{n_x=-\infty}^{\infty}e^{jk_x n_x 2a}=\frac{\pi}{a}\sum_{m_x=-\infty}^{\infty}\delta\left(k_x-k_{xm}\right),\quad k_{xm}=\frac{\pi m_x}{a} \tag{D.3}$$

$$\sum_{n_y=-\infty}^{\infty}e^{jk_y n_y 2a}=\frac{\pi}{b}\sum_{m_y=-\infty}^{\infty}\delta\left(k_y-k_{ym}\right),\quad k_{ym}=\frac{\pi m_y}{b} \tag{D.4}$$

and by calculating the integrals of the Dirac deltas, (D.2) becomes as follows

$$\vec{E}^{\,i}\left(\vec{r},\vec{r}',h\right)=\frac{1}{4ab}\sum_{m_x=-\infty}^{\infty}\sum_{m_y=-\infty}^{\infty}\bar{\bar{G}}^{ej}\left(k_{xm},k_{ym}\right)\cdot\hat{p}_i F_{\text{im}}^{\text{i}}\left(x',y'\right)e^{-jk_{xm}x}e^{-jk_{ym}y}e^{-jk_{zm}\left(z-\frac{h}{2}\right)} \tag{D.5}$$

The corresponding magnetic field can be written as

$$\vec{H}^{i}\left(\vec{r},\vec{r}',h\right)=\frac{1}{4ab}\frac{1}{\zeta_0}\sum_{m_x=-\infty}^{\infty}\sum_{m_y=-\infty}^{\infty}\hat{k}_m\times\left(\bar{\bar{G}}^{ej}\left(k_{xm},k_{ym}\right)\cdot\hat{p}_i\right)F_{\text{im}}^{\text{i}}\left(x',y'\right)e^{-jk_{xm}x}e^{-jk_{ym}y}e^{-jk_{zm}\left(z-\frac{h}{2}\right)}. \tag{D.6}$$

The power radiated in the waveguide by an elementary source located at $\vec{r}\,'$ can be obtained by integrating the Poynting vector on the surface $\mathscr{S}_{\text{wg}}$ located at $z=h$ in the waveguide, as

$$P_{\text{wg}}^{i}=\text{Re}\left\{\iint_{\mathscr{S}_{\text{wg}}}\vec{E}\left(\vec{r},\vec{r}',h\right)\times\vec{H}^{*}\left(\vec{r},\vec{r}',h\right)\cdot\hat{z}d\vec{r}\right\} \tag{D.7}$$

Figure D.1: Images of source oriented along (a) x-, (b) y-, and (c) z-axis due to the presence of perfect electric conductor walls of the waveguide

which by using the plane wave expansion of the fields, can be rewritten as

$$P_{\text{wg}}^{\text{i}} = \frac{1}{16\,(ab)^2}\frac{1}{\zeta_0}\,\text{Re}\Bigg\{\sum_{m_x}\sum_{m_y}\sum_{m_x'}\sum_{m_y'}\Big\{\Big(\bar{\bar{G}}^{ej}\left(k_{xm},k_{ym}\right)\cdot\hat{p}_i\Big)\times\Big[\hat{k}_{m'}\times\Big(\bar{\bar{G}}^{ej^*}\left(k_{xm},k_{ym}\right)\cdot\hat{p}_i\Big)\Big]\Big\}\cdot\hat{z}$$
$$\left|F_{\text{im}}^{\text{i}}\left(x',y'\right)\right|^2 e^{-jk_{zm}\left(z-\frac{h}{2}\right)}e^{jk_{zm}'\left(z-\frac{h}{2}\right)}\iint\limits_{\mathscr{S}_{\text{wg}}} e^{-j\left(k_{xm}-k_{xm'}\right)x}e^{-j\left(k_{ym}-k_{ym'}\right)y}\,d\vec{r}\Bigg\} \tag{D.8}$$

The vector products of (D.8) can be rewritten as

$$\Big(\bar{\bar{G}}^{ej}\left(k_m,k_y\right)\cdot\hat{p}_i\Big)\times\Big[\hat{k}_{m'}\times\Big(\bar{\bar{G}}^{ej^*}\left(k_m',k_y'\right)\Big)\cdot\hat{p}_i\Big]\cdot\hat{z} =$$
$$\Big[\hat{k}_m\Big|\bar{\bar{G}}^{ej}\left(k_m,k_y\right)\cdot\hat{p}_i\Big|^2-\Big(\bar{\bar{G}}^{ej}\left(k_m,k_y\right)\cdot\hat{p}_i\Big)\Big(\bar{\bar{G}}^{ej^*}\left(k_m,k_y\right)\cdot\hat{p}_i\cdot\hat{k}_m\Big)\Big]\cdot\hat{z} \tag{D.9}$$

with $\hat{p}_i\in\{\hat{x},\hat{y},\hat{z}\}$. Since the operator $\bar{\bar{G}}^{ej^*}\left(k_m,k_y\right)\cdot\hat{p}_i$ extracts the transverse component, that is orthogonal to $\hat{k_m}$, (D.9) becomes

$$\Big|\bar{\bar{G}}^{ej}\left(k_m,k_y\right)\cdot\hat{p}_i\Big|^2\hat{k}_m\cdot\hat{z}=\Big|\bar{\bar{G}}^{ej}\left(k_m,k_y\right)\cdot\hat{p}_i\Big|^2\hat{k}_{zm} \tag{D.10}$$

And the integral can be closed as

$$\iint_{S_{\text{wg}}} e^{-j\left(k_{xm}-k_{xm'}\right)x} e^{-j\left(k_{ym}-k_{ym'}\right)y} d\vec{r} =$$

$$ab\left(\frac{\sin\left(\pi\left(m_x-m_x'\right)\right)}{\pi\left(m_x-m_x'\right)}+j\frac{\cos\left(\pi\left(m_x-m_x'\right)\right)-1}{\pi\left(m_x-m_x'\right)}\right)\left(\frac{\sin\left(\pi\left(m_y-m_y'\right)\right)}{\pi\left(m_y-m_y'\right)}+j\frac{\cos\left(\pi\left(m_y-m_y'\right)\right)-1}{\pi\left(m_y-m_y'\right)}\right) \tag{D.11}$$

For $m_x = m_x'$ (D.8) becomes

$$P_{\text{wg}}^{\text{i}} = \text{Re}\,\frac{1}{16\,(ab)}\frac{1}{\zeta_0}\left\{\sum_{m_x}\sum_{m_y}\bar{\bar{G}}^{ej}\left(k_x,k_y\right)\cdot\hat{p}_i\times\hat{k}_{m'}\times\left(\bar{\bar{G}}^{ej^*}\left(k_x,k_y\right)\cdot\hat{p}_i\right)\cdot\hat{z}\left|F_{\text{im}}^{\text{i}}\left(x',y'\right)\right|^2\right\} \tag{D.12}$$

Therefore, (D.12) becomes as follows

$$P_{\text{wg}}^{i} = \frac{1}{16ab}\frac{1}{\zeta_0}\,\text{Re}\left\{\sum_{m_x}\sum_{m_y}\left|F_{\text{im}}^{i}\left(x',y'\right)\right|^2\left|\bar{\bar{G}}^{ej}\left(k_{xm},k_{ym}\right)\cdot\hat{p}_i\right|^2\hat{k}_{zm}\right\} \tag{D.13}$$

While for $m_x \neq m_x'$ one obtains

$$P_{\text{wg}}^{i} = -\frac{1}{16ab}\frac{1}{\zeta_0}\,\text{Re}\Bigg\{\sum_{m_x\neq 0}\sum_{m_y\neq 0}\sum_{m_x'\neq 0}\sum_{m_y'\neq 0}\left|\bar{\bar{G}}^{ej}\left(k_{xm},k_{ym}\right)\cdot\hat{p}_i\right|^2\hat{k}_{zm}$$

$$\left|F_{\text{im}}^{i}\left(x',y'\right)\right|^2 e^{-jk_{zm}\left(z-\frac{h}{2}\right)}e^{jk_{zm'}\left(z-\frac{h}{2}\right)}\frac{\cos\left(\pi\left(m_x-m_x'\right)\right)}{\pi\left(m_x-m_x'\right)}\frac{\cos\left(\pi\left(m_y-m_y'\right)\right)}{\pi\left(m_y-m_y'\right)}\Bigg\} = 0 \tag{D.14}$$

thanks to the oddity of the sum with respect to $m_x - m_x'$ and $m_y - m_y'$. The function $F_{\text{im}}^{\text{i}}\left(x',y'\right)$ for the sources oriented along the three components can be written as

$$F_{\text{im}}^{x}\left(x',y'\right) = e^{jk_xx'}e^{jk_yy'} + e^{-jk_xx'}e^{jk_yy'} - e^{-jk_xx'}e^{-jk_yy'} - e^{jk_xx'}e^{-jk_yy'} \tag{D.15a}$$

$$F_{\text{im}}^{y}\left(x',y'\right) = e^{jk_xx'}e^{jk_yy'} - e^{-jk_xx'}e^{jk_yy'} - e^{-jk_xx'}e^{-jk_yy'} + e^{jk_xx'}e^{-jk_yy'} \tag{D.15b}$$

$$F_{\text{im}}^{z}\left(x',y'\right) = e^{jk_xx'}e^{jk_yy'} - e^{-jk_xx'}e^{jk_yy'} + e^{-jk_xx'}e^{-jk_yy'} - e^{jk_xx'}e^{-jk_yy'} \tag{D.15c}$$

with the minus signs accounting for the odd symmetry of the perfect electric conductor (PEC) plane for tangent sources. The sums of the complex exponentials can be rewritten as follows

$$F_{\text{im}}^{x}\left(x',y'\right) = 4j\cos\left(k_xx'\right)\sin\left(k_yy'\right) \tag{D.16a}$$

$$F_{\text{im}}^{y}\left(x',y'\right) = 4j\sin\left(k_xx'\right)\cos\left(k_yy'\right) \tag{D.16b}$$

$$F_{\text{im}}^{z}\left(x',y'\right) = -4\sin\left(k_xx'\right)\sin\left(k_yy'\right) \tag{D.16c}$$

Hence the power radiated by each component can be written as

$$P_{\text{wg}}^{x} = \frac{1}{ab}\frac{1}{\zeta_0}\sum_{m_x}\sum_{m_y}\left|\bar{\bar{G}}^{ej}\left(k_{xm},k_{ym}\right)\cdot\hat{x}\right|^2\hat{k}_{zm}\cos^2\left(k_{xm}x'\right)\sin^2\left(k_{ym}y'\right) \tag{D.17a}$$

$$P_{\text{wg}}^{y} = \frac{1}{ab}\frac{1}{\zeta_0}\sum_{m_x}\sum_{m_y}\left|\bar{\bar{G}}^{ej}\left(k_{xm},k_{ym}\right)\cdot\hat{y}\right|^2\hat{k}_{zm}\sin^2\left(k_{xm}x'\right)\cos^2\left(k_{ym}y'\right) \tag{D.17b}$$

$$P_{\text{wg}}^{z} = \frac{1}{ab}\frac{1}{\zeta_0}\sum_{m_x}\sum_{m_y}\left|\bar{\bar{G}}^{ej}\left(k_{xm},k_{ym}\right)\cdot\hat{z}\right|^2\hat{k}_{zm}\sin^2\left(k_{xm}x'\right)\sin^2\left(k_{ym}y'\right) \tag{D.17c}$$

E

Green's Function of a Slab inside a Waveguide

To evaluate the Green's function of a dielectric slab of thickness h and infinitely extended in x and y with the presence of backing reflector, as shown in Fig. E.1. One can resort to the equivalent transmission line model, and the Green's function of a horizontally polarized source located in the slab can be written as

$$\bar{\bar{G}}^{ej}\left(k_x,k_y\right)=\begin{bmatrix} -\frac{v^{\mathrm{TM}}k_x^2+v^{\mathrm{TE}}k_y^2}{k_\rho^2} & \frac{\left(v^{\mathrm{TE}}-v^{\mathrm{TM}}\right)k_xk_y}{k_\rho^2} \\ \frac{\left(v^{\mathrm{TE}}-v^{\mathrm{TM}}\right)k_xk_y}{k_\rho^2} & -\frac{v^{\mathrm{TE}}k_x^2+v^{\mathrm{TM}}k_y^2}{k_\rho^2} \\ \zeta\frac{k_x}{k}i^{\mathrm{TM}} & \zeta\frac{k_y}{k}i^{\mathrm{TM}} \end{bmatrix} \tag{E.1}$$

where v^{TM}, v^{TE}, i^{TM}, and i^{TE} are the Transverse Magnetic (TM) and Transverse Electric (TE) solutions of the current the voltage at the observation point as shown in Fig. E.2, $k_\rho=\sqrt{k_x^2+k_y^2}$ is the tangent component of the wave number and ζ is the characteristic impedance.

To characterize the Green's function (E.1), one has to find the voltage and current along the equivalent transmission line model. Due to the presence of the TE and the TM modes, an equivalent transmission line for each mode has to be formulated and solved. As shown in Fig E.3, the upper and lower part of the transmission line model can be represented by an equivalent impedance Z_{up} and Z_{down}, solution of which can be written

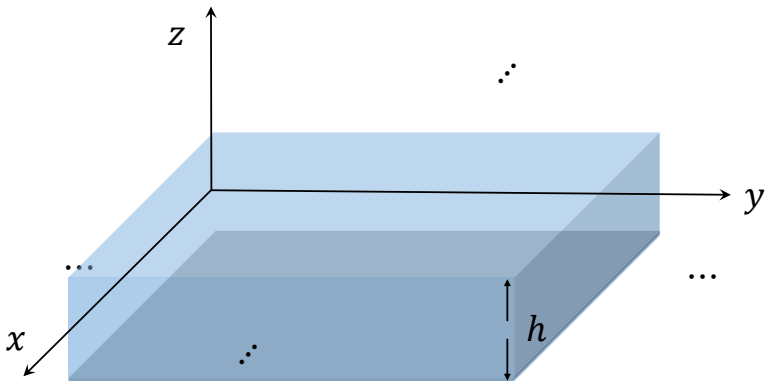

Figure E.1: A infinite slab of thickness h on top of a reflector

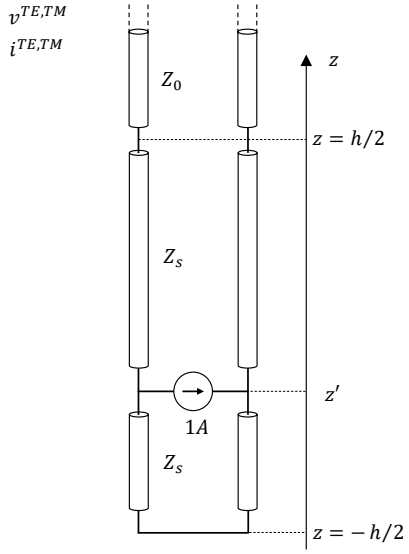

Figure E.2: Equivalent transmission line model of an horizontally polarized elementary source located at $z = z'$, in a dielectric slab of thickness h.

as

$$Z_{\text{up}}^{\text{TE,TM}} = Z_s^{\text{TE,TM}} \frac{Z_0^{\text{TE,TM}} + jZ_s^{\text{TE,TM}} \tan\left(k_{zs}\left|\frac{h}{2} - z'\right|\right)}{Z_s^{\text{TE,TM}} + jZ_0^{\text{TE,TM}} \tan\left(k_{zs}\left|\frac{h}{2} - z'\right|\right)} \tag{E.2a}$$

$$Z_{\text{down}}^{\text{TE,TM}} = jZ_s^{\text{TE,TM}} \tan\left(k_{zs}\left|\frac{h}{2} - z'\right|\right) \tag{E.2b}$$

where

$$Z_0^{\text{TM}} = \frac{\zeta_0 k_{z0}}{k_0} \tag{E.3a}$$

$$Z_s^{\text{TM}} = \frac{\zeta_0 k_{zs}}{k_s} \tag{E.3b}$$

$$Z_0^{\text{TE}} = \frac{\zeta_0 k_0}{k_{z0}} \tag{E.3c}$$

$$Z_s^{\text{TE}} = \frac{\zeta_0 k_s}{k_{zs}} \tag{E.3d}$$

$$k_{z0} = \sqrt{k_0^2 - k_{x0}^2 - k_{y0}^2} \tag{E.3e}$$

$$k_{zs} = \sqrt{k_s^2 - k_{xs}^2 - k_{ys}^2}. \tag{E.3f}$$

where k_0 and k_s is the wavenumber in free space and in the dielectric respectively.

After having characterized the input impedances of the upper and of the lower section, the voltage and current distribution along the equivalent transmission line have to be determined. The two transmission lines problems associated with the TE and TM modes have to be solved separately, but with an analogous procedure. Since the same operations are carried out on the TE and TM problem, the the TE and TM superscripts are omitted for simplicity. The voltage and the current on the transmission line can be expressed as (E.4)

$$V(z) = V^+ e^{-jk_{zs}z} + V^- e^{jk_{zs}z} \tag{E.4a}$$

$$I(z) = \frac{V^+}{Z_s} e^{-jk_{zs}z} - \frac{V^-}{Z_s} e^{jk_{zs}z} \tag{E.4b}$$

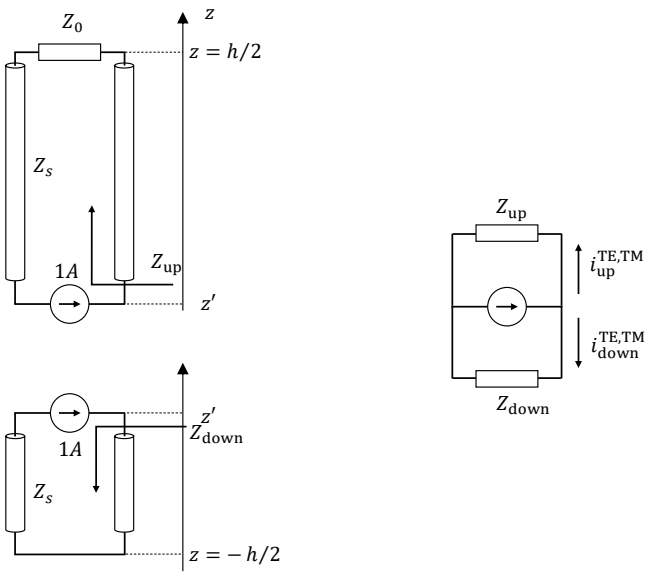

Figure E.3: Equivalent impedance of the upper part and the lower part of the circuit

where V^+ and V^- are the amplitudes of the voltage waves propagating along the positive, and negative z-direction, respectively. The voltage and the current at $z = h/2$, i.e., on the top of the slab, can be written as

$$V\left(\frac{h}{2}\right) = V^+ e^{-jk_{zs}\frac{h}{2}} + V^- e^{jk_{zs}\frac{h}{2}} \tag{E.5a}$$

$$I\left(\frac{h}{2}\right) = \frac{V^+}{Z_s} e^{-jk_{zs}\frac{h}{2}} - \frac{V^-}{Z_s} e^{jk_{zs}\frac{h}{2}}. \tag{E.5b}$$

Since at $z = h/2$,since the equivalent impedance at that section is Z_{tot}, and the transmission line is excited with 1 A at $z = z'$, one can write as follows

$$V\left(\frac{h}{2}\right) = Z_0 I\left(\frac{h}{2}\right). \tag{E.6}$$

Combining (E.5a), (E.5b) and (E.6), one obtains the following realationship

$$V^+ = V^- \frac{Z_s + Z_0}{Z_0 - Z_s} e^{jk_{zs}h}. \tag{E.7}$$

Similarly, at $z = z'$, the voltage and the current follow the Ohm's law

$$V\left(z'\right) = Z_{\text{tot}} \cdot I\left(z'\right) = Z_{\text{tot}} \cdot 1A \tag{E.8}$$

where

$$Z_{\text{tot}} = Z_{\text{up}} || Z_{\text{down}} = \frac{Z_{\text{up}} Z_{\text{down}}}{Z_{\text{up}} + Z_{\text{down}}}. \tag{E.9}$$

By combining (E.9) and (E.4a) with $z = z'$, one can express V^- as follows

$$V^- = \frac{Z_{\text{tot}}}{\frac{Z_0+Z_s}{Z_0-Z_s} e^{jk_{zs}h} e^{-jk_{zs}z'} + e^{jk_{zs}z'}} = \frac{\Gamma Z_{\text{tot}}}{e^{jk_{zs}h} e^{-jk_{zs}z'} + \Gamma e^{jk_{zs}z'}} \tag{E.10}$$

where Γ is the reflection coefficient between Z_s and Z_0

$$\Gamma = \frac{Z_0 - Z_s}{Z_0 + Z_s}. \tag{E.11}$$

Then by combining (E.7) and (E.10), V^+ can be written as

$$V^+ = \frac{Z_{\text{tot}}}{e^{jk_{zs}h}e^{-jk_{zs}z'} + \Gamma e^{jk_{zs}z'}} e^{jk_{zs}h}. \tag{E.12}$$

Therefore, the voltage and current at $z = h/2$ in (E.5a) and (E.5b) can be derived by using (E.12) and (E.10)

$$V\left(\frac{h}{2}\right) = \frac{(1+\Gamma)\, Z_{\text{tot}}}{e^{jk_{zs}\left(\frac{h}{2}-z'\right)} + \Gamma e^{-jk_{zs}\left(\frac{h}{2}-z'\right)}} = v \tag{E.13a}$$

$$I\left(\frac{h}{2}\right) = \frac{1}{Z_0} \frac{(1+\Gamma)\, Z_{\text{tot}}}{e^{jk_{zs}\left(\frac{h}{2}-z'\right)} + \Gamma e^{-jk_{zs}\left(\frac{h}{2}-z'\right)}} = i \tag{E.13b}$$

F

Graphical User Interface

F.1. Start Page

Fig F.1 shows the overview of the GUI's start page, where the measure of unit of the project, the interested frequency range are defined. By clicking the "Create" or "Load" button, the user can create a new file or load an existing file respectively.

In the drop-down lists at ① and ②, the user can define their preferred measure unit for the frequency and the length, respectively.

The frequency range under investigation is defined in ③ and ④ as the minimum and the maximum frequency. The field of ③ and ④ is numeric and uses the units defined in ①.

By clicking the check box at ⑤, the user chooses to define the dimension of the structures in terms of the wavelength. If the ⑤ is checked, the numeric field at ⑥ can be filled, where the reference frequency of the wavelength is defined with the units defined in ①. For example, if the user defines the reference frequency as 150 GHz, then the dimensions used in later stage will be "2 mm" and overwrite the units ②. The checkbox ⑤ by default, and can be optionally chosen.

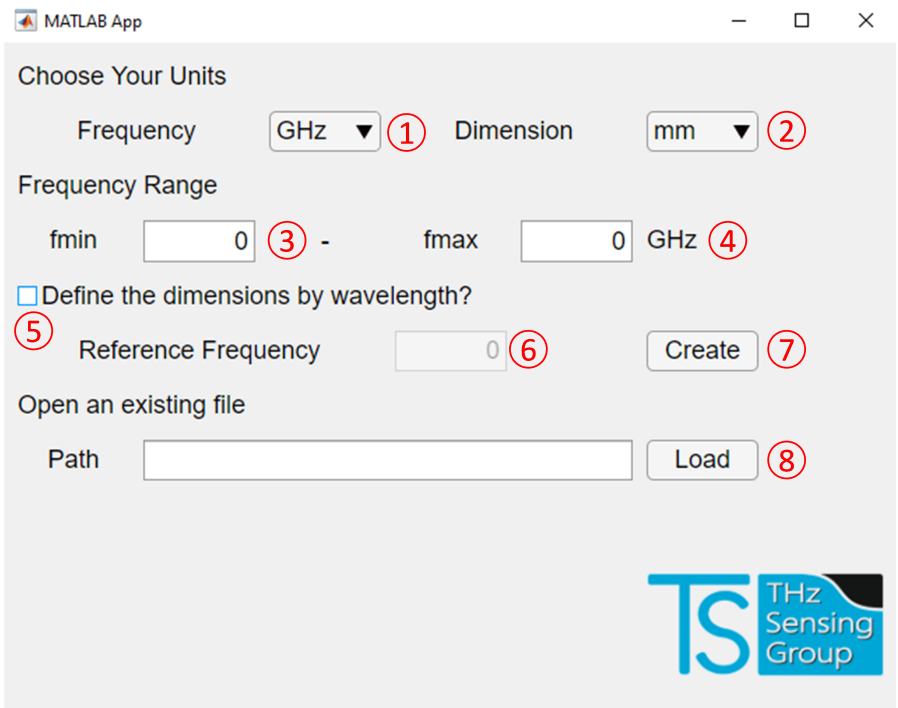

Figure F.1: Overview of the start page of the GUI

By clicking the "Create" button at ⑦ the user creates a new project and a window appears to select the file destination as indicated in Fig. F.2. The user can change the project file name, and the default project name is "NewProject".

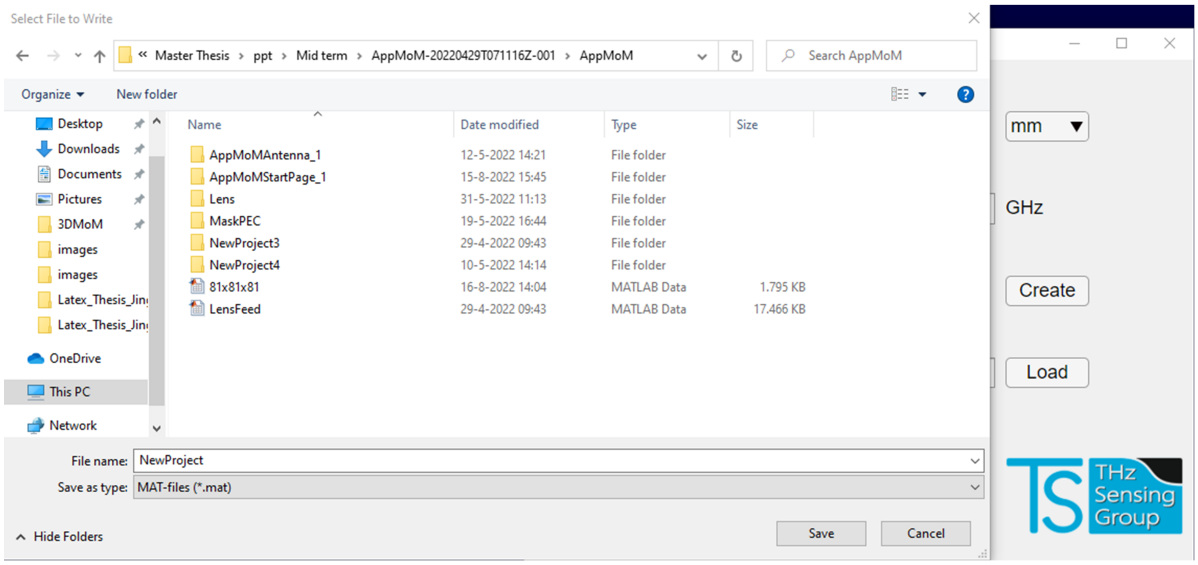

Figure F.2: Window to select the created file's destination

After the "Save" button in Fig. F.2 is clicked, a folder with the chosen file name is created in the destination as shown in the left side of Fig. F.3. The folder have a structure indicated by the right side of Fig. F.3, where

- the ".mat" file in the red box is the main file that stores all the information of the project, and it is named "ProjectName + Main".
- The "Current" folder is used to store the solution of the equivalent currents, which can be imported into the project gained in the main page (Fig. F.5).
- The "Excitation" folder stores the excitation information of the project.
- The "Export" folder stores the results of the simulation on the user's demand.
- The "Geometry" folder stores the shapes of the project.
- The folder "Grid" stores by default the pre-computed reaction integrals.

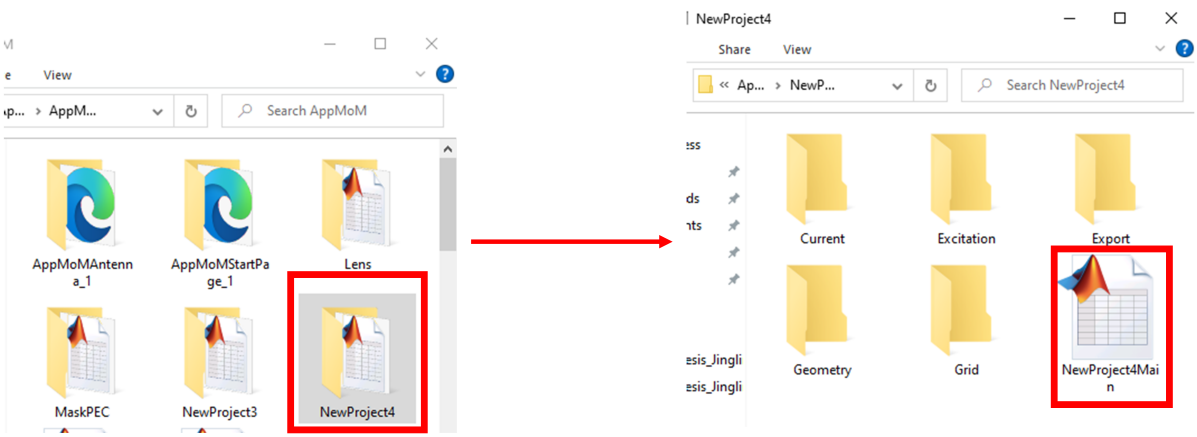

Figure F.3: Location and structure of the created folder

The the user may click the "Load" button ⑧ in Fig. F.1 to open an already existing project. A pre-existing project can be loaded by selecting the main file, as shown in Fig. F.3.

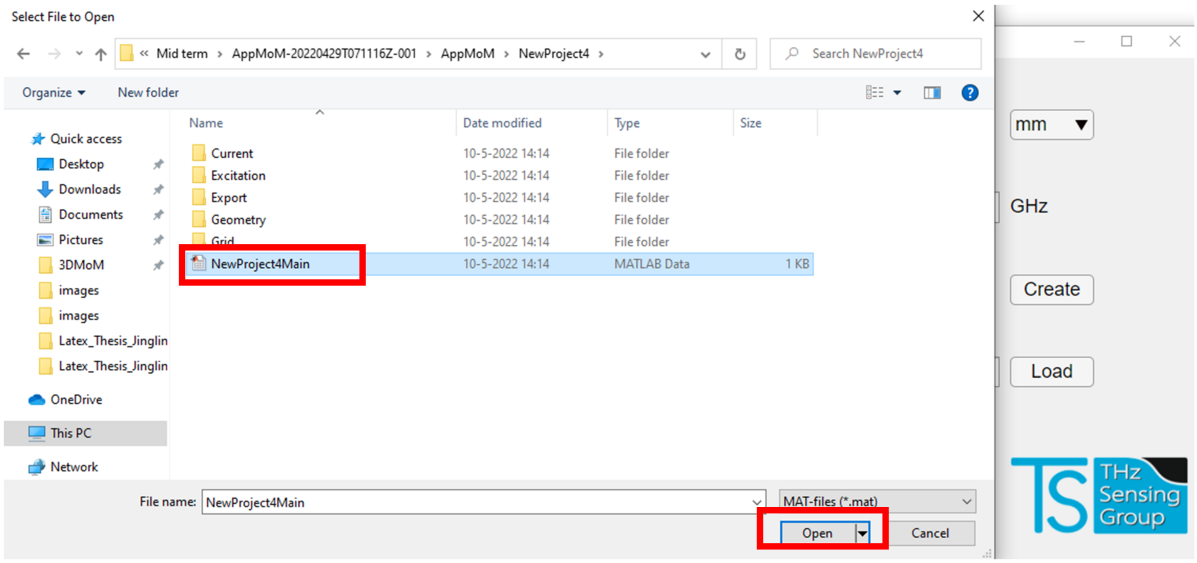

Figure F.4: Window to select the loaded file

After creating a new project or loading a previous project, the tool is directed to the Main working page as shown in Fig. F.5. The **blue**area is pertinent to the structured grid used in the project. The **green** region is used to defineand combine all the different shapes that constitute the geometry under analysis. The **red** part is used for the plane wave excitation. The **yellow** part is used for the discrete port excitation. The **purple** box indicates the measure units used in the project. The **black** box displays the messages from the tool. The geometry under analysis is shown on the right side of the page.

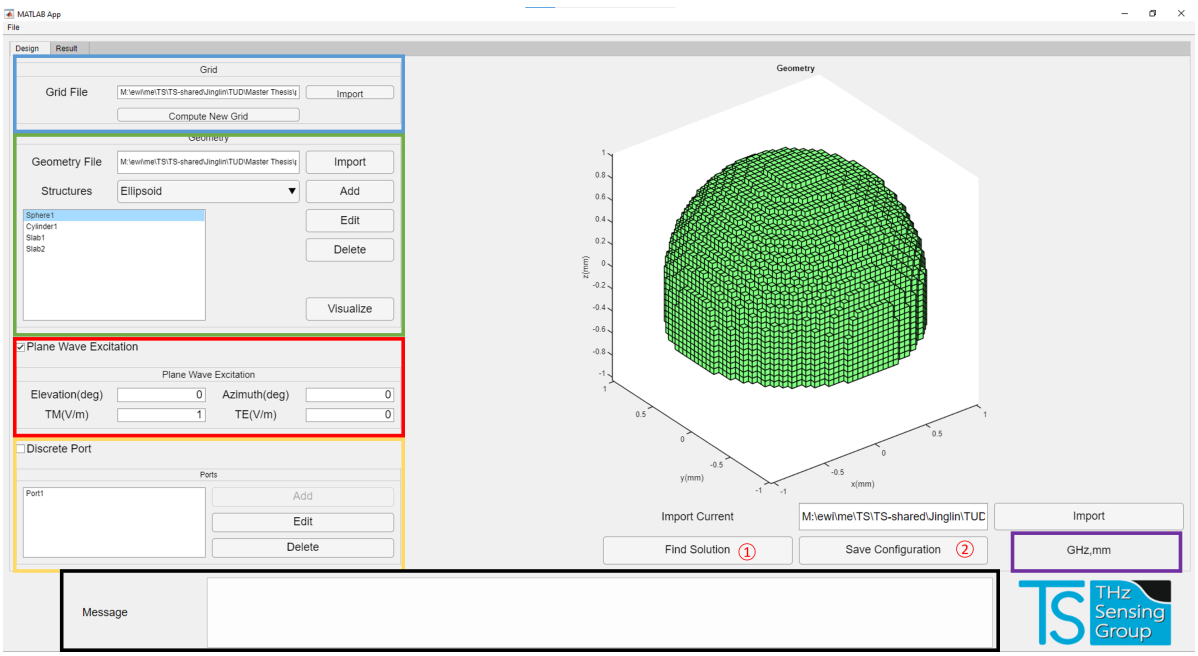

Figure F.5: Overview of the design page of the GUI

F.2. Pre-Computation

In the "Grid" panel, the user can either load an existing grid file by clicking the "Import" button or compute anew one by clicking the "Compute New Grid" button. Once the "Import" button is clicked, the user can select a "*projectname*Grid.mat" grid file, which is usually placed in the "Grid" folder as shown in Fig. F.3.

The destination of the grid file used in this project is displayed in the "Grid File" text field. To compute a new grid, click "Compute New Grid", then the tool directs to a new sub-window. The frequency range of the new grid is defined in ① and ②. The number of the frequency points equispaced between the minimum and maximum frequency is defined in ③. The dimension of the discretized box, and the length of the basis function are defined in ④, ⑤, ⑥, and ⑦. The properties of the background material are then selected, i.e., the permittivity with ⑧ and, if lossy, the conductivity ⑨. The path where the grid is stored, is defined at ⑩. By clicking ⑪, the grid starts to be computed.

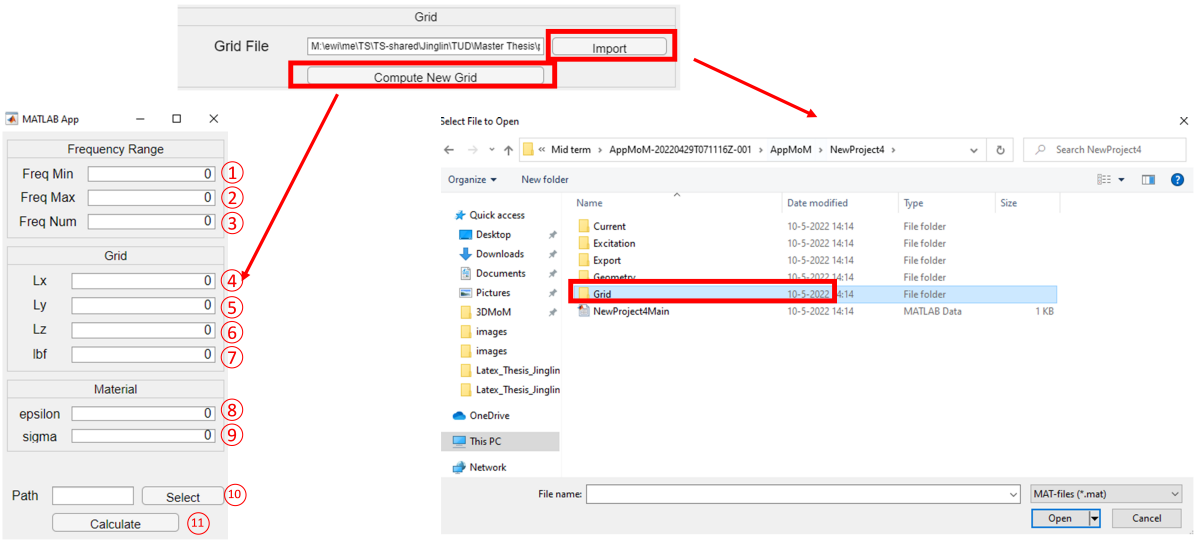

Figure F.6: Overview of the "Geometry" panel for grid definition

The grid file contains a struct named "GridInfo", which has several fields. "Dim" is a vector containing the size of the grid as $[L_x, L_y, L_z]$ expressed in meters. The variable "lbf" denotes the length of the basis function expressed in meters. The vector "Freq" records the frequency points expressed in Hertz. "Imp" is a cell array that contains the radiation matrix $\mathbf{Z}_{xx}^{rad}$ and $\mathbf{Z}_{xy}^{rad}$ having a dimension of $[N_x \times N_y \times N_z \times N_f]$. "Centers" contains the position vectors of the voxels. "Number" denotes the number of basis function along x, y, and z by $[N_x, N_y, N_z]$. "Mat" stands for the material of the background using $[\varepsilon_r, \sigma]$. Note that all the variables on the interface is in user defined unit while all the files and variables that the tool work with has a unit in SI.

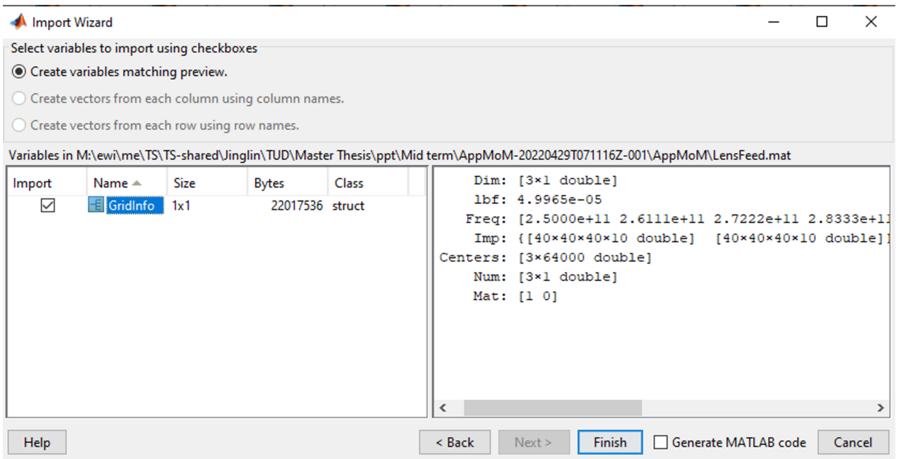

Figure F.7: Data structure of the grid file

F.3. Design

In the main page the user is able to design and visualize their desired geometries and excitation terms.

F.3.1. Geometry Design

In the "Geometry" panel shown in Fig. F.8, the user can import, add, edit, delete and plot the geometries by using the buttons from ②-⑥.

Adding Shapes The user can add the four basic geometries (i.e., ellipsoid, sphere, slab, cylinder) by first selecting the shape in the shape drop-down list ① and pressing the "Add" button at ③. After the button is clicked, the sub window appears for parametrization of the shapes as shown in Fig. F.9. After the parametrization of the shape the user can click the "Confirm" button and the created is added in the list box on the left.

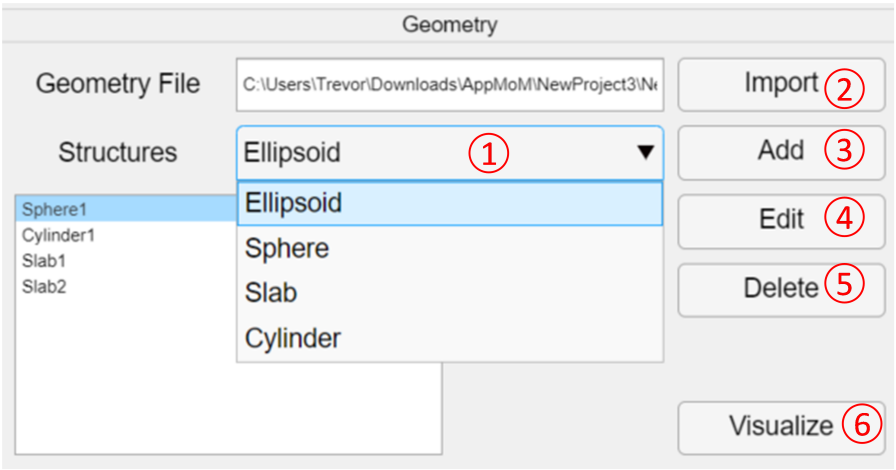

Figure F.8: Overview of the "Geometry" panel for shape design

After that a shape is added, the user may rename it in the "Name" field ①, as shown in Fig. F.9. The parameters describing the shapes are set in "Dimension" ②, and the material is specified in ③. The shapes can be displaced along x, y, and z using the panel "Transform" ④ . By clicking the "Rotate" button ⑤, the user is redirected to a dedicated page, as shown in Fig. F.10. Then by clicking the "Confirm" button ⑥, the user can create a shape in the list box.

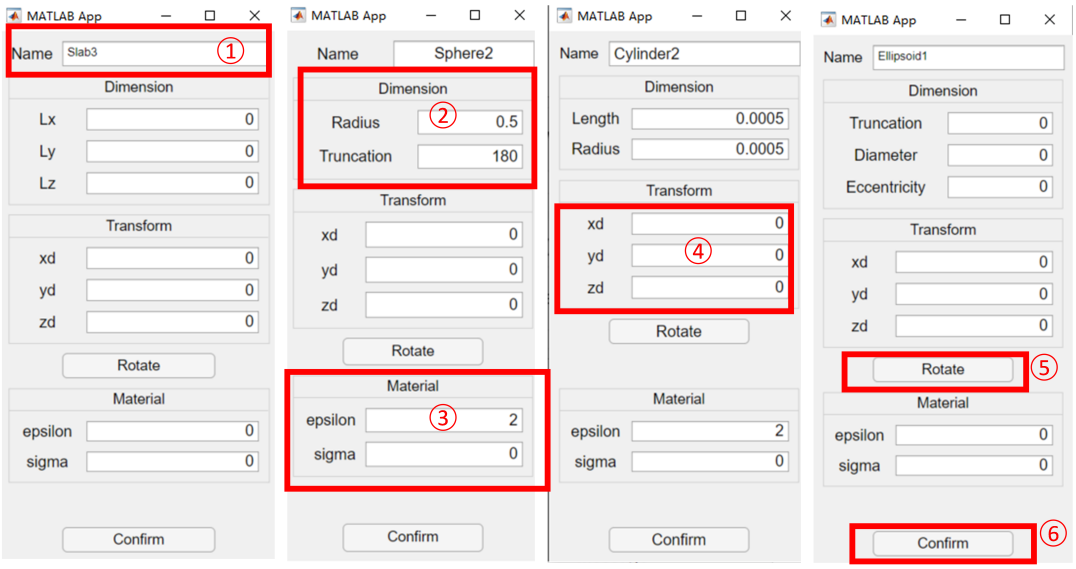

Figure F.9: Parametrization pages of the shapes in GUI

User may rename their shapes in the "Name" field at ①, as shown in Fig. F.9. At ② and ③, the parameters and materials of the shapes are defined in the "Dimension" and "Material" panel respectively. The shapes can be displaced along x, y, and z using the panel Transform at ④. Then by clicking the "Rotate" button at ⑤,

the user is directed to the rotation page of the shapes, as shown in Fig. F.10. Then by clicking the "Confirm" button at ⑥, the user can create a shape in the list box.

In the rotation page, by clicking the "Add" button at ①, the user can create a rotation. At the axis drop-down list at ②, the axis of the rotation can be chosen in terms of x, y, and z. Angles of the rotation are defined at the "Angle" field at ③ in degrees. The direction of rotation is defined always as the counter-clockwise direction when the centre axis is facing you, as shown in Fig. 4.3. The "Step" field denotes the ordering of the rotation. A step of rotation can be deleted when the user selects the unwanted row and presses the "Delete" button at ④. Finally the rotation is applied to the shapes when the user press button "Apply" at ⑤.

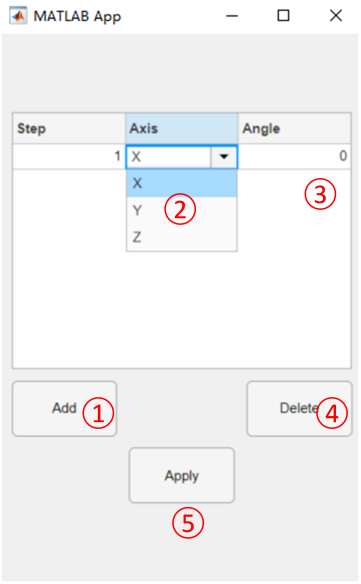

Figure F.10: Rotation page of the shapes in GUI

Editing and Deleting Shapes To edit or delete a shape, the user needs to select the shape in the list box in Fig. F.8 and to click the "Edit" or the "Delete" button. After the "Edit" button is pushed, the user can return to the parametrization page as shown in Fig. F.9. All information is automatically refilled in the field and the changing step is the same as the adding part.

Import Geometry The user can import a geometry file using ② in Fig. F.8. The geometry file contains a struct named "GeoInfo", which has several fields: "Shapes" is a string array containing the type of shapes used in the geometry, the string array "NameTag" denotes the name given to each shape, "ShapeParameter" is a $N \times 8$ matrix that contains the paramters that define each shape, "Rotaiton" is a struct array that records the rotation information of each shape, and the indexes of the shapes are stored in the cell array "Idx".

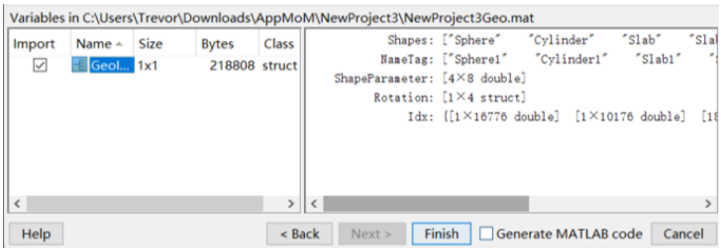

Figure F.11: Data structure of the geometry file

F.3.2. Excitation Design

Plane Wave Excitation By checking the plane wave excitation box at ① in Fig. F.12, the user excites the grid with a plane wave. The plane wave is defined by its direction of incidence, given by the azimuth and the

elevation angles (ϕ, θ) at ② and ③, and its TM and TE polarization at ④ and ⑤ respectively.

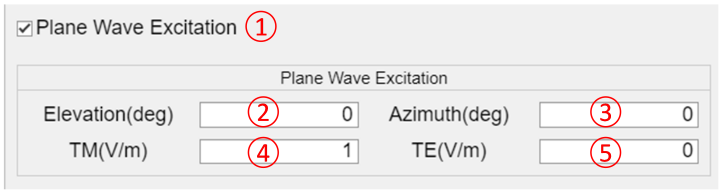

Figure F.12: Plane wave excitation page

Discrete Port Excitation By checking the discrete port box, as shown in Fig. F.13, the user excites the grid with discrete ports by adding, editing or deleting a port at ①-③. The geometry of the port is defined a cuboid, and by default it has a electric field oriented along the x-axis by default without any rotation. The source impedance of the port and the voltage on the gap are defined in ⑤ and ⑥. Note that only one type of excitation is allowed in the tool, so by checking one excitation method, the other one is disabled automatically. By

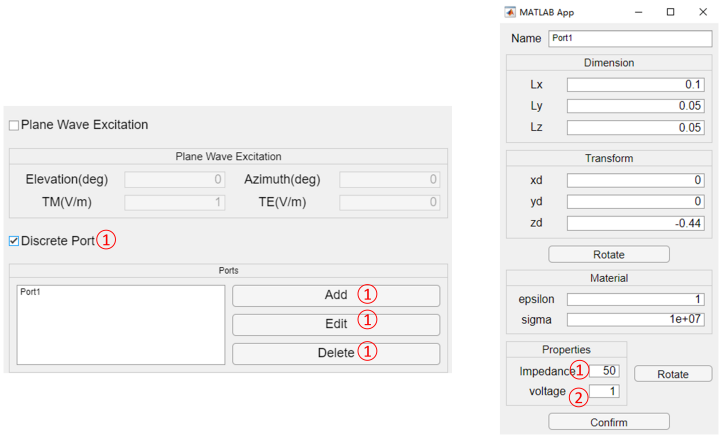

Figure F.13: Discrete port excitation page

clicking the "Find Solution" button ① in Fig. F.5, the linear system solver is started.

F.4. Result

The results from the too contains the electric field inside the body, the far field properties, and the circuit parameters, which can be accesses by the tab button in the red box as shown in Fig. F.14.

F.4.1. Near Field Distribution

As shown in Fig. F.14, in the electric field window the user can click the button "Plot Near Field" ⑧ , to plot the absolute value the electric field on the plane chosen in the "Plane Cut" panel ①. The user can select the position of the cut at ③, the component of the field at ② and the frequency at ⑪. The limits of the x-axis, the y-axis and the color bar can be ajusted using the fields at ④-⑥. The phase can be adjusted at ⑦ and by checking the "Animation" box at ⑧ the user plots the animated field with a varying phase.

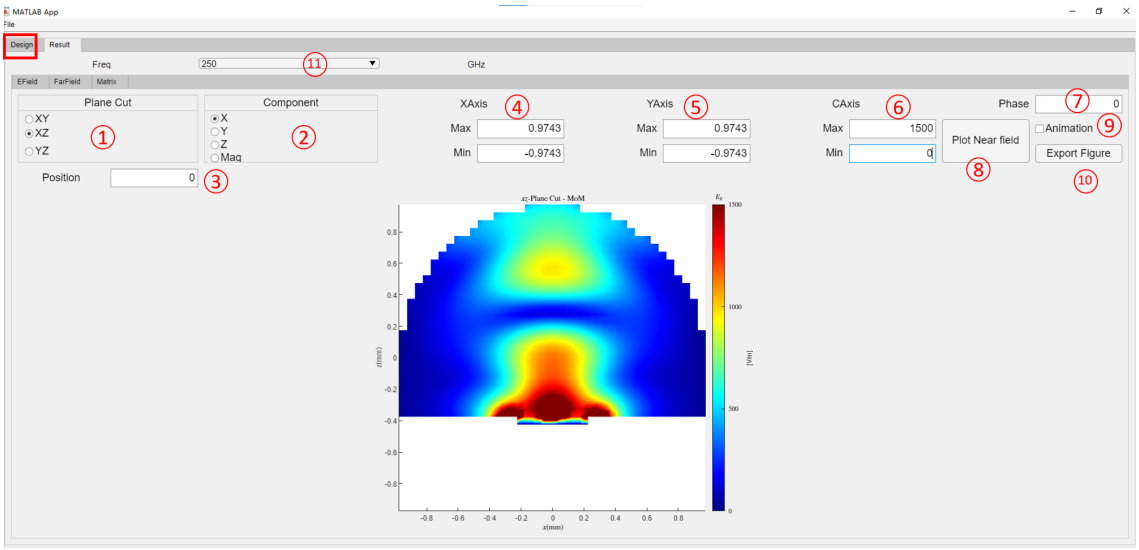

Figure F.14: The result page of the electric field inside the body

F.4.2. Far Field

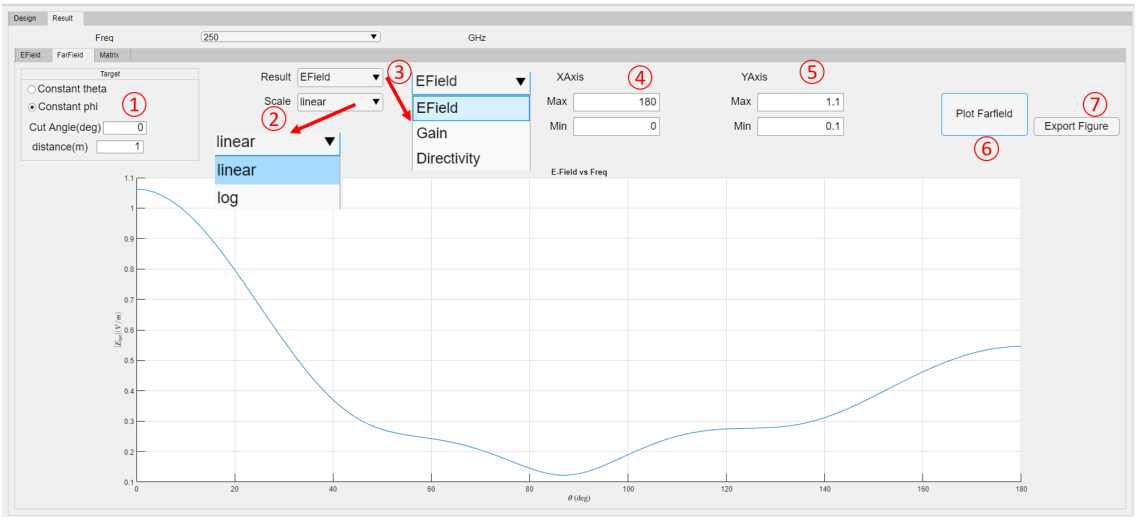

Figure F.15: The result page of the farfield properties

In the far field page, as shown in Fig. F.15, the user can plot the far field properties and export the figure using ⑥ and ⑦, respectively. At the "Target" panel denoted by ①, the far field pattern is chosen to be plotted in a constant θ or constant ϕ plane, specified by an angle defined in degrees and at the certain distance

defined in meters. At the drop-down list at ③ the user can choose to plot the electric field, the directivity or the gain. The drop-down list at ② is chosen to plot the quantities in either linear scale or logarithm scale. At ④ and ⑤ the limits of the axis can be adjusted. The sampling of the x-axis is 100 points in the tool.

F.4.3. Circuit Parameter

By clicking the "Matrix" button, the user enters the result page of circuit parameters, as shown in Fig. F.16. The Z, Y, and S parameters of the antenna can be selected, plotted and exported using ②, ⑥, and ⑦ respectively. At the drop-down list at ①, the scale can be chosen as linear or logarithm. By selecting in the component drop-down list at ③, the user can plot different component of the parameters in terms of the real and imaginary part, magnitude and phase. In the field at ④ and ⑤, the limits of the axes can be adjusted.

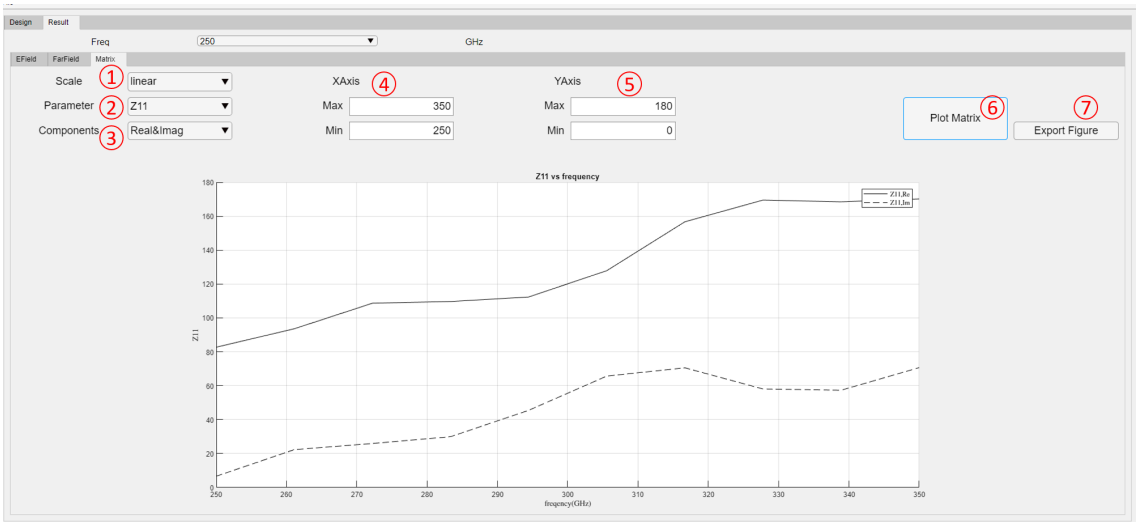

Figure F.16: The result page of the circuit parameters

F.5. Save Project and Export Result

The user can store the project by clicking the "Save Configuration" button at ⑤ in Fig. F.5 or by using the "Save" option in the menu bar as shown in Fig. F.17. The configuration of the project then is saved to the main file. By clicikng the "Save as" option and select a destination, the user created another file folder to save the configuration of the current project. The grid, geometry, the equivalent current, the excitation, and the post-processed result can be exported using the "Export" option in the menu.

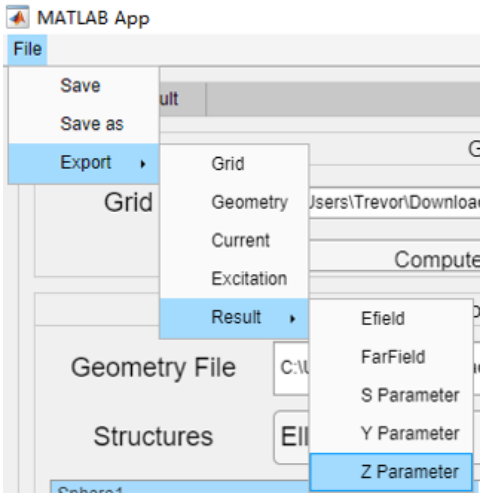

Figure F.17: Menu to save the project

F.6. Potential Malfunctions and Their Solutions

ProjectName or ProjectName not found The update of the project destination in the tool is not automatic, therefore, it is highly recommended to stay in the same folder for a fixed project. In case there is a need to change the repository of the project or an error accurs, the user should try to load the main file in MatLab workspace and change the project name and path manually.

Circuit parameters not loaded When loading the result from an existing project, if the circuit parameter is not loaded, try to plot the geometry once more by pressing the "Visualization" button at ⑥ in Fig. F.8. The tool takes the port information from the desinged geometry.

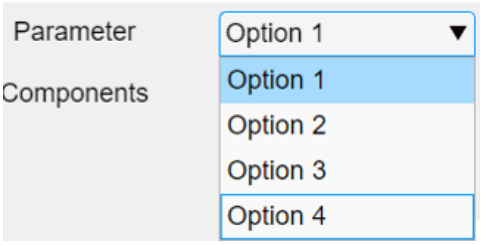

Figure F.18: Circuit parameters not loaded in a project

The GUI will be available on the THz Sensing Group's website [33]. Currently, the GUI is still under testing and bug reports are appreciated by us to continue improve the GUI. Please send your questions and findings to us by [33].

Bibliography

[1] H. Zhang, S. Bosma, A. Neto, and N. Llombart, "A dual-polarized 27 dbi scanning lens phased array antenna for 5g point-to-point communications," *IEEE Transactions on Antennas and Propagation*, vol. 69, no. 9, pp. 5640–5652, 2021.

[2] N. van Rooijen, M. Alonso-delPino, M. Spirito, and N. Llombart, "Core-shell leaky-wave lens antenna for 150ghz fly's eye communication systems," in *presented at the 16th European Conference on Antennas and Propagation (EuCAP)*, Mar. 27-Apr. 1 2022, pp. 1–5.

[3] L. Ferrari, O. Yurduseven, N. Llombart, S. J. C. Yates, J. Bueno, V. Murugesan, D. J. Thoen, A. Endo, A. M. Baryshev, and J. J. A. Baselmans, "Antenna coupled mkid performance verification at 850 GHz for large format astrophysics arrays," *IEEE Transactions on Terahertz Science and Technology*, vol. 8, no. 1, pp. 127–139, 2018.

[4] E. Gandini, J. Svedin, T. Bryllert, and N. Llombart, "Optomechanical system design for dual-mode standoff submillimeter wavelength imagers," *IEEE Transactions on Terahertz Science and Technology*, vol. 7, no. 4, pp. 393–403, 2017.

[5] D. Filipovic, S. Gearhart, and G. Rebeiz, "Double-slot antennas on extended hemispherical and elliptical silicon dielectric lenses," *IEEE Transactions on Microwave Theory and Techniques*, vol. 41, no. 10, pp. 1738–1749, 1993.

[6] E. Lima, J. R. Costa, M. G. Silveirinha, and C. A. Fernandes, "ILASH - software tool for the design of integrated lens antennas," in *2008 IEEE Antennas and Propagation Society International Symposium*, 2008, pp. 1–4.

[7] J. Budhu and Y. Rahmat-Samii, "A novel and systematic approach to inhomogeneous dielectric lens design based on curved ray geometrical optics and particle swarm optimization," *IEEE Transactions on Antennas and Propagation*, vol. 67, no. 6, pp. 3657–3669, 2019.

[8] H. Zhang, S. O. Dabironezare, G. Carluccio, A. Neto, and N. Llombart, "A fourier optics tool to derive the plane wave spectrum of quasi-optical systems [EM programmer's notebook]," *IEEE Antennas and Propagation Magazine*, vol. 63, no. 1, pp. 103–116, 2021.

[9] A. Nair, S. O. Dabironezare, A. Neto, and N. Llombart, "On the evaluation of mutual coupling in integrated lens arrays," in *16th European Conference on Antennas and Propagation (EuCAP 2022)*, Madrid, Spain, Mar. 2022.

[10] V. I. T. Sergei M. Rytov, Yurii A. Kravtsov, *Principles of Statistical Radiophysics 1*. Heidelberg, Germany: Springer Berlin, Heidelberg, 1976.

[11] D. Polder and M. Van Hove, "Theory of radiative heat transfer between closely spaced bodies," *Phys. Rev. B*, vol. 4, pp. 3303–3314, Nov 1971.

[12] J.-J. Greffet, P. Bouchon, G. Brucoli, and F. Marquier, "Light emission by nonequilibrium bodies: Local Kirchhoff law," *Phys. Rev. X*, vol. 8, p. 021008, Apr 2018.

[13] P. Drude, "Zur elektronentheorie der metalle," *Annalen der Physik*, vol. 306, no. 3, pp. 566–613, 1900.

[14] P. P. Silvester and R. L. Ferrari, *Finite Elements for Electrical Engineers*, 3rd ed. Cambridge University Press, 1996.

[15] J. Jin, *The Finite Element Method in Electromagnetics*, 3rd ed. Wiley-IEEE Press, 2014.

[16] J. Volakis and K. Sertel, *Integral Equation Methods for Electromagnetics*, ser. Electromagnetic Waves. Institution of Engineering and Technology, 2012.

[17] R. F. Harrington, *Field computation by moment methods*. Piscataway, New Jersey: IEEE Press, 2015.

[18] J. Markkanen, P. Yla-Oijala, and A. Sihvola, "Discretization of volume integral equation formulations for extremely anisotropic materials," *IEEE Transactions on Antennas and Propagation*, vol. 60, no. 11, pp. 5195–5202, 2012.

[19] Rotation matrix. [Online]. Available: https://nl.mathworks.com/help/phased/ref/rotx.html

[20] G. Mie, "Beiträge zur optik trüber medien, speziell kolloidaler metallösungen," *Annalen der Physik*, vol. 330, no. 3, pp. 377–445, 1908.

[21] J. Schäfer. (2016) Matscat. [Online]. Available: https://nl.mathworks.com/matlabcentral/fileexchange/36831-matscat?tab=reviews%2F2100233

[22] [Online]. Available: https://www.3ds.com/products-services/simulia/products/cst-studio-suite/

[23] G. R. Kirchhoff, "On the relation between the radiating and absorbing powers of different bodies for light and heat," *Philosophical Magazine Series 1*, vol. 20, pp. 1–21, 1860.

[24] M. Planck, *The Theory of Heat Radiation*. Blakiston, 1914.

[25] J. B. Johnson, "Thermal Agitation of Electricity in Conductors," *Physical Review*, vol. 32, no. 1, pp. 97–109, Jul. 1928.

[26] H. Nyquist, "Thermal Agitation of Electric Charge in Conductors," *Physical Review*, vol. 32, no. 1, pp. 110–113, Jul. 1928.

[27] A. G. Polimeridis, M. T. H. Reid, W. Jin, S. G. Johnson, J. K. White, and A. W. Rodriguez, "Fluctuating volume-current formulation of electromagnetic fluctuations in inhomogeneous media: Incandescence and luminescence in arbitrary geometries," *Phys. Rev. B*, vol. 92, p. 134202, Oct 2015.

[28] R. M. van Schelven, A. Fiorellini Bernardis, P. Sberna, and A. Neto, "Drude dispersion in the transmission line modeling of bulk absorbers at sub-mm wave frequencies: A tool for absorber optimization," *IEEE Antennas and Propagation Magazine*, vol. 64, no. 1, pp. 50–60, 2022.

[29] H. Chen, *Theory of Electromagnetic Waves*, ser. McGraw-Hill series in electrical engineering: Electromagnetics. CBLS Publishers, 1992.

[30] A. Yaghjian, "Electric dyadic green's functions in the source region," *Proceedings of the IEEE*, vol. 68, no. 2, pp. 248–263, 1980.

[31] J. G. V. Bladel, "Green's dyadics," in *Singular Electromagnetic Fields and Sources*. IEEE, 1991, pp. 59–115.

[32] N. V. Budko, "Lectures on computational electromagnetics-the volume integral equation method." [Online]. Available: https://docs.google.com/viewer?a=v&pid=sites&srcid=ZGVmYXVsdGRvbWFpbnxwaHlzaWN1c25hdHVyYWxpc3xneDo1ZWFmYjE5MmU2ZWQxYmJm

[33] [Online]. Available: https://terahertz.tudelft.nl/